Temperature and Density Measurements of Plasmas

Paweł Marek Kozłowski

Wolfson College

University of Oxford

A thesis submitted for the degree of

Doctor of Philosophy

Trinity term, 2016

Temperature and Density Measurements of Plasmas

Pawel Marek Kozlowski
Wolfson College, University of Oxford

Thesis Submitted for the Degree of Doctor of Philosophy
Trinity term, 2016

Abstract

Diagnosing the temperatures and densities of plasmas is critical to the understanding of a wide variety of phenomena. Everything from equations of state for warm dense matter (WDM) found in Jovian planets and inertial confinement fusion (ICF) to turbulent and dissipative processes in laser-produced plasmas, rely on accurate and precise measurements of temperature and density. This work presents improvements on two distinct techniques for measuring temperatures and densities in plasmas: x-ray Thomson scattering (XRTS), and Langmuir probes (LPs).

At the OMEGA laser facility, experiments on warm dense matter were performed by firing lasers at an ablator foil and driving a planar shock into cryogenically cooled liquid deuterium. XRTS in the collective scattering regime was implemented to probe the matter, measuring densities of $n_e \sim 4.3 \times 10^{23}\,\mathrm{cm}^{-3}$, temperatures of $T_e \sim 12\,\mathrm{eV}$ and ionizations of $Z \sim 1.0$. Through an extension to XRTS theory for inhomogeneous systems, it was possible to extract an additional parameter, the length scale of the shock, whose value of $\Lambda \sim 1.33\,\mathrm{nm}$ was consistent with the predicted mean free path, and therefore the thickness of the shock.

A unique triple Langmuir probe prototype was designed and tested at the Gregori group's lab at the University of Oxford. This probe was designed for a high temporal resolution of $\sim 200\,\mathrm{MHz}$ for probing laser-produced shocks. The probes were used to measure the shock formed from ablating carbon rods in an argon gas fill. The probe yielded plasma parameters of $n_e \sim 1.0 \times 10^{17}\,\mathrm{cm}^{-3}$, and $T_e \sim 1.5\,\mathrm{eV}$, consistent with measurements from interferometry and emission spectroscopy.

Aye, I suppose I could stay up that late.

—James Clerk Maxwell, on being told on his arrival at Cambridge University that there would be a compulsory 6 a.m. church service

For my parents, Marek and Dana

Acknowledgements

I would like to thank my DPhil supervisor Gianluca Gregori for giving me the opportunity to work on this project as well as for the advice which he has given throughout. Sean Regan, the head of the experimental campaign at OMEGA deserves a special thanks for his efforts in putting the project together and in acting as a second mentor.

Thanks to the LLE staff who supported this technically difficult project. Thanks to Adam Baird for his assistance in all things electrical.

Thanks to Dirk Gericke for his discussions and feedback on the extensions to XRTS theory. Thanks to the late Basil Crowley, whose unending pursuit of theoretical precision was both an aid and an inspiration.

Thanks to Hugo Doyle, Matthew Oliver, Thomas White, Joseph Cross, Alexandra Rigby, Nicholas Hartley, Archie Bott, Jena Meinecke, and Paul Maybe for pitching in to set up the lab, sharing useful advice, and when all was dark and lost, for their pithy banter.

Thanks to Rachel for her immense support in the form of tea, sunny walks, and for being my whiteboard.

Contents

1

Introduction

Science may be described as the art of systematic over-simplification.
—Karl Popper

1.1 Temperature and density

Temperature and density are crucial parameters in understanding and predicting a wide variety of plasma phenomena, from the basic concepts of Debye shielding and plasma frequency to thermodynamic equations of state. Consequently, it is important to have refined techniques for accurately and precisely measuring temperature and density, and to have a number of independent methods so as to reinforce findings by consilience.

1.2 Ascertaining the state of a plasma

The statistical mechanical description of systems in equilibrium is one of the greatest successes of physics to date. One of the most important components of equilibrium physics is the notion of state.

A thermodynamic state is a system which is fully described at a point in time by a number of state variables. Another formulation is to say that the system may be described by an equation of state consisting of physically measurable parameters which uniquely define the state. Likewise, these functions of state must have a well-defined physical value for every possible equilibrium state of a system (1). This means that for a given state of a system, these variables have a value which is independent of the path taken to achieve that state. The parameters of state are the familiar properties of systems: temperature, density, pressure, ionization, entropy, and so on. A prominent example of an equation of state is the ideal gas law

$$pV = Nk_BT \tag{1.1}$$

where p, V, N, T are the pressure, volume, number of particles in, and temperature of an ideal gas system and k_B is Boltzmann's constant. One of the benefits of finding equations of state is that when given all but one of the state variables in a particular equation of state, it is possible to uniquely solve for the remaining state variable.

Plasmas may be classified by the importance of various physical effects, such as thermal, quantum, and correlation effects. In this manner, we may, at least partially, define a state as a particular temperature and density, as depicted in Figure 1.1.

These states can be further grouped through the dimensionless coupling parameter, $\Gamma_{\alpha,\beta}$, which is the ratio between energy due to the Coulomb potential and thermal energy of the particles (2):

$$\Gamma_{\alpha,\beta} = \frac{Z_\alpha Z_\beta e^2}{4\pi\epsilon_0 a_{\alpha,\beta} k_B T_{\alpha,\beta}} \tag{1.2a}$$

$$a_{\alpha,\beta} = \left(\frac{3\sqrt{Z_\alpha Z_\beta}}{4\pi n_e}\right)^{1/3} \tag{1.2b}$$

$$T_{\alpha,\beta} = \frac{m_\alpha T_\beta + m_\beta T_\alpha}{m_\alpha + m_\beta} \tag{1.2c}$$

α, β refer to the charged particle species (e.g. electrons, ions), Z is the ionization, e is the charge of an electron, ϵ_0 is the permittivity of free space, k_B is Boltzmann's constant, $a_{\alpha,\beta}$ is the interparticle separation, n_e is the electron density, $T_{\alpha,\beta}$ is the temperature, and m_x $(x = \alpha, \beta)$ is the particle mass.

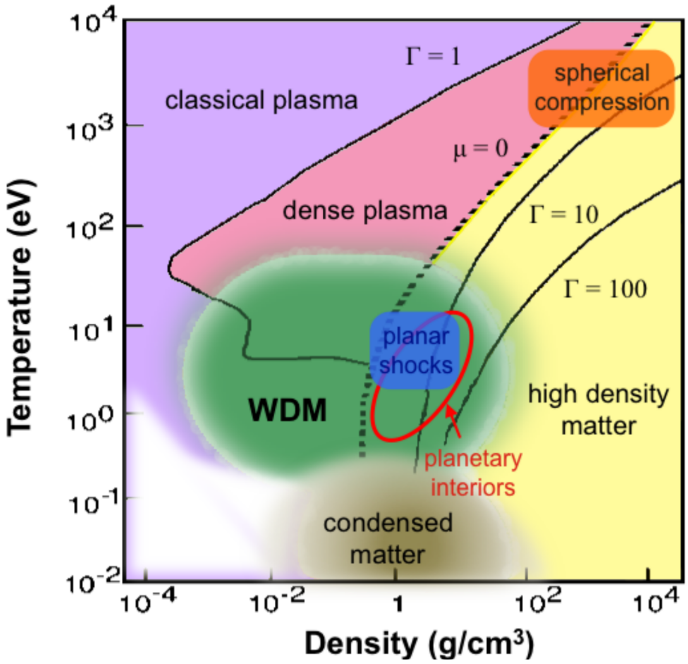

Figure 1.1: Plasma states described by temperature and density. Lines of constant coupling parameter separate the various regions. The most important of these is the $\Gamma = 1$ line which separates the strongly and weakly coupled regimes. Warm dense matter is between condensed matter and the hotter dense plasmas and classical plasmas. The $\mu = 0$ line (where μ is the chemical potential), signifying the separation above which thermal effects are important and below which quantum effects are important, cuts right through the WDM region, therefore requiring both effects in its description.

The ion-ion coupling factor is frequently used to define states of plasmas. For $\Gamma_{ii} \ll 1$, the thermal energy dominates over the Coulomb potential energy and the plasma may be treated as an ideal gas (*i.e.* collisionally dominated interactions). At $\Gamma_{ii} = 1$ collisions are superseded by electrostatic forces and we have a classical plasma. For $\Gamma_{ii} \geq 1$ the coupling of the plasma becomes significant and the electrostatic effects must be accounted for to adequately describe the state (3). Figure 1.1 gives an overview of the various plasma states and their coupling parameters.

A familiar equation of state, in the low temperature regime, is the Saha equation, which describes the degree of ionization for a plasma/gas as a function of temperature and density (4, 5, 6):

$$\frac{N_j}{N_k} n_e = \frac{1}{4a_o^3} \frac{g_j}{g_k} \left(\frac{k_B T_e}{\pi E_H} \right)^{3/2} \exp\left[-\frac{E_{jk}}{k_B T_e} \right] \tag{1.3}$$

where N_j and N_k are the number of atoms in the j and k energy states, n_e is the electron density, $a_o = 5.29 \times 10^{-9}\,\text{cm}$ is the Bohr radius, E_{jk} is the energy required to go from energy level k to j, g_j and g_k are the statistical weights of j and k, also known as the degeneracy, T_e is the electron temperature of the plasma, k_B is Boltzmann's constant and $E_H = 13.6\,\text{eV}$ is the ionization energy for a Hydrogen atom.

The Saha equation describes the balance between ionization, due to collisions by particles in the high energy tail of the energy distribution, and recombination with free electrons. It does not account for screening effects so it is only, strictly, valid for low temperature partially ionized gases/plasmas, even though it may serve as a useful approximation outside of this regime.

Ascertaining the state of a plasma is critical to understanding the dominant mechanisms in various regimes, ranging from classical plasmas to warm dense matter to high density matter. In the upper left corner of Figure 1.1 are the classical plasmas which are hot and not very dense. They may be approximated as purely thermal and weakly coupled, neglecting quantum and correlation effects. By contrast, in the low temperature limit, condensed matter is well described by focusing on quantum effects and neglecting thermal effects. Warm dense matter (WDM) sits directly in between these two regimes where neither approximation may be used. The need to account for both thermal and quantum effects makes WDM extremely complex.

It was already seen that knowing the temperature and density of plasma gives us much information on what effects we can expect to be important in a system. Knowing an equation of state for a particular regime would yield even more information, especially critical for computational modeling. For many systems it is sufficient to know the density, temperature and ionization of a plasma to infer something about the state.

Furthermore, accurate measurement of a state is important in most plasma physics experiments as it provides a baseline for characterization as well as comparison to other experiments. It is of special importance in the fields of inertial confinement fusion (where the compressed cryogenic pellet quickly passes through a number of transient states before arriving in the high density and temperature regime where fusion may occur) and in laboratory astrophysics, where exotic states (such as metallic hydrogen) in the centers of large gas giants are being explored (7). We are particularly interested in measuring the state of cryogenic deuterium in the WDM regime in order to confirm the equation of state, thereby providing a general expression for the behavior of deuterium in various regimes with possible applications to inertial confinement fusion. In addition, warm dense hydrogen is of great importance to describing the planetary dynamics for the formation of gas giants such as Jupiter, as well as how these gas giants maintain magnetic fields (8, 9). In particular, we wish to provide an experimental platform for confirming equations of state for hydrogen at pressures $\lesssim 10\,\mathrm{Mbar}$ where there is uncertainty along the Hugoniot (10, 11, 12).

1.3 Basic plasma definitions

Despite the wide range of plasma states in existence, many fundamental concepts are shared between these disparate states. For example, all forms of plasma have a notion of screening, even though screening for a classical plasma may be different than that of condensed matter. It is therefore informative to introduce these general concepts along with criteria which set apart the different instances to better define various states as well as the transitional regions between states.

Plasmas are defined as collections of freely moving particles in quasi-neutral systems. Plasmas have a significant proportion of charged particles, meaning the system is at least partially ionized. As a consequence, statistical fluctuations within a plasma system give rise to electromagnetic fields and collective behavior. In fact, what distinguishes a plasma from an ionized gas is the importance of collective behavior via these electromagnetic fields (4). In a weakly coupled plasma, thermal effects dominate over electromagnetic interactions and we may describe the plasma using familiar concepts from gas dynamics (13). The particle velocities in this classical plasma are governed by thermal effects, which are described by the Maxwell-Boltzmann distribution (1).

$$f\left(v\right)dv = \frac{4}{\sqrt{\pi}}\left(\frac{m}{2k_BT}\right)^{3/2} v^2 dv e^{-mv^2/2k_BT} \tag{1.4}$$

Placing a test charge into the plasma generates a Coulomb potential which attracts the oppositely charged particles in the medium and induces them to screen out the electric fields (4):

$$\phi\left(r\right) = \frac{e}{4\pi\epsilon_0 r}\exp\left(-\frac{r}{\lambda_{De}}\right) \tag{1.5a}$$

$$\lambda_{De} = \sqrt{\frac{\epsilon_0 k_B T_e}{e^2 n_e}} \tag{1.5b}$$

where ϕ is the electric potential as a function of distance r from the test charge, e is the charge of an electron, ϵ_0 is the vacuum permittivity, λ_{De} is the Debye length, T_e is the electron temperature, n_e is the electron density and k_B is Boltzmann's cosntant.

It is evident from the above equation that the electric potential emanating from a charge is reduced by an e-folding at one Debye length away, due to the collective effect of screening of oppositely charged particles in the plasma.

Continuing with kinetic theory, the dispersion relation for longitudinal Langmuir waves is given by the Bohm-Gross relation (14):

$$\omega^2 = \omega_p^2 + 3k^2 v_{th}^2\left(1 + 0.088 n_e \Lambda_e^3\right) + \left(\frac{\hbar k^2}{2m_e}\right)^2 \tag{1.6}$$

The first term on the right-hand side, ω_p, is the plasma frequency. In other words, it is the characteristic frequency of the simple harmonic oscillator solution for waves of charge displacement in a plasma, also known as plasmon waves (13):

$$\omega_{pe} = \sqrt{\frac{n_e e^2}{\epsilon_0 m_e}} \tag{1.7}$$

The second term represents thermal oscillations which are given by the thermal velocity of electrons

$$v_{th} = \sqrt{\frac{k_B T_e}{m_e}} \tag{1.8}$$

as well as the thermal wavelength of electrons

$$\Lambda_e = \frac{h}{\sqrt{2\pi m_e k_B T_e}} \tag{1.9}$$

where h is Planck's constant.

The third and final term is the quantum shift, where $\hbar$ is the reduced Planck's constant.

The dispersion relation is of the utmost importance to plasma physics experiments since it describes the relation between electromagnetic radiation and the medium. Incident electromagnetic radiation oscillates electrons which drive Langmuir waves within the plasma. Radiation of frequency lower than ω_p generates evanescent Langmuir waves which are not supported by the plasma and are instead reflected at the surface. We may replace plasma frequency with the frequency of incident radiation and invert eq. 1.7 to solve for the critical density:

$$n_c = \frac{\omega^2 \epsilon_0 m_e}{e^2} \tag{1.10}$$

The critical density defines the maximum density plasma which a radiation source of frequency ω may penetrate (15). This critical density is especially important to the study of WDM as it places strict constraints on which techniques may be used to probe the plasma. The standard technique of using an optical probe laser for Thomson scattering will not work for the high densities involved in WDM and we must instead turn towards the more complex x-ray Thomson scattering (XRTS). For regular optical Thomson scattering, interactions between photons and particles are elastic, meaning no energy is exchanged. For XRTS the energy of the photon is significantly larger than the rest mass of the particle $\hbar\omega \gg m_e c^2$ meaning that energy exchanges between the photon and the particle become important (16). This inelastic scattering is in fact Compton scattering which will be described in further detail in chapters 2 and 3.

Going back to Fig. 1.1 we see that as temperature reduces and density increases we move away from ideal, classical plasmas and towards the WDM and condensed matter regimes. In these regimes, the density is so large that the inter-particle separation is on the order of the particle's quantum oscillation wavelength:

$$\lambda_{DeBroglie} = \Lambda_e = \frac{h}{\sqrt{2\pi m_e k_B T_e}} \tag{1.11}$$

At sufficiently low temperatures the thermal distribution of the electrons no longer follows the standard Maxwell-Boltzmann and the electrons have become degenerate; they instead follow the Fermi statistics (13). The Debye screening length is no longer valid and is instead replaced by the Thomas-Fermi screening length:

$$\lambda_{TF} = \sqrt{\frac{2\epsilon_0 E_F}{3n_e e^2}} \tag{1.12}$$

where E_F is the Fermi energy as defined by:

$$E_F = \frac{\pi^2\hbar^2}{2m_e}\left(\frac{3n_e}{\pi}\right)^{2/3} \tag{1.13}$$

The corresponding Fermi temperature is given by $T_F = E_F/k_B$.

The relative importance of thermal and quantum effects may be summarized by the nondimensional degeneracy parameter:

$$\Theta = \frac{k_B T_e}{E_F} \tag{1.14}$$

This is a simple ratio of the thermal energy and quantum/Fermi energy. When $\Theta \approx 1$ thermal effects are on par with quantum effects and degeneracy begins to play an important role.

In the region transitioning between thermal and quantum effects neither the Debye length nor the Thomas-Fermi screening length suffice to describe the screening which is fundamental to WDM plasmas. Gericke *et al.* have suggested to use the Debye length formula while interpolating between the thermal and Fermi temperatures (17):

$$\kappa_e = \frac{1}{\lambda_s} = \sqrt{\frac{e^2 n_e}{\epsilon_0 k_B T_e^{eff}}} \tag{1.15}$$

where

$$T_e^{eff} = \left(T_e^4 + T_F^4\right)^{1/4} \tag{1.16}$$

Such an interpolation has yielded promising results with low errors across a large range of density values (17).

An alternative measure of the electron degeneracy is the Wigner-Seitz parameter:

$$r_s = \frac{d}{a_B} \tag{1.17}$$

where $a_B = 5.29 \times 10^{-11}$ m is the Bohr radius and $d = \left(\frac{3}{4\pi n_e}\right)^{1/3}$ is the interparticle spacing for electron density n_e. For $r_s < 1$ the size of the particle is larger than the spacing between the particles which results in a degeneracy comparable to the situation when Fermi energy dominates over the Coulomb potential. The electrons smear and form a uniform background resulting in weak electron-electron coupling, which is redefined as (2)

$$\frac{e^2}{dE_F} = 0.543 r_s \tag{1.18}$$

Besides electrostatic and quantum effects, collisions may play an important role in the evolution of a body of plasma. For example, if a plasma is in non-equilibrium, the particles collide and exchange energy through the process of thermalization until the system is returned to equilibrium. The characteristic length scale over which these collisions occur is given by the mean free path. The mean free paths for electron-ion and ion-ion collisions are given by (4, 18):

$$\lambda_{ie} = \frac{v_{e,th}}{\nu_{ii}\left(\frac{m_i}{2m_e}\right)^{1/2}\left(\frac{T_i}{T_e}\right)^{3/2}} \tag{1.19a}$$

$$\lambda_{ii} = \frac{v_{i,th}}{\nu_{ii}} \tag{1.19b}$$

where $v_{e,th}$ and $v_{i,th}$ are the electron and ion thermal velocities, respectively. ν_{ii} is the ion-ion collision frequency given by:

$$\nu_{ii} = n_i v_i 6\pi b^2 \ln\left(\frac{\lambda_{De}}{b}\right) \tag{1.20a}$$

$$b = \frac{e^2}{4\pi\epsilon_0 m_i v_i^2} \tag{1.20b}$$

where b is the impact parameter.

the mean free path is important for describing diffusive and viscous effects including the thickness of a shock (19). Most of the plasmas we will be covering in this thesis involve laser driven shocks.

Although for many plasmas, electromagnetic effects are more important then collisional effects, collisions cannot be ignored altogether. The Knudsen number is a measure of collisionality in a system and is defined as:

$$\mathrm{Kn} = \frac{\lambda_{\mathrm{mfp}}}{\mathrm{r_p}} \tag{1.21}$$

where r_p can be any characteristic distance, but for the purposes of this thesis we are particularly interested in the size of our diagnostic, or the thickness of the sheath. In particular, we will deal with Langmuir probes as a diagnostic which collects charged particles to measure the temperature and density of a plasma. When $\mathrm{Kn} \gg 1$ the plasma is collisionless and we only need to concern ourselves with inertial effects for describing the motions of charged particles as they are being collected by the probe. When $\mathrm{Kn} \ll 1$ collisional effects are important in the bulk of the plasma and they impede the effectiveness of the probe's electrostatic potential at attracting and collecting particles (20).

1.4 Non-equilibrium plasmas

To more fully understand a concept one should be aware of the limitations of its framework, therefore the following section should be treated as a caveat for the description of plasmas using state variables. When it comes to notions of state and parameters of state such as temperature and density, these are fundamentally equilibrium or near-equilibrium ideas. The further away one strays from certain assumptions of equilibrium the less valid these concepts become until, in some cases, they are completely inapplicable (21, 22).

There are, of course, approximations to retain the robustness of equilibrium theory even when straying away from equilibrium conditions. Arguably, the most important of such approximations is local thermodynamic equilibrium (LTE). As the name suggests, LTE is a situation where although the plasma system as a whole may not be considered to be in equilibrium, some smaller plasma element may be approximated as being locally in equilibrium, both spatially and temporally. The requirement here is that the plasma parameters vary slowly enough across the plasma, and in time, that effects due to gradients are small as compared to equilibrium effects (1, 23).

LTE may be described by a number of essentially equivalent statements:

- Detailed balance, where each process is equilibrated by its reverse (24)
- In spectroscopy, LTE may be defined as every energy level in an atom having population corresponding to the Saha-Boltzmann distribution value (23)
- Negligible net flow of matter or energy (transport properties) within the system or between the system under observation and any external system (1)

In contrast, net flows of matter and energy (transport properties) and violations of detailed balance are the critical feature of non-equilibrium systems. Although it is typically the case that non-equilibrium systems will rapidly thermalize and tend towards equilibrium, it has been shown by Glansdorff and Prigogine that under certain conditions non-equilibrium systems may be quasi-stable and reach a steady-state in non-equilibrium. These types of dissipative systems may be of great interest as the study of plasmas reaches for increasingly extreme conditions (21, 22). Later in this work (Chapter 3) we demonstrate one such case where the effect of strong gradients in a plasma is to completely violate detailed balance in the context of x-ray Thomson scattering, and therefore complicate the analysis required for extracting the temperature from the scattered spectra.

With this complication also comes the ability to extract information on gradients present in the plasma (25).

1.5 Laboratory astrophysics

In spite of the limitations imposed by equilibrium, the measurement of state variables can be a useful tool for characterizing phenomena which are significantly non-equilibrium. For example, turbulent energy may be quantified by examining fluctuations in temperature and density due to eddies, over time (20, 26). Experiments on the importance of turbulence in astrophysically relevant plasmas can provide a glimpse as to whether turbulence is a viable mechanism for amplification of magnetic fields observed in the intergalactic medium (27).

Equations of state are also relevant for modeling of planetary dynamics. It is thought that at the center of gas giants, such as Jupiter, are cores of WDM. An equation of state for WDM would not only prove useful for modeling the formation of Jupiter, but also in how Jupiter generates magnetic fields, analogous to Earth's magnetic dynamo (9).

One may ask, how can a small laboratory experiment be used to make inferences about massive astrophysical objects? On the one hand, there are certain physical properties which, to the extent of present knowledge, are invariant with respect to position in the universe. A carbon atom is always a carbon atom and will emit or absorb photons of particular energy resulting in spectral lines characteristic of carbon, so long as the relevant physical processes are similar.

This latter condition is all important, and it may, in fact, be quantified. Scaling parameters are nondimensional numbers which yield information on the relative importance of physical properties in a system. We've already seen one such number in the nondimensional degeneracy parameter eq. 1.14. The nondimensionality of these parameters allows us to compare physical processes for systems which may have many orders of magnitude in size between them.

Ryutov *et al.* have given a set of scaling parameters which allow us to compare magnetohydrodynamic systems (28). Cross *et al.* have extended this work to include quantum and radiative effects (29).

The present work is twofold. First, we examine and develop the application of XRTS to WDM experiments with the aim of providing detailed information on WDM sufficient to test proposed equations of state used in computational modeling. Second, we develop a high temporal resolution Langmuir probe with the aim of using it to quantify turbulent energy for laboratory astrophysics experiments on turbulent amplification of magnetic fields, as well as to further develop the theory of electrostatic probes embedded in supersonic flows. The following section will provide an overview of prior work in these two techniques.

1.6 Overview of previous experiments

Prior experiments with respect to the problem of warm dense matter were conducted as part of Dr. Katerina Falk's doctoral thesis under the Gregori group, in collaboration with Dr. Sean Regan at the Laboratory for Laser Energetics (LLE). Their work on designing and testing the platform for firing and probing cryogenic deuterium targets with XRTS probes is an invaluable foundation to the present work. They were able to assess the temperature and density of the shocked plasma using XRTS in the non-collective scattering regime. Those results were compared to 2D DRACO radiation-hydrocode simulations as well as independently verified using velocity-interferometry (VISAR) and streaked optical pyrometry (SOP) (30, 31) The experimental setup presented in chapter 4 of the present work is nearly identical to that of the prior experiments, except for the important distinction that the initial work was carried out in the non-collective regime whereas the present work is in the collective regime of x-ray Thomson scattering. It was found that the standard equilibrium assumptions for XRTS, used in the analysis of prior experiments, were insufficient for explaining the observed spectra in the collective regime. Chapter 3 presents an extension to XRTS theory for scattering off of media with strong gradients, while chapter 5 applies this extension to the analysis of experiments in the collective scattering regime. The extension to XRTS theory and the resulting analysis of XRTS spectra in the collective regime are consistent with the non-collective experiments done by Falk and Regan (30, 31, 32).

The Langmuir probe, on the other hand, is novel work within the Gregori research group and pushes the frontiers of this diagnostic on multiple fronts. Previous works have been able to reach temporal resolutions of $\sim$ 20MHz through a combination of improvements to swept voltage sources and the switch to using multiple probe tips as a work-around to limits on sweeping speeds (33, 34). It was primarily this jump to multi-tipped probes that the author has been able to exploit in designing a triple Langmuir probe which achieves a resolution of $\sim$ 200 MHz. Previous works primarily dealt with electron densities of $n_e \sim 10^{10} - 10^{12}$ cm^{-3} and at most $n_e \sim 10^{15}$ cm^{-3}. The probe presented in this work is composed of similar materials, but with robust circuit elements capable of transmitting higher currents. The short exposure time of the probe due to the rapid expansion of the shock assists in reaching higher currents which consequently allows probing of higher densities, around $n_e \sim 10^{17}$ cm^{-3}. These developments will allow for the use of Langmuir probes to assess temperatures and densities in laser produced shocks in regimes relevant to a range of astrophysical problems (18, 20).

1.7 Thesis outline and author's role in this work

This thesis will focus on two diagnostic techniques for measuring the temperatures and densities of plasmas, namely X-ray Thomson scattering (XRTS), and Langmuir Probes (LPs). XRTS is a high energy variant of classical Thomson scattering and has become a staple in the field of experimental plasma physics (3). Langmuir probes, are a principle diagnostic on space probes, in tokamaks and in industrial plasma deposition, but are not typically used in laser-driven experiments (35, 36, 37, 38, 39, 40, 41). This thesis will elaborate on the theory of each, explain in detail the innovations we are developing in XRTS theory and in LP design to push the boundaries of modern plasma research, and finally present the experimental setup and resulting data for both diagnostics.

As is the case with much of modern experimental physics, the research presented herein consists of a combination of collaborative and individual contributions. The purpose of this section and the thesis as a whole are to effectively convey the author's contributions to the field and to distinguish them from prior work and the contributions of collaborators. To this end, clear references will be made to acknowledge the work of others when it is presented. The chapter you have just read is an introduction to the fields of research examined in this thesis. By its nature, it is a review of foundational work laid down by others, along with open questions in these fields.

Chapter 2 is a more in depth examination of the theoretical background crucial to the author's work on XRTS and WDM. Much like chapter 1, it draws from a variety of sources which are referenced throughout.

Chapter 3 is the first chapter which deals with the author's original work in the field. It is concerned with an extension to XRTS theory in the collective scattering regime for inhomogeneous media and how this can be used to measure gradients in, for example, shocked plasmas. This work has been published in *Scientific Reports* in collaboration with the author's supervisor, Prof. Gianluca Gregori, who conceived of the project, Dr. Dirk Gericke, and the late Prof. Basil Crowley who provided theoretical guidance and Dr. Sean Regan who provided the relation to experimental data (31). The implementation of the code and simulations were carried out by the author. Initial prototypes of the code were written by the author and later implemented into Prof. Gianluca Gregori's XRS code.

Chapter 4 focuses on the technical details of the experimental campaign at the OMEGA laser facility, for probing WDM with XRTS in the collective scattering regime. Due to the similarity to prior experiments, much of the initial work was carried out by Dr. Katerina Falk, Prof. Gianluca Gregori, and Dr. Sean Regan with the immense support of the scientists and engineers at the Laboratory of Laser Energetics at the University of Rochester in New York. For the present work, some modifications were necessary to convert the targets and beam alignment procedures to collective scattering geometry. Target assembly was carried out by the LLE target fabrication laboratory overseen by Mark Bonino. The planning of the project was a shared endeavor between the author and Dr. Sean Regan. The author was involved in laser orientation and target development under the oversight of project leader, Dr. Sean Regan. Analysis of the x-ray backlighter brightness was conducted by the author.

Chapter 5 deals with the analysis of results from the OMEGA experimental campaign. The 2-D DRACO hydrodynamic simulations were done by Dr. Suxing Hu. The 1-D HELIOS simulations were done by the author with the use of Prism's HELIOS software. The analysis of XRTS spectra was carried out in whole by the author. The spectral fits using the random phase approximation (RPA), were carried out by the author using the XRS code written by Prof. Gianluca Gregori with the addition of an inhomogeneous theory implementation, as described in chapter 3, being written by the author.

Chapter 6 marks the beginning of the Langmuir probe portion of this thesis. Here, a brief overview is given of Langmuir probe theory with references given to various prior works. In addition, the design and characterization of a nanosecond resolution Langmuir probe is discussed in detail. The general probe design is based off of prior work, namely that of Gatsonis *et al.*, in creating a current-mode triple probe (36). Initial probe designs were drafted by the author and constructed by Adam Baird. Following the failure of these initial prototypes, substantial improvements accounting for high-frequency circuit effects were introduced by the author to achieve higher temporal resolution and robustness in the face of high density plasmas. The construction and characterization of these improved probes was entirely carried out by the author with technical advice from Adam Baird.

Chapter 7 outlines experiments on probing shock waves in laser-produced plasmas with a background gas fill. The purpose of these experiments was to characterize the shock expansion and compare temperatures and densities obtained from the newly constructed probe to those of interferometry and emission spectroscopy. Some background on interferometry, emission spectroscopy, and B-dots is given. It goes without saying that these are standard diagnostics whose theory is well established, therefore references are given as appropriate. The experiments were entirely conceived by the author with oversight from Prof. Gianluca Gregori. The experimental setup was done by the author with assistance from Matthew Oliver, Dr. Hugo Doyle, and Dr. Joseph Cross. The B-dots used to characterize the magnetic fields were constructed by Dr. Jena Meinecke and Adam Baird.

Chapter 8 presents the results of the aforementioned experiments using Langmuir probes. All aspects of the calibration and analysis were done by the author with advice from Prof. Gianluca Gregori.

Chapter 9 is a summary of the main results from this thesis. As with all good science, there is room for improvement, so the author has included proposals for future work. A list of publications by the author is given in the appendix.

2

Warm Dense Matter and XRTS

> *...long may Louise deBroglie continue to inspire those who suspect that what is proved by impossibility proofs is lack of imagination.*
>
> —John Stewart Bell, *On the Impossible Pilot Wave*

2.1 Introduction

As described in the introductory chapter, WDM is a complex state of matter. The complexity of WDM stems from the fact that it sits at the interface between classical plasma and condensed matter descriptions where neither thermal nor quantum effects may be totally neglected. Furthermore, WDM is characterized by a high coupling factor, thus correlations between ions are important, causing WDM to exhibit behavior similar to that seen in liquids.

Whenever a field poses theoretical problems, and in all good science, one invariably turns to experiments to help eliminate untenable theories and establish criteria for new theories. Unfortunately, WDM is notoriously difficult to diagnose by standard techniques. The high density eliminates the possibility of using most physical probing techniques and prevents all manner of optical techniques such as emission spectroscopy, interferometry, schlieren, shadowgraphy, and optical Thomson scattering. As a consequence, many of these optical techniques have been extended to x-ray energies which may penetrate the critical density barrier. One important technique is x-ray Thomson scattering (XRTS) which is capable of yielding a full description of the microscopic structure of a probed plasma.

Obtaining information on a plasma from XRTS requires a theory to describe the microscopic structure of the medium. Since the theories of WDM and XRTS must go hand in hand for XRTS to be a viable method in probing WDM plasma parameters, this chapter is devoted to the theoretical description of these two phenomena.

2.2 Warm Dense Matter

2.2.1 Statistical properties

Taking a statistical approach, we may begin to describe WDM using a one-component plasma (OCP) model. In the OCP model ions are treated as individual particles and electrons form an evenly distributed background charge which maintains quasineutrality of the system. Electrons at high temperatures can be approximated as forming a neutralizing background since they are much more mobile than the ions. Highly degenerate electrons also form such a background since their wavefunctions are smeared throughout the lattice. This smearing satisfies the Bloch functions (13, 42, 43). Using such an approximation we may describe the structure of a static many-body system by a function which yields the probability of finding ions at a given time and position. This is given by the *pair correlation function* which is the conditional probability density of a pair of particles being separated by a distance $\boldsymbol{r}$:

$$h(\boldsymbol{r}) = \frac{V}{N\left(N-1\right)}\left\langle \sum_{i\neq j=1}^{N} \delta\left(\boldsymbol{r}-\boldsymbol{r}_i+\boldsymbol{r}_j\right)\right\rangle \tag{2.1}$$

where N is the number of particles in the system and V is the volume of the system. The pair correlation function is normalized by:

$$\frac{1}{V}\int_V d^3r h(\boldsymbol{r}) = 1 \tag{2.2}$$

The *pair distribution function* is defined as

$$g(\boldsymbol{r}) \equiv h(\boldsymbol{r}) + 1 \tag{2.3}$$

The brackets in eq. 2.1 indicate that both the pair correlation and the pair distribution functions are statistical averages of all possible configurations of positions r_i and r_j for the pair of ions. The function is assumed to not contain holes, meaning that at least one ion is found at any given distance.

The *density-density correlation function* of a translationally invariant system is given as:

$$p(\boldsymbol{r}) = \langle \rho(\boldsymbol{r})\rho(0) \rangle = \langle \rho(\boldsymbol{r}+\boldsymbol{r'})\rho(\boldsymbol{r}) \rangle = \frac{1}{V} \left\langle \sum_{i,j=1}^{N} \delta\left(\boldsymbol{r}-\boldsymbol{r}_i+\boldsymbol{r}_j\right) \right\rangle \tag{2.4}$$

where the electron density operator and its Fourier transform are

$$\rho(\boldsymbol{r}) \equiv \sum_{i=1}^{N} \delta\left(\boldsymbol{r}-\boldsymbol{r}_i\right) \tag{2.5a}$$

$$\rho_{\boldsymbol{k}}(\boldsymbol{r}) \equiv \sum_{i=1}^{N} e^{-i\boldsymbol{k}\cdot\boldsymbol{r}_i(t)} \tag{2.5b}$$

We may further define the *static form factor* which is the Fourier transform of the spatial density distribution of the system of ions (2):

$$S(\boldsymbol{k}) = \frac{1}{N}\langle \rho_{\boldsymbol{k}}(0)\rho_{-\boldsymbol{k}}(0) \rangle = 1 + \frac{1}{N}\left\langle \sum_{i\neq j=1}^{N} e^{i\boldsymbol{k}\cdot(\boldsymbol{r}_i-\boldsymbol{r}_j)} \right\rangle \tag{2.6}$$

The static form factor is commonly used in x-ray crystallography where Bragg's Law yields Fourier space information on the lattice structure of crystals. The form factor yields the amplitude of the scattering signal off of the ions. It is evident from eqs. 2.1, 2.6 that the pair correlation function and the static form factor are related. The static form factor may therefore be reformulated in terms of the pair distribution function:

$$S(\boldsymbol{k}) - 1 = \frac{N-1}{V}\int d^3 r e^{-i\boldsymbol{k}\cdot\boldsymbol{r}}\left[g(\boldsymbol{r})-1\right] \tag{2.7}$$

This formulation brings to light the dependence of the scattering signal on the pair distribution of the ions. One can simulate the form factor by obtaining the ion distribution from a wide variety of approaches, including, but not limited to: density-functional theory molecular dynamics (DFT-MD), Thomas-Fermi models, or path integral Monte Carlo (PIMC) simulations. The model can then be confirmed by fitting the simulated spectra to those obtained experimentally (42, 44, 45, 46).

When it comes to probing WDM with XRTS, the static form factor is insufficient. This is because XRTS involves not only *elastic scattering*, where the particle and photon energies are the same before and after scattering, but also *inelastic scattering* via the Compton effect, where energy exchange takes place between the photon and the scattering particle. This exchange of energy may be viewed as a temporal dependence, since time and energy are Fourier transforms of one another. Therefore, we must include the dynamics of the system, and we do this by introducing the dynamic structure factor (DSF). The DSF describes the density-density correlations in Fourier space and is defined as:

$$S\left(\boldsymbol{k},\omega\right) \equiv \frac{1}{2\pi N}\int dte^{i\omega t}\left\langle \rho_{\boldsymbol{k}}(t)\rho_{-\boldsymbol{k}}(t)\right\rangle \tag{2.8a}$$

$$\rho\left(\boldsymbol{k},\omega\right) = \frac{1}{2\pi}\int dte^{i\omega t}\rho_{\boldsymbol{k}}(t) \tag{2.8b}$$

where $\rho\left(\boldsymbol{k},\omega\right)$ is the space-time Fourier transform of the density operator.

The corresponding dynamic density-density correlation function can be written as:

$$G\left(\boldsymbol{r},t\right) = \int \left\langle \rho_{\boldsymbol{k}}\left(\boldsymbol{r}+\boldsymbol{r}',t\right)\rho_{\boldsymbol{k}}\left(\boldsymbol{r}',0\right)\right\rangle d\boldsymbol{r}' \tag{2.9}$$

Much as the static form factor could be expressed in terms of the pair distribution function, the dynamic structure factor is related to the density-density correlation function $G\left(\boldsymbol{r},t\right)$. This means that the amplitude of the scattered signal as expressed by the dynamic structure factor, is created by both the spatial and temporal density fluctuations expressed in the density-density correlation function.

Up to this point the discussion of the dynamic structure factor has involved the one-component plasma approximation where the background of negative charges exists only for quasineutrality and does not participate in screening effects. In real plasmas screening effects are of the utmost importance and we may take them into account by introducing an *effective, quasi-particle density* or *dressed particle*:

$$\rho\left(\boldsymbol{k},\omega\right) \equiv \frac{\rho^0\left(\boldsymbol{k},\omega\right)}{\epsilon\left(\boldsymbol{k},\omega\right)} \tag{2.10}$$

where $\epsilon\left(\boldsymbol{k},\omega\right)$ is the *dielectric response function* of the medium and the superscript "0" denotes non-interacting particles, as in the idealized OCP case. Requiring that $\rho\left(\boldsymbol{k},\omega\right)$ and $\rho^0\left(\boldsymbol{k},\omega\right)$ be real quantities we obtain $\epsilon\left(-\boldsymbol{k},-\omega\right) = \epsilon\left(\boldsymbol{k},\omega\right)^*$ where * denotes the complex conjugate. From this relation we can express a dynamic structure factor with screening effects as:

$$S\left(\boldsymbol{k},\omega\right) = \frac{S^0\left(\boldsymbol{k},\omega\right)}{\left|\epsilon\left(\boldsymbol{k},\omega\right)\right|^2} = \frac{1}{\left|\epsilon\left(\boldsymbol{k},\omega\right)\right|^2}\int d^3v f(\boldsymbol{v})\delta\left(\omega-\boldsymbol{k}\cdot\boldsymbol{v}\right) \tag{2.11}$$

This is also known as the *fluctuation-dissipation theorem*, it relates the spectrum of density fluctuations of charges in a system to the dielectric response function. The fluctuation-dissipation theorem is a common method of statistically describing relatively small deviations from equilibrium via dissipations which return the system back to equilibrium (1). When incident radiation scatters off electrons, it perturbs the system and both the fluctuations and response are described by eq. 2.11. The DSF is therefore the spectrum of radiation scattered by the particles in the system. The fact that the DSF is expressed in terms of the dielectric function is crucial, since this provides a convenient link to linear response theory and the measures of electric and thermodynamic properties of the system. It also provides us with a means of further extending the theory into a wider range of non-equilibrium systems (13).

2.2.2 Dynamic structure factor

The total electron-electron dynamic structure factor may be derived using a chemical model as shown by Chihara (47).

$$S_{ee}^{tot}\left(\mathbf{k},\omega\right) = \left|f_I(\mathbf{k})+q(\mathbf{k})\right|^2 S_{ii}\left(\mathbf{k},\omega\right) + Z_f S_{ee}^0\left(\mathbf{k},\omega\right) + Z_c\int \tilde{S}_{ce}\left(\mathbf{k},\omega-\omega'\right) S_s\left(\mathbf{k},\omega'\right) d\omega' \tag{2.12}$$

The total dynamic structure factor breaks down into different terms which are known as the ion feature, electron feature, and the bound-free transitions, which correspond to the first, second and third terms on the right-hand side of eq. 2.12 respectively. This expression is valid even in the regime where the incident radiation is higher than the ionization energy $\hbar\omega_0 \gg E_I$.

$f_I(k)$ is the distribution of electrons tightly bound to nuclei and $q(k)$ is the screening term, that is the free and valence electrons which follow ions and establish screening of electric fields. Z_f represents the free electrons and Z_c represents the core electrons where it is understood that free electrons are those which have been ionized and are no longer bounded to an ion whereas the core electrons are those which remain bound to an ion. The sum of Z_f and Z_c must be the total number of electrons for the neutral atom. $S^0_{ee}(k,\omega)$ accounts for the free electrons, in particular it is the high frequency component of the electron-electron correlation function. The last term accounts for inelastic scattering due to bound-free transitions of core electrons, those electrons which are neither free nor in the valence shell. $S_{ce}\left(k,\omega\right)$ describes Raman transitions of core electrons to continuum. $S_s\left(k,\omega\right)$ is the dynamic structure factor for a single ion and it compensates for self-motion of the ion when simulating inelastic processes.

2.2.2.1 Ion term

In the weakly coupled regime the ion feature is well approximated by models like Debye-Hückel

$$S_{ee}(k) \equiv S_{DH}(k) = \int d\omega S_{ee}\left(k,\omega\right) = \frac{k^2}{k^2 + k_{De}^2} \tag{2.13}$$

where $k_{De} = 1/\lambda_{De}$ is the wavenumber corresponding to the Debye length.

Unfortunately, such weakly coupled approximations may not be used in the high density, strongly coupled regime which is of interest for WDM studies. In general, models for the ion structure factor $S_{ii}\left(k,\omega\right)$ in the strongly coupled regime are a continuing problem of exceeding complexity requiring the description of quantum electron-ion potentials or screening models. A naive approach may be taken with the *frozen core approximation* where bound-free transitions are ignored, so that $\lim_{k\to 0} f_I(k) = Z_c$. The approximation also treats ions adiabatically and the ion-ion DSF is simplified to a delta function of the form:

$$|f_I(\mathbf{k}) + q(\mathbf{k})|^2 \, S_{ii}\left(\mathbf{k},\omega\right) = \left| Z_c + \sqrt{Z_f}\frac{S_{ei}(\mathbf{k})}{S_{ii}(\mathbf{k})} \right|^2 S_{ii}(\mathbf{k})\delta(\omega) \tag{2.14}$$

where $S_{ei}(\mathbf{k})$ and $S_{ii}(\mathbf{k})$ are the static electron-ion structure factor and the static ion-ion structure factor respectively (3). The screening function $q(k)$ for a fully ionized system is defined as a function of the partial structure factors in an electron-ion system $q(\mathbf{k}) = \sqrt{Z_f} S_{ei}(\mathbf{k})/S_{ii}(\mathbf{k}) = Z\left(k_{De}/k\right)^2 S^0_{ee}$ In this form, it is evident that corrections to S^0_{ee} will affect $q(\mathbf{k})$ and, in turn, affect the ion feature in the total dynamic structure factor. Such corrections will have a significant impact for low-Z elements where the ratio of free to bound electrons is large. The ionic form factor $f_I(\mathbf{k})$ may be modeled using eletron-wave functions such as the Hartree-Fock (HF) self-consistent field (SCF) method; these often yield more precise results (48, 49, 50).

The ion-ion static form factor $S_{ii}(\mathbf{k})$ can be obtained from the one-component plasma (OCP) model discussed earlier. Although the model works quite well for strongly coupled and highly degenerate systems, it can fall short due to the treatment of ions as point-like and neglect of electron-ion polarization effects. This can be ameliorated by treating the ions as *charged hard spheres* of finite size. Further developments to the OCP model include screening effects and extensions to partially ionized matter. Screening effects are introduced by using the linear screening approximation in the limit where electron-ion coupling is weak:

$$S_{ii}^{SOCP}(\mathbf{k}) = \frac{S_{ii}^{OCP}}{1 + f_v(\mathbf{k})S_{ii}^{OCP}} \tag{2.15}$$

where $f_v(\mathbf{k})$ is the screening correction for bare ion-ion interaction and S_{ii}^{OCP} is OCP ion-ion structure factor with no screening and ions of finite size.

The SOCP model is extended to the partially ionized regime by introducing pseudopotentials which allow for negative screening, hence the name SOCPN, where “N” stands for negative. The negative screening is a known effect where bound electrons repel valence electrons and reduce screening at short distances from the nucleus. This is modeled as a pseudopotential with an empty core and a soft cut off (17).

An alternative approach for obtaining the static structure factor is through the use of a hypernetted chain (HNC) equation to solve for the pair correlation function $h(r)$. The HNC scheme involves the use of *direct correlation function* $c(r)$ and an expanding series of integral equations:

$$h\left(1,2\right)=c\left(1,2\right)+\int c\left(1,3\right)c\left(3,2\right)d3+\int\int c\left(1,3\right)c\left(3,4\right)c\left(4,2\right)d3d4+... \tag{2.16}$$

The first order (first term on the right hand side) accounts for the interaction of two neighboring bodies with specific effective potentials. The second order builds on this by treating interactions between a third particle and the first order pair. The higher orders add more interacting ions in similar fashion. In the homogeneous case, the chain reduces to the Ornstein-Zernike relation which can be solved analytically (42, 51). Short-range effects can be included through the use of quantum pseudo-potentials to approximate diffraction and exchange effects in dense electron-ion systems (13, 52, 53).

Simulations of ion feature effects should be taken with a grain of salt, as much of it depends on the choice of potentials and screening approximations (54). This uncertainty in choice of model leads to variability in simulating the inelastic (Compton effect) and elastic (Rayleigh-like) scattering features. Therefore, the present work will be primarily concerned with the free electron feature and the more tractable problems which may be tackled therein.

2.2.2.2 Free electron term

The free electron feature is expressed as a function of ion and free electron structure factors:

$$S_{ee}\left(\mathbf{k},\omega\right)=\frac{\left|q(\mathbf{k})\right|^{2}}{Z_{f}}S_{ii}\left(\mathbf{k},\omega\right)+S_{ee}^{0}\left(\mathbf{k},\omega\right) \tag{2.17}$$

where the electron-ion structure factor is related to the ion-ion structure factor by $S_{ei}\left(\mathbf{k},\omega\right)=\frac{|q(\mathbf{k})|}{\sqrt{Z_f}}S_{ii}\left(\mathbf{k},\omega\right)$. In many WDM experiments electron-electron correlations are weak and we may neglect non-linear terms. The idealized, non-interacting DSF for a Boltzmann distribution is then given by

$$S_{ee}^{id}\left(\mathbf{k},\omega\right)=\frac{N}{\pi\omega}\frac{k^{2}}{k_{De}^{2}}\,\mathrm{Im}\left[\epsilon\left(\mathbf{k},\omega\right)\right] \tag{2.18}$$

This is then substituted in place of $S^0(\boldsymbol{k},\omega)$ in the fluctuation-dissipation relation eq 2.11 to obtain:

$$S^0_{ee}(\mathbf{k},\omega) = -\frac{\hbar}{1-\exp\left(-\hbar\omega/k_B T_e\right)}\frac{\epsilon_0 k^2}{\pi e^2 n_e}\,\mathrm{Im}\left[\frac{1}{\epsilon\left(\mathbf{k},\omega\right)}\right] \tag{2.19}$$

The first ratio on the right hand side represents the detailed balance constraint which ensures that the DSF obeys

$$S\left(\mathbf{k},\omega\right) = \exp\left(-\hbar\omega/k_B T_e\right) S\left(-\mathbf{k},-\omega\right) \tag{2.20}$$

for a system in local thermodynamic equilibrium (13).

The dependence of the dynamic structure factor on the imaginary component of the reciprocal of the dielectric function is as a consequence of the dissipative nature of scattering. In general, the imaginary components of linear response functions represent dissipative processes whereas the real components represent conservative processes, although if there is dispersion in the real component this will be included in the imaginary component as well. (55, 56). This means that the electron correlations are implicit in the dielectric function, and it is assumed that the system responds linearly to a perturbation.

The dielectric function can be derived from the Vlasov equation (50, 57) for a plasma where collisions are negligible. For degenerate matter with weak interparticle interactions, the random phase approximation (RPA) may also be used for deriving the dielectric function. In this case, we may take the dielectric function for the finite temperature RPA to be expressed by (57):

$$\epsilon\left(\mathbf{k},\omega\right) = 1-\frac{e^2}{\hbar\epsilon_0 k^2}\int\frac{f\left(\boldsymbol{p}+\hbar\boldsymbol{k}/2\right)-f\left(\boldsymbol{p}-\hbar\boldsymbol{k}/2\right)}{\boldsymbol{k}\cdot\boldsymbol{p}/m_e-\omega-i\nu}\frac{2d^3p}{\left(2\pi\hbar\right)^3} \tag{2.21}$$

with $\nu \to 0^+$ and where $\boldsymbol{p}$ is the electron momentum.

The distribution function $f(\boldsymbol{p})$ is the Fermi-Dirac distribution so that the response function describes degenerate electrons:

$$f(\boldsymbol{p}) = \frac{1}{\exp\left(\frac{p^2/2m_e-\mu}{k_B T_e}\right)+1} \tag{2.22}$$

Here, μ is the chemical potential energy as interpolated between classical and quantum theories and can be expressed as (13, 50)

$$\frac{\mu}{k_B T_e} = -\frac{3}{2}\ln\Theta + \ln\frac{4}{3\sqrt{\pi}} + \frac{A\Theta^{-b-1} + B\Theta^{-(b+1)/2}}{1 + A\Theta^{-b}} \tag{2.23}$$

where Θ is the degeneracy parameter as given in eq. 1.14, and the coefficients are $A = 0.25945$, $B = 0.072$, $b = 0.858$ (13, 50).

Eq. 2.22 reduces to the Maxwell-Boltzmann function in the limit of $T \to \infty$ such that the interpolation remains valid for classical plasmas. It is important to notice that the above treatment takes the thermal, statistical properties of the system from the uncorrelated electron distribution function and summarizes them into the linear response of the system such that the measured scatter spectra are then, inextricably, a function of the thermodynamics of the system (50). As a consequence, the DSF depends on the temperature, and the electron temperature may be inferred from the free electron Compton feature in the scattered spectra.

Landau's formulation of the dielectric response as a function of the electron distribution is robust in that it allows us to derive dynamic structure factors for different regimes by using a different distribution function; the Debye-Hükel theory is an example of this (58). In the limit of weak ion-ion coupling in a collisionless plasma we may substitute the Maxwell-Boltzmann distribution into eq. 2.21 and obtain:

$$S_{ee}(k) \equiv S_{DH}(k) = \int d\omega S_{ee}\left(k,\omega\right) = \frac{k^2}{k^2 + k_{De}^2} \tag{2.24}$$

where $k_{De} = 1/\lambda_{De}$ is the wavenumber corresponding to the Debye length. The Debye-Hückel formulation can be corrected to include screening effects by taking the inverse Fourier transform of eq. 2.24 and adjusting it by the exponential form of the Debye-shielding model to give: $g(r) = -\frac{k_{De}^2}{4\pi n_e r} e^{-rk_{De}}$ (2, 42).

Both the RPA and Debye-Hückel models become invalid when electron-electron coupling becomes important $\Gamma_{ee} > 1$, as may be the case for experiments on warm dense matter. Coupling may be introduced through the *local field correction* where a parameter $G\left(k\right)$ compensates for the short-range correlations and the strong coupling ignored in the previous models (13). The static electron structure factor becomes:

$$S_{ee}(k) = \frac{k^2}{k^2 + k_{De}^2\left[1 - G(k)\right]} \tag{2.25}$$

In the low frequency limit $G(k)$ is obtained from the compressibility rule and in the high frequency limit it is given by the parametrized relation (2, 54, 59, 60). In the low coupling limit $G(k) = 0$ and the DSF reduces back to RPA or Debye-Hückel.

2.2.2.3 Bound-free transitions

Bound-free transitions are expressed in the third term on the right hand side of eq. 2.12. These transitions must include the details of the atomic structure which is influenced by environment of particles as well as the x-rays used for probing. In a plasma, there are many freely moving electrons which affect the electronic states in the atom, making the modeling of bound-free transition a complex subject.

The *continuum lowering* effect can be seen in dense and strongly coupled plasmas where the proximity of ions causes the atomic potentials to depress the ionization potential of the electrons in neighboring ions. The continuum lowering effect has been observed in experiments (61, 62). The effect depends on the number of ions which affect the potential of a test ion, which in turn, depends on the screening length due to the Coulomb force (3). Stewart and Pyatt derived a continuum lowering model based on the finite-temperature Thomas-Fermi model by using an effective screening length to compensate for the breakdown of the Debye screening length for dense plasmas (63). Other approaches involving Pauli blocking, dynamic screening, and statistical correlations for bound states can effectively model pressure ionization (Mott effect) by maintaining a constant binding energy while lowering the continuum until it merges with the highest bound states (64). A prominent method for simulating Compton interactions for bound-free scattering is the *impulse approximation*. In the impulse approximation, the potential between charges does not change due to the interaction so the energy exchange is given by the initial and final states (65).

In general, the bound-free term is quite small as compared to the electron feature and only generates a weak background signal due to the Raman bandwidth being comparable to the Compton feature (3, 66). The simulations and experiments presented in the remainder of this work are primarily concerned with hydrogen in the WDM regime where there are few electrons in the core states and therefore the bound-free transitions can be ignored.

2.3 X-ray Thomson scattering

2.3.1 Scattering power

Thomson scattering is a process by which incident electromagnetic radiation accelerates a charged particle and the particle re-emits radiation in response to being accelerated. Thomson scattering is the limiting case of Compton scattering in that we are treating low frequencies ω such that $\hbar\omega \ll m_e c^2$ (3). There is a caveat, in X-ray Thomson Scattering, the photon energy is sufficiently large that Compton Scattering must be accounted for because $\hbar\omega \gg m_e c^2$. This process of photon re-emission can be intuitively described by the classical electrodynamic concept of retarded potentials generated by accelerating charges. These retarded potentials generate a radiated power output in the shape of a deformed donut in the lab frame, which in the rest frame of the charged particle is a regular donut shape (16).

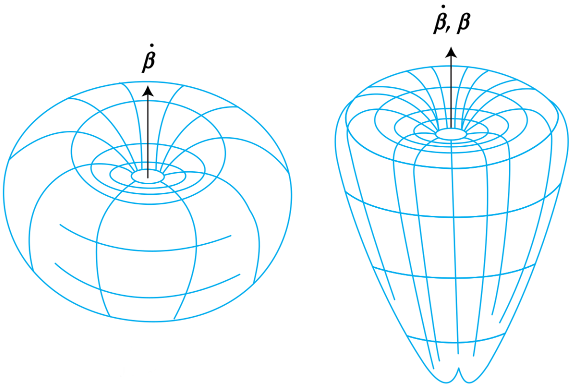

Figure 2.1: Donut shaped power radiated by an accelerating charge as modeled by retarding potentials (16).

Through the use of statistical mechanics we can gain a deeper understanding of how a collection of particles forming the plasma will scatter light from an incoming probe beam.

The DSF is directly related to the power of the scattered spectrum of the probe beam via (67):

$$\frac{d^2\sigma}{d\Omega d\omega} = \sigma_T \frac{k_1^2}{k_0^2} S\left(\boldsymbol{k}, \omega\right) \tag{2.26}$$

where $\sigma_T = \frac{8\pi}{3} r_0^2 = 6.65 \times 10^{-25}$ cm^2 is the Thomson scattering cross-section, $r_0 = \frac{e^2}{4\pi\epsilon_0 m_e c^2} = 2.82 \times 10^{-15}$ cm^2 is the classical radius of the electron, k_0 and k_1 are the wavevectors of the incident and scattered beams respectively. $\boldsymbol{k} = |\boldsymbol{k_0} - \boldsymbol{k_1}|$ is the difference in the incident and scattered wavevectors, and ω is the frequency of the incident beam (50).

$S(\boldsymbol{k}, \omega)$ will have some implicit dependence on the retarded potentials of the electrons, as depicted in Figure 2.1, so it is intuitive that $S(\boldsymbol{k}, \omega)$ will vary with scatter angle. There are multiple approaches to deriving analytical expressions for the DSF. One-component plasma approximation (OCP) and its extensions SOCP (screened OCP) and SOCPN (SOCP "negative") are typically used to derive the ion component of the DSF. SOCP uses the Coulomb potential to derive the screening function $q\left(k\right)$, while SOCPN uses pseudo-potentials which allow for negative screening. The first is only applicable for fully ionized systems while the latter is applicable to partially ionized systems. Other DSF terms are obtained using: Thomas-Fermi theory, chemical models, density-function theory molecular dynamics and path integral Monte Carlo simulations (44, 45, 46, 68, 69). Furthermore, it is important to note that the aforementioned treatment of the DSF only applies to free-free scattering.

2.3.2 Collective and non-collective scattering

In addition to the above, it is important to determine the scattering parameter, α, which compares the scale at which fluctuations in the plasma are probed to the scale length of the plasma screening (70).

$$\alpha \equiv \frac{1}{k\lambda_s} \tag{2.27}$$

where k is the wavenumber given by the relation $\lambda = \lambda_0 / 2\sin(\theta/2)$, θ is the scattering angle, λ_0 is the wavelength of the incident probe beam, and λ_s is the screening length of the plasma. It is in the calculation of this α-parameter that the relevant screening lengths discussed in the introductory chapter become important.The screening length can either be the Debye length, or for sufficiently degenerate plasmas, the Thomas-Fermi screening length.

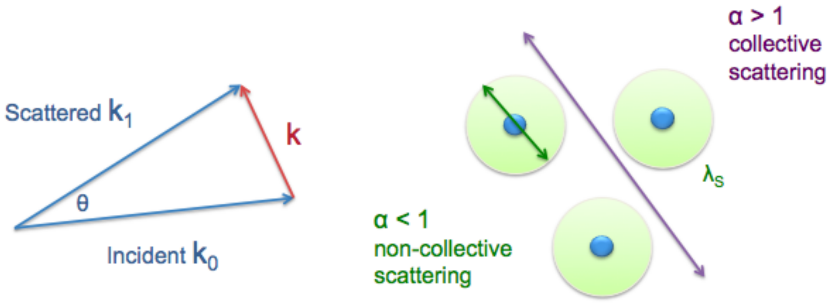

Figure 2.2: Left: a diagram showing the wavevector, **k**, as compared to the incident and scattered wavevectors. Right: Collective and non-collective Thomson scattering off a plasma

For $\alpha < 1$ the scattering scale length is smaller than the screening length and we obtain scattering off of individual particles, or *non-collective scattering*. For $\alpha > 1$ the various individual scatter sites interfere at distances larger than the screening length to yield *collective scattering*, thereby giving information on plasmon waves supported by the medium. Typically the dielectric function used in the dynamic structure factor may be expressed as

$$\epsilon\left(\boldsymbol{k},\omega\right) = 1 + \chi(\alpha^2) \tag{2.28}$$

where the second term on the right hand side is merely indicating the dependence of χ on the square of the alpha parameter. For non-collective scattering the dielectric susceptibility approaches unity and the scattered spectrum is simply the Doppler contributions of individual scatterers. On the other hand, for collective scattering, the χ term becomes important and inelastically, upshifted and downshifted plasmon signals at a distance of $\sim \hbar\omega_p$ from the quasi-elastic peak are witnessed in the scattered spectrum. Note, the Compton recoil, $E_C = \hbar^2 k^2/2m_e$, also plays a part in defining the shift between elastic and inelastic signals, in the dispersion relation give by Eq. 1.6.

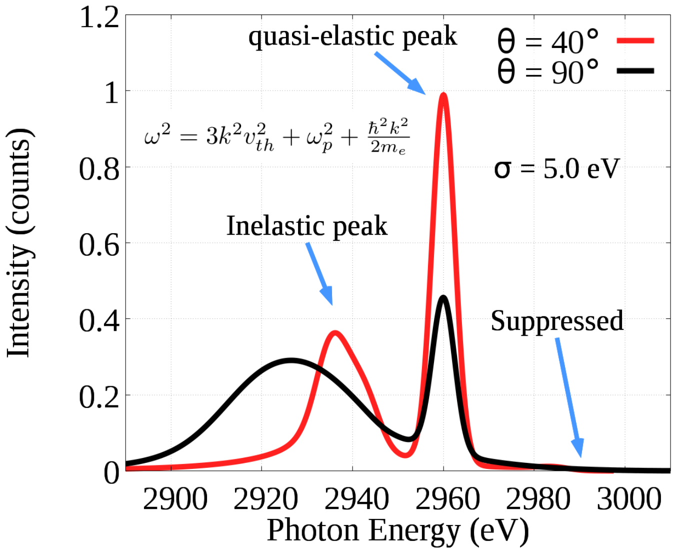

Figure 2.3: *Black*: Non-collective scatter simulation off warm dense deuterium with $\alpha = 0.8$. *Red:* Collective scatter simulation for the same plasma parameters but with $\alpha = 1.6$. The values used for the simulations were $E_0 = 2960$eV, $T_e = 8$eV, $n_e = 2.2 \times 10^{23}\,\text{cm}^{-3}$, $Z = 0.8$, convolved with a Gaussian instrument function with $\sigma = 5\,\text{eV}$. The RPA model was used to generate these simulations.

In Figure 2.3 we show the results of XRTS simulations in the collective and non-collective regimes. These simulations were done for deuterium at $n_e = 2.2 \times 10^{23}\ \mathrm{cm}^{-3}$, $T_e = 8\ \mathrm{eV}$, $Z = 0.8$, with a probe beam of $E_0 = \hbar\omega = 2960\ \mathrm{eV}$ at two different scatter angles $\theta = 40^\circ$ and $\theta = 90^\circ$ corresponding to $\alpha = 1.6$ and $\alpha = 0.8$ respectively. In the collective scatter spectrum you can clearly identify the downshifted plasmon peak while in the non-collective spectrum this peak is significantly broadened. When the experiment is in the non-collective regime it is mainly sensitive to temperature. In the degenerate case this is the Fermi temperature which is proportionate to the electron density $T_F \propto n_e^{2/3}$. In the classical case the DSF is related to the Maxwell-Boltzmann distribution function making the spectrum sensitive to electron temperature via Doppler broadening. In the collective scattering regime, the ratio of the upshifted and downshifted plasmon intensities is related to detailed balance which can be used as a measure of temperature (3, 71, 72).

$$\frac{S(\mathbf{k},\omega)}{S(-\mathbf{k},-\omega)} = \exp\left[\frac{-\hbar\omega}{k_B T_e}\right] \tag{2.29}$$

It is evident from the Bohm-Gross dispersion relation Eq. 1.6 that the plasmon shift away from the elastic peak is dependent on the plasma frequency. Therefore the shift is sensitive to the density of the plasma by $\omega_{pe} \propto n_e^{1/2}$. The elastic peak is a quasi-Rayleigh feature, in that while it appears to be elastic from the perspective of free-free scattering, if we were to resolve the peak we would see two inelastically shifted ion feature peaks.

2.4 Equation of state models

For classical plasmas we may describe the equation of state for internal energy through the ideal gas equation $E_{int}^{ideal} = 3Nk_BT/2$. For strongly coupled plasmas, this is insufficient and we need to include Coulomb interactions. In the OCP model the internal energy may be expressed as the sum of classical and Coulomb terms:

$$\frac{E_{int}}{N} = \frac{3}{2}k_BT + \frac{1}{2V}\sum_{k\neq 0} V_k\left[S(\mathbf{k}-1)\right] \tag{2.30}$$

where V_k is the Fourier transform of the Coulomb potential. Here, the second term, representing the Coulomb interactions, is a function of the structure factor $S(\mathbf{k})$, which can be obtained from Thomson scattering measurements. We may then invoke the *virial theorem* and incorporate this into an equation of state

$$\frac{P}{P_{ideal}} = 1 + \frac{1}{3}\frac{E_{int} - E_{int}^{ideal}}{Nk_BT} \tag{2.31}$$

where $P_{ideal} = Nk_BT$ is the ideal gas pressure. This equation only accounts for pressure of the ions. When electron pressure is important, alternative derivations which include degeneracy and quantum corrections are available (42).

EOS in hydrodynamic simulations

This work focuses on the SESAME and PROPACEOS equation of state tables which were used in DRACO 2D radiation hydrodynamic (rad-hydro) and HELIOS 1D rad-hydro codes to simulate the deuterium shock produced in the XRTS experiments at the OMEGA laser facility.

DRACO was created at LLE to model spherical compression and planar targets (73, 74). The simulations presented in this work use DRACO simulations in Lagrangian coordinates. The equation of state of deuterium was obtained from SESAME tables; these tables use a chemical model developed by Kerley (68, 75). Chemical models typically assume independent bound configurations interacting via pair potentials while treating electrons as a uniform neutralizing background, similar to OCP. The model used in SESAME contains corrections based in experimental data as chemical models are strictly classical and lack quantum/degeneracy effects which occur at higher densities. The EOS consists of three phases for deuterium, fluid, molecular solid, and metallic solid, and includes effects from ionization, dissociation, and first-order mixing of molecular and atomic fluid phases. For reference, the SESAME tables used in this work were numbers 5263, and 5265.

HELIOS was developed by Prism to simulate laser-produced and z-pinch plasmas (76). The code allows for planar, cylindrical and spherical target geometries and generates a spatially divided mesh for the target, the resolution of which can be set. Given a set of initial conditions: composition, density, drive intensity, the code simulates evolution in time in Lagrangian coordinates. In the present work, the Spitzer thermal conductivity model was used along with a multi-frequency flux-limited diffusion model for simulating radiation transport. PROPACEOS (PRism OPACity and Equation of State) tables were used for equation of state and opacity models in the simulations. Just like SESAME tables, PROPACEOS is based on the chemical model and should provide comparable results to DRACO simulations.

3

XRTS in inhomogeneous media

> *There is of course no sharply defined boundary between what is to be treated as microscopic and what as macroscopic, and this introduces a basic vagueness into [the usual formulation of] fundamental physical theory.*
>
> —John Stewart Bell, *Measurement Theory of Everett and De Broglie's Pilot Wave*

3.1 Introduction

Thomson scattering of laser light is one of the most fundamental diagnostics of plasma density, temperature and magnetic fields. It relies on the assumption that the properties in the probed volume are homogeneous and constant during the probing time. On the other hand, laboratory plasmas are seldom uniform and homogeneous on the temporal and spatial dimensions over which data is collected. This is particularly true for laser-produced high-energy-density matter, which often exhibits steep gradients in temperature, density and pressure, on a scale determined by the laser focus. Here, we discuss the modification of the cross section for Thomson scattering in fully-ionized media exhibiting steep spatial inhomogeneities and/or fast temporal fluctuations. It'll be demonstrated that the predicted Thomson scattering spectra are greatly altered compared to the uniform case, and may even lead to violations of detailed balance. As was mentioned in chapter 1, this implies that the system is in non-equilibrium. Therefore, careful interpretation of the spectra is necessary for spatially or temporally inhomogeneous systems to avoid errors in measured parameters.

Fourth generation light sources hold the promise of improving our understanding of extreme states of matter by providing a probe which can penetrate through the enormous densities produced in inertial confinement fusion or laboratory astrophysics experiments. Thomson scattering by free electrons has emerged as a powerful diagnostic for such systems, through its extension from the optical through the x-ray regime, allowing it to take full advantage of the new capabilities provided by fourth generation light sources (e.g. LCLS, SACLA, European XFEL, SwissFEL) (16, 77, 78). Thomson scattering allows for the measurement of density, temperature, and ionization state in plasmas, leading to an effective characterization of the plasma equilibrium state (16, 79, 80), and progress in the understanding of the properties of high-energy-density matter has significantly relied upon this technique (81, 82, 83, 84, 85, 86, 87). Thomson scattering has also been utilized for probing temperatures and magnetic fields in tokamaks (88, 89).

To date, investigations using Thomson scattering have been based on the assumption of a homogenous or weakly inhomogeneous plasma. This limitation becomes particularly restrictive when considering the ultra-short x-ray pulses and near diffraction limited laser spot sizes of fourth generation light sources (90, 91). Under such conditions, large spatial and temporal gradients in the properties of matter are not negligible and are mainly determined by the extent of laser focus (6). This situation is exemplified by inertial fusion experiments, where the capsule is compressed by a series of shocks (80, 92), which introduce inhomogeneities on the scale of the particle mean free path (*i.e.*, the shock width) and this significantly complicates the determination of the properties of the dense, compressed core in a scattering experiment (93). Interpreting the scattering signals with models developed for homogenous equilibrium systems may thus lead to significant errors in the inferred properties of the matter.

Here we develop a generalization of the theory for Thomson scattering to spatially inhomogeneous systems, with a scale-length of the gradient comparable to the scattering wavelength, as well as to rapidly varying plasma conditions. In order to capture the fast externally driven relaxation processes in a sample, ultrashort pulses with durations on the order of the inverse of the plasma frequency are needed. It will be shown that, under these conditions, both strong density and temporal gradients result in significant changes in the predicted spectra, modifying the intensity and width of the inelastic scattering peaks due to collective electron excitations (plasmons). As Thomson scattering diagnostics yield results by matching theoretical predictions with experimental data, these modifications have important consequences when interpreting experimental data.

3.2 Limitations of theories for homogeneous systems

Consider a scattering probe of wavelength λ_0. The wavenumber of the transferred momentum is determined by the scattering geometry as $k \equiv |\mathbf{k}| \approx (4\pi/\lambda_0)\sin(\theta/2)$, where θ is the scattering angle. The spatial scale-length sampled by the scattering probe is thus $\lambda_p \sim 1/k$. The scale length of microscopic density fluctuations in equilibrium plasmas is determined by the screening length λ_{scr} of electric fields (16, 79). This length is usually taken to be the Debye length in a classical plasma or the Thomas-Fermi screening length in a degenerate electron gas. Whether the single particle behaviour or collective excitations are probed (noncollective versus collective scattering) depends on the ratio of these scale lengths. Thus, the scattering condition is usually cast by the parameter $\alpha = \lambda_p/\lambda_{scr}$.

Noncollective scattering corresponds to $\alpha \ll 1$. In this case, the total scattering signal is the incoherent sum of individual scatterers. Even in an inhomogeneous system, different regions in the plasma will scatter an amount of photons proportional to the local conditions, and the resultant spectrum is expected to be the sum of these local contributions. In the opposite case of collective scattering with $\alpha > 1$, the picture is qualitatively different: now the spatial arrangements of free charges within a distance λ_p give rise to a coherent superposition of scattering waves. Since plasmas support electrostatic waves (plasmons), the scattered photons gain or lose an amount of energy close to $\hbar\omega_{pe}$, where ω_{pe} is the plasma frequency (80). Plasmon resonances appear in the scattering spectrum as a result of these wave-particle interactions.

Thomson scattering probes the fluctuations of a system. In equilibrium systems, these can be either microscopic density perturbations due to bound electrons or screening clouds, or collective excitations such as plasmons. Likewise, hydrodynamic gradients in the plasma conditions may also result in light scattering if they occur on the scale of the probe volume. Moreover, the dispersion of the plasma waves may be affected by gradients. If the scale length of macroscopic spatial inhomogeneities, Λ, is much larger than the length scale probed, that is λ_p, we can still apply the equilibrium theory locally, *i.e.*, on scales $\sim\lambda_p$. Hence, the resultant spectrum is simply the sum of the weighted contributions of different regions in the plasma. For strong gradients with $\Lambda \lesssim \lambda_p$, the plasmon dispersion is changed and, thus, the coherence relation between scatterers is altered. Consequently, macroscopic spatial gradients must be considered in the theoretical description explicitly (see also Ref. (94) for further considerations). Similar difficulties arise if the duration of the scattering probe, τ, is shorter than the time required for screening to be established and the system is dynamically evolving in states far from equilibrium. The typical time scale for such processes is on the order of $2\pi/\omega_{pe}$.

3.3 Theory for inhomogeneous systems

The differential cross section of Thomson scattering is determined by the dynamic structure factor $S(\mathbf{k},\omega)$, where $\hbar\mathbf{k}$ is the change in photon momentum and $\hbar\omega$ is the energy gain (or loss) of the photon during scattering (80). In an isotropic medium all directions are equivalent and the dependence on the modulus of the wavenumber is sufficient, that is $S(k,\omega)$. The structure factor is the Fourier transform of the electron density-density correlation function (13, 95), and essentially an extension of the well-known form factor used in x-ray crystallography (96). Thus, it contains all electron correlations and their dynamics including collective excitations in the system. A number of different sources may contribute to the total dynamic structure factor and thus to the Thomson scattering signal. The total dynamic structure factor, as described in chapter 2, is usually written as (97):

$$S\left(k,\omega\right) = \left|f_I(k) + q(k)\right|^2 S_{ii}\left(k,\omega\right) + Z_f S^0_{ee}(k,\omega) + Z_c \int \tilde{S}_{ce}\left(k,\omega-\omega'\right) S_s(k,\omega') d\omega' \,. \tag{3.1}$$

Briefly reviewing what these terms mean; the first term deals with electrons which follow the motion of the ions. These motions are described by the ion-ion density correlation function $S_{ii}(k,\omega)$, with $f_I(k)$ the scattering form factor of the bound electrons in the ion and $q(k)$ the contribution arising from the screening cloud around an ion. The second term in Eq. (3.1) represents free electrons, those which do not follow the ion motions. The last term consists of inelastic scattering by core electrons, where $\tilde{S}_{ce}\left(k,\omega\right)$ is the structure factor of the core electrons inside an ion and $S_s(k,\omega)$ the self structure of the ions, which describes their thermal motion. Here, Z_f and Z_c are the number of free electrons and core electrons per ion, respectively.

In principle, gradient correction will affect all three terms in Eq. (3.1). However, we expect the largest modifications to occur for the free electron feature, i.e., $S^0_{ee}(k,\omega)$ as the other terms are strongly related to the microscopic bound states that will be unchanged by the gradients in the plasma environment. We will focus on the free electron feature, keeping in mind that corrections in the electron feature should also appear in the ion feature through the screening function $q(k)$. The effect of the screening clouds on the ion feature is strongly dependent on ionization, so we expect that for low Z materials the screening cloud will play a significant role, increasing the likelihood of seeing effects from hydrodynamic gradients in the ion feature. Let's continue with our examination of the effect of collective electron excitations and their dispersion due to gradients in the plasma.

Spatial gradients and fast relaxation processes, including the build-up of correlations and screening, can be described on the basis of the Kadanoff-Baym equations (98). Although numerical solutions are feasible (99), they are restricted for easy situations and simple approximations for the interactions. However, a more practical way is possible for weakly coupled plasmas of interest. Taking

$S(k,\omega) \equiv S^0_{ee}(k,\omega)$, the approximate dynamic structure factor of free electrons in a weakly coupled plasmas is given by the dielectric superposition principle (13)

$$S(\mathbf{k},\omega) = \frac{S^{\mathrm{id}}(\mathbf{k},\omega)}{|\epsilon\left(\mathbf{k},\omega\right)|^2}\,, \tag{3.2}$$

where $S^{\mathrm{id}}(\mathbf{k},\omega)$ is the dynamic structure factor for an ideal (noninteracting) gas, and $\epsilon(\mathbf{k},\omega)$ is the dielectric (screening) function in the random phase approximation (RPA). The latter is given by $\epsilon\left(\mathbf{k},\omega\right) = 1 + \chi^0\left(\mathbf{k},\omega\right)$, where $\chi^0\left(\mathbf{k},\omega\right)$ is the susceptibility of the ideal Coulomb plasma. Eq. (3.2) is an approximation in first order with respect to the correlation strength in the plasma. Although strong coupling effects may need to be taken into account under certain conditions, in most situations concerning laboratory experiments the electrons are nearly or fully degenerate and therefore weakly coupled. The applicability of RPA to first order is often justified for relatively uniform systems, and higher order corrections to the RPA are typically small. Static and dynamic local field corrections act to slightly modify the dispersion relation (i.e., the position of the plasma wave resonance peaks of the structure factor) and can in principle be accounted for within the same theoretical scheme discussed in this paper. Eq. (3.2) also returns to the familiar fluctuation-dissipation theorem (FDT) for systems in local thermodynamic equilibrium (LTE) (13). For systems which are not in LTE different approaches may be considered for the structure factors (100, 101); however, in the context of random phase approximation, the dielectric superposition principle is exact, and we may proceed with a description of the dielectric function for systems considerably departing from homogeneity and equilibrium.

The direct application of Eq. (3.2) is crucial for systems with spatial and temporal gradients as the usual application of the FDT limits the theory to the LTE regime. To extend the applicability of the theory to inhomogeneous plasmas, we follow the approach given by Belyi (102) and Bornatici and Kravtsov (103). Assuming the susceptibility to be a smooth function of macroscopic space ($\mathbf{r}$) and time (t) coordinates, one may apply a first order gradient expansion in the microscopic variables

$$\chi\left(\mathbf{k},\omega\right) \approx \chi^{\mathrm{eq}}\left(\mathbf{k},\omega\right) - i\frac{\partial}{\partial\mathbf{k}}\cdot\frac{\partial}{\partial\mathbf{r}}\chi^{\mathrm{eq}}\left(\mathbf{k},\omega\right) + i\frac{\partial}{\partial\omega}\frac{\partial}{\partial t}\chi^{\mathrm{eq}}\left(\mathbf{k},\omega\right)\,. \tag{3.3}$$

Here, the index ‘eq’ labels the susceptibility for homogeneous systems in thermodynamic equilibrium.

Introducing a scale for the gradients in space and time, the above form can further be simplified: $\partial/\partial\mathbf{r} \approx 1/\Lambda$ and $\partial/\partial t \approx 1/\tau$. Here, Λ represents the spatial gradient along the direction of the scattering wavenumber $\mathbf{k}$ where the sign indicates increasing or decreasing plasma parameters. Unless the spatial gradients are distributed uniformly along all directions, as for example in isotropic turbulence, the scattering spectrum will depend on the specific geometry. Similarly, the time constant τ gives either the strength of externally driven changes (*e.g.*, heating) or the relaxation time within the electron system.

The dielectric response of the system can then be constructed in the usual way

$$\epsilon(\mathbf{k},\omega) \approx 1 + \chi^{\mathrm{eq}}(\mathbf{k},\omega) - i\frac{1}{\Lambda}\frac{\partial}{\partial k}\chi^{\mathrm{eq}}(\mathbf{k},\omega) + i\frac{1}{\tau}\frac{\partial}{\partial\omega}\chi^{\mathrm{eq}}(\mathbf{k},\omega)\ . \tag{3.4}$$

For noncollective scattering, $\chi(\mathbf{k},\omega) \ll 1$, gradients have no significant effect on the dielectric response. On the other hand, in collective scattering the susceptibility cannot be neglected, and $\epsilon(\mathbf{k},\omega) \sim \epsilon^{\mathrm{eq}}(\mathbf{k},\omega)$ follows only if $k\Lambda \sim \Lambda/\lambda_p \gg 1$ and $\omega\tau \sim \tau/\tau_p \gg 1$, as discussed before.

The above expansion can be understood from the constitutive relation between the displacement, $\mathbf{D}$, and the electric $\mathbf{E}$, fields in a macroscopic medium (103):

$$D_i(\mathbf{r},t) = \int d^3r' \int_{-\infty}^{t} dt' \epsilon_{ij}(\mathbf{r},t;\mathbf{r}',t')E_j(\mathbf{r}',t'), \tag{3.5}$$

where $\mathbf{r}$ and t are the space and time coordinates, respectively. This implies that the dielectric tensor is not a function only of $\mathbf{r}-\mathbf{r}'$ and $t-t'$, as we would have in a uniform and stationary medium, but instead it is a function of the space and time variables $(\mathbf{r},t)$ and $(\mathbf{r}',t')$ independently. Through a change of variables the dielectric function may be expressed as

$$\epsilon_{ij}(\mathbf{r},t;\mathbf{r}',t') \to \epsilon_{ij}\left(\mathbf{r}-\mathbf{r}',t-t';\mu\mathbf{r}',\mu t'\right), \tag{3.6}$$

where the ”fast” variables $\Delta\mathbf{r} = \mathbf{r}-\mathbf{r}'$ and $\Delta t = t - t'$ are associated with the microscopic spatial ($\mathbf{k}$) and temporal (ω) dispersion in Fourier space. The remaining ”slow” variables, $\mu\mathbf{r}$ and μt, account for the macroscopic inhomogeneities of the medium. The factor $\mu \approx \Lambda/\lambda_p\,;\, \tau/\tau_p$ compares the scales of the fast and slow variables. When $\mu \gtrsim 1$, the dielectric function is expanded in Taylor series with respect to μ:

$$\epsilon_{ij}(\mathbf{r}, t; \mathbf{r}', t') \approx \epsilon_{ij} + \mu\Delta\mathbf{r} \cdot \frac{\partial \epsilon_{ij}}{\partial \mu \mathbf{r}} + \mu\Delta t \frac{\partial \epsilon_{ij}}{\partial \mu t}, \tag{3.7}$$

and assuming that the electric field is locally of an eikonal form, $\exp[i\,(\mathbf{k}\cdot\Delta\mathbf{r} - \omega\Delta t)]$, Eq. (3.4) is then retrieved (102, 103). From the given dielectric function, the free electron dynamic structure factor of inhomogeneous plasmas can be obtained from Eq. (3.2). As the ideal part is, of course, unchanged, the contribution of gradients to the Thomson scattering signal are all contained in the expression for the dielectric constant Eq. (3.4). Higher-order terms in the Taylor expansion are neglected. Accordingly, this theory presents the first-order correction to the equilibrium treatment and is thus limited to moderate gradients. Of course, in real experiments this condition may not apply and higher-order terms should be considered as they may yield details of the complex relation between the the electric and density fluctuations implicit in the non-local Poisson equation. In the latter case, our theory will give at least a clear signal that an equilibrium treatment is not applicable. It will also give a sense for how higher-order terms may affect the spectrum since the principle effect on the spectrum comes from introducing the real component of the dielectric susceptibility through dispersion. This effect will be seen in all of the odd-order expansion terms, while spectral features akin to equilibrium will be seen in even-order expansion terms. It should be noted here that the above result has been derived upon the assumption of geometric optics, thus this method of addressing inhomogeneities is applicable not just to the free electron dynamic structure factor, but any calculation of the dynamic structure factor which utilizes the dielectric susceptibility. This fact is indeed important if we intend to apply the same analysis to the other terms in Eq. (3.1). The main difference in implementing this formula for terms other than the free electron dynamic structure factor, will arise from whether or not Eq. (3.2) is applicable.

3.4 Application of the theory

In order to evaluate the effects of spatial and temporal density variations in the scattering spectrum, we consider a practical example of a fully ionized dense deuterium plasma with an average electron density $n_e = 2.2 \times 10^{23}\,\mathrm{cm}^{-3}$ and an electron temperature $T_e = 8\,\mathrm{eV}$ (see, *e.g.*, Regan *et al.* (93) for the experimental setup). Under such conditions the Fermi energy is comparable to the thermal energy and thus we need to take into account quantum effects by choosing a suitable form for $\chi(\mathbf{k}, \omega)$. For the present example we use the random phase approximation (57, 81):

$$\epsilon(\mathbf{k}, \omega) = 1 - \frac{e^2}{\hbar \epsilon_0 k^2} \int \frac{f(\boldsymbol{p} + \hbar \boldsymbol{k}/2) - f(\boldsymbol{p} - \hbar \boldsymbol{k}/2)}{\boldsymbol{k} \cdot \boldsymbol{p}/m_e - \omega - i v} \frac{2 d^3 p}{(2\pi\hbar)^3} \tag{3.8}$$

where $f(\boldsymbol{p})$ is the electron distribution function.

This plasma is probed with x-rays with an energy of 2,960 eV at a scattering angle of $\theta = 40^{\mathrm{o}}$, giving $\alpha = 2.17$, i.e., collective scattering conditions. The characteristic probe scale length is $\lambda_p \approx 0.1$ nm, and the relaxation time is $\tau \approx 0.2$ fs. This suggests that strong spatial gradients may be observable whereas it will be improbable to find suitable ultra-fast probes.

In Figure 3.1a, we have plotted the dynamic structure factor $S(\mathbf{k}, \omega)$, giving the form of the expected Thomson scattering signal for different values for the spatial scale Λ (and taking $\tau \to \infty$). We observe large changes in both the width and relative heights of the blue and red shifted plasmon resonances when $\Lambda/\lambda_p \lesssim 10$. Moreover, the relative intensity of the two resonances changes depending on the direction of the gradients with respect to the probe (parallel or anti-parallel). In Figure 3.1c, we have considered the case of temporal fluctuations comparable to the probe duration (and with no spatial gradients). Again, the predicted dynamic structure factor is significantly broadened for $\tau/\tau_p \lesssim 2$. This effect is to be expected, since a shorter pulse duration would have the same effect as a higher collision frequency between scatterers, which results in a broadening of the plasmon lines.

As expected, the detailed balance relation is not recovered for nonhomogeneous and nonequilibrium systems. In a homogeneous plasma, the intensity of the plasmon resonances is determined by detailed balance (13, 104). Detailed

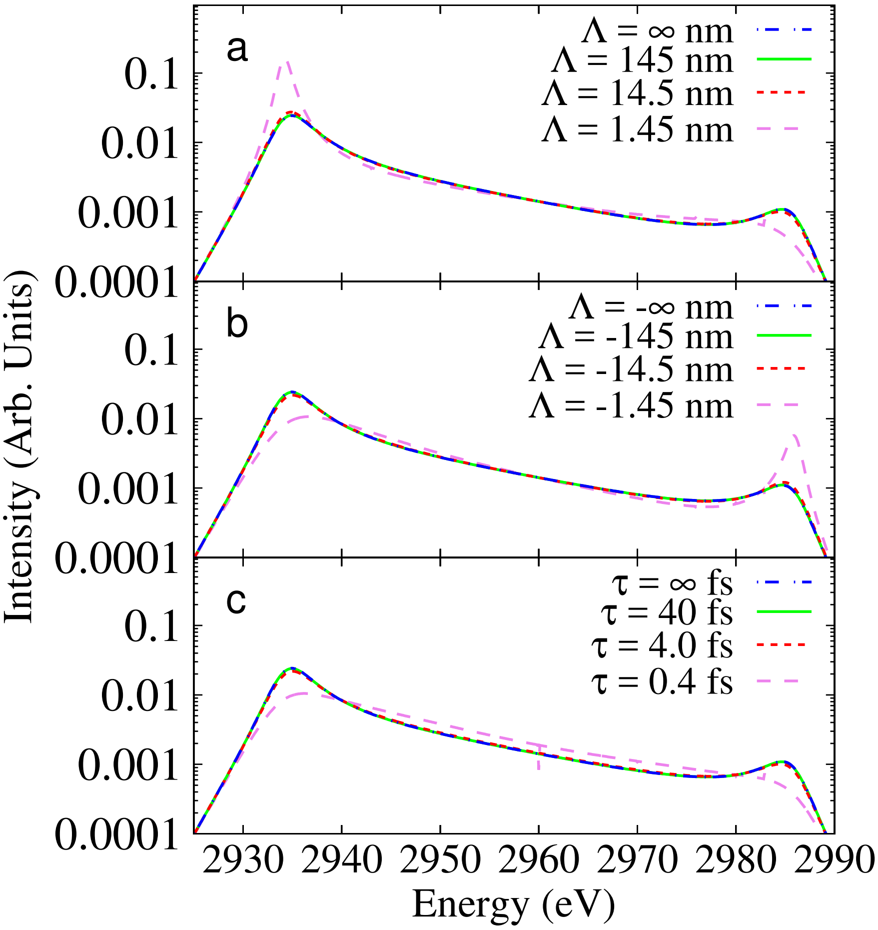

Figure 3.1: Effects of gradients in the intensity of the plasmon resonances. a) Calculation of Thomson scattering intensity, which is proportional to $S(k,\omega)$, with different values of Λ and $\tau = \infty$. The spatial gradients are all assumed to have a component parallel to $\mathbf{k}$ where $k = 1.03 \times 10^{10}$ m^{-1}. b) Same as a) but with the direction of the gradients reversed. c) Calculation of $S(k,\omega)$ with different values of τ and $\Lambda = \infty$.

balance is a consequence of LTE, which, in this case, is governed by Fermi statistics, where scattering events for which the electron final state falls into an energy level lower than the ground state (and consequently an energy gain for the photon) are not allowed. In an inhomogeneous system, however, currents (transport effects) induced by the gradients provide an additional sink or source in the energy exchange between electrons and photons. This effect is also well-known from scattering measurements of ion acoustic waves in classical plasmas in the presence of a heat flow (79).

The change in the detailed balance relation bears important consequences in the analysis of Thomson scattering data from solid density plasmas. As discussed in Refs. (80, 105, 106), the intensity ratio of the two plasmon peaks is often assumed to provide a direct measurement of the temperature, without relying on any additional approximations. On the other hand, as discussed by Chapman and Gericke (107), once the homogeneous plasma or equilibrium assumption is relaxed, the intensity ratio of the plasmon peaks is no longer uniquely defined by the electron temperature. In such cases, nonequilibrium distributions and spatial gradients determine the shape and intensity of the plasmon peaks in the scattering signal.

Figure 3.2 demonstrates how the ratio of the upshifted and downshifted plasmon signals dramatically diverges from the equilibrium case as density varies for the same conditions given in the example above. The ratio of plasmon signals is maximized when $n_e \approx 2.8 \times 10^{23}\,\mathrm{cm}^{-3}$ which occurs when $\mathrm{Re}[\chi^{\mathrm{eq}}(\mathbf{k},\omega)]$ reaches a minimum for both resonances, $\omega = \pm\omega_{pe}$, while $\dfrac{\partial}{\partial k}\mathrm{Im}[\chi^{\mathrm{eq}}(\mathbf{k},\omega)]$ reaches a maximum for the upshifted plasmon and a minimum for the downshifted plasmon. It is due to this latter term being an odd function with respect to ω that the detailed balance condition is violated. We may conclude that given a sufficiently nonequilibrium plasma probed in the collective scattering regime, assuming the ratio of the plasmon peaks to yield a measure of temperature may lead to large errors.

Similarly, in Figure 3.3 we see how significantly the red and blue shifted plasmon peak intensities change as a function of the inhomogeneity scale lengths. The simulations were conducted for the same plasma parameters as discussed above, while varying either Λ or τ. Here we see that the results of the new

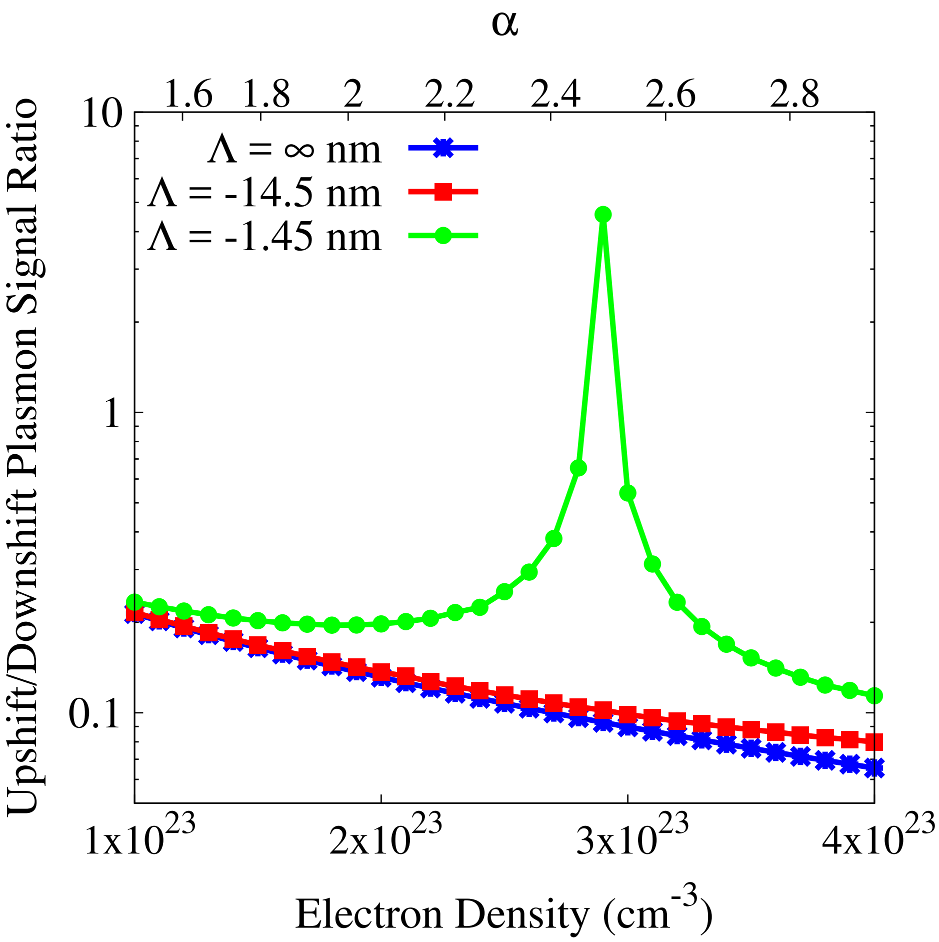

Figure 3.2: Ratio of upshifted over downshifted plasmon signals The ratio of the integrated plasmon signals is given for different gradient conditions as well as the equilibrium case. The intermediate gradient (red) steadily diverges from the equilibrium case (blue) with increasing density. We see two effects for the larger gradient (green). First, the green curve begins to diverge from the equilibrium case at a lower density, as expected. Second, as density increases, the green curve peaks and subsequently decreases rapidly; this is due to the coincidental minimization of $\mathrm{Re}[\chi^{\mathrm{eq}}(\mathbf{k},\omega)]$ which emphasizes the effect of the gradient expansion terms on the DSF.

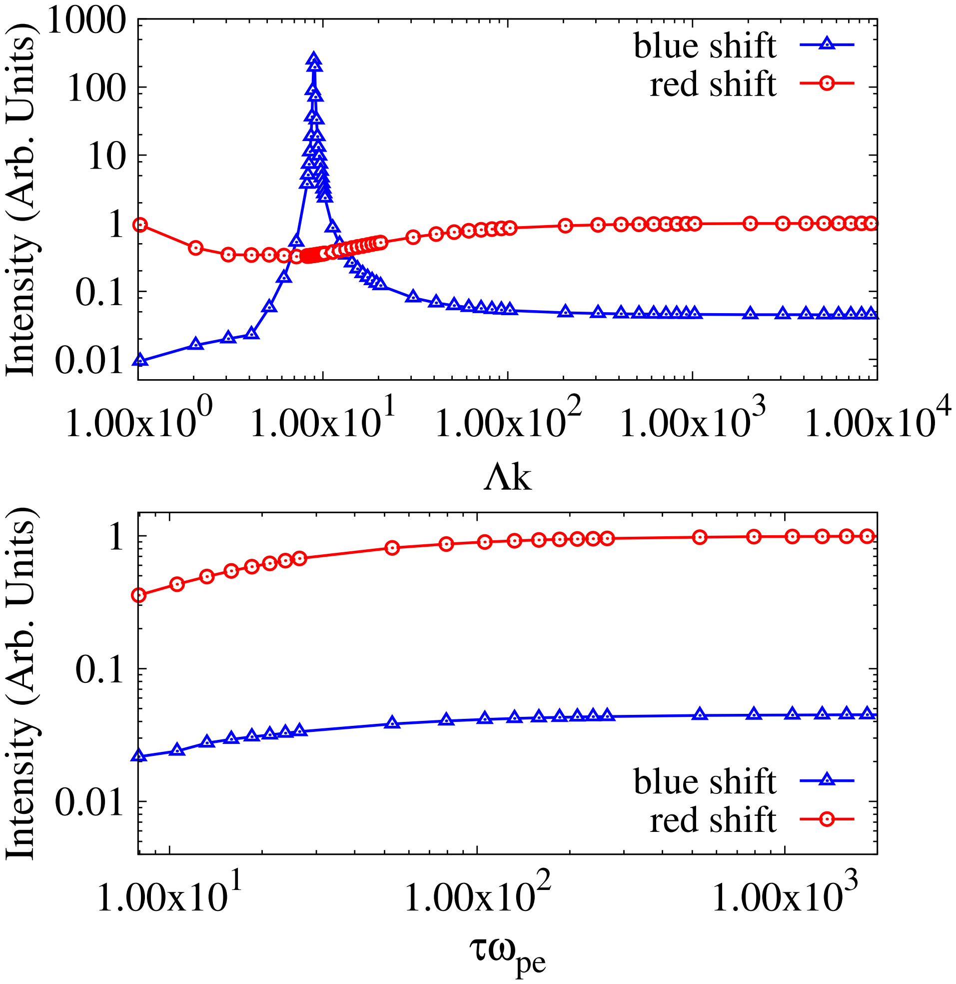

Figure 3.3: Effects of gradients on plasmon peak intensities. We show the variation in the peak intensities of the plasmons with respect to the gradient parameter. For spatial gradients this is Λk and for temporal gradients this is $\tau\omega_{pe}$. For spatial gradients we see a sharp rise in the blue shifted plasmon and a dip in the red shifted plasmon as we approach steeper gradients (*i.e.*, lower gradient parameter). For temporal gradients both plasmons are reduced with higher gradients.

approach deviate from equilibrium starting at around $\Lambda k \sim 100$. It is important to note, that although the figure gives a sense of how gradients may alter the scatter signal, the change is not the same for all plasma parameters. This is due to the inhomogeneous dynamic structure factor depending on differences between the real and imaginary components of the dielectric susceptibility as described above.

3.5 Comparison with summation method

An approximate, but often applied (32, 108, 109, 110, 111), method to account for the effects of spatial gradients on the Thomson scattering spectrum is to simply take the average over a given region. Thus, individual scattering spectra are generated for different plasma regions using the FDT, weighted by the number of electrons present in the subvolume selected and finally added to obtain the full spectrum:

$$S_{\text{sum}}(\mathbf{k},\omega) = \frac{\Sigma_j V_j n_{e,j} S_j(\mathbf{k},\omega)}{\Sigma_j V_j n_{e,j}}, \tag{3.9}$$

where V_j, $n_{e,j}$ and $S_j(\mathbf{k},\omega)$ are the volume, electron density and structure factor of cell j, respectively. The simplest approximation consists in taking $S_j(\mathbf{k},\omega) \equiv S_j^{eq}(\mathbf{k},\omega)$, where $S_j^{eq}(\mathbf{k},\omega)$ is the equilibrium structure factor inside the jth cell. This is the method discussed in Ref. (32, 108, 109), for example. As already mentioned, this incoherent addition of scattering spectra is strictly valid only if $\alpha \ll 1$ or both $\Lambda/\lambda_p \gg 1$ and $\tau/\tau_p \gg 1$. One might assume that dividing the volume into infinitesimally small cells would make this method applicable even for steep gradients, however, one neglects the explicit influence of the gradients in this way. Technically, the problem with the LTE treatment is that the local dynamic structure factors which are being used assume that only the imaginary, dissipative component of the dielectric susceptibility is important, as in Eq. (3.2), but don't consider the current flows. This assumption fails for large gradients where the real component of the dielectric susceptibility becomes critical. Such an effect is also common in Onsager-violating media where cross-terms between the energy storing and dissipative components of the dielectric susceptibility emerge (112).

Here, instead, we may replace the calculation of the equilibrium structure factor inside each subvolume element with its non-equilibrium version.

Let us continue our practical example and test the above approach by assuming that the plasma exhibits density variations on a scale of $\Lambda = 1.45$ nm. The density gradient is then given by $dn_e/dr = n_e/\Lambda$. We notice that such gradients are, for example, quite common in shocked dense matter. For the conditions of Ref. (93), we expect the electron mean free path to be $\lambda_{\mathrm{mfp}} \sim 0.4$ nm, and thus the shock width to be a few mean free paths, which is indeed of the same order as assumed here.

Figure 3.4 shows a comparison between the overall structure factors calculated with the methods described above. Large modifications to the whole spectrum are seen when the full effect of inhomogeneities is accounted for in the weighted sum.

3.6 Concluding Remarks

This work indicates that collective Thomson scattering by free electrons from strongly inhomogeneous matter requires a modeling of the dielectric response including not only the effects of microscopic, but also macroscopic spatial and temporal gradients. The treatment presented here gives results that differ significantly from those assuming uniform plasma conditions for systems with gradients as often encountered in experiments, in particular the violation of detailed balance.

One could expect that with such a large effect on the scattered spectrum that this effect may have been seen before, especially in the experimental conditions used for the prior simulations. Although previous experiments have been conducted on a plasma with similar conditions, those experiments were in the non-collective regime. Figure 3.2 suggests that as the alpha parameter tends towards the non-collective regime, gradient effects on the scatter spectra become negligible. We can show this explicitly by taking a simulation with the exact same parameters but with a scatter angle of $\theta = 90°$ corresponding to $\alpha = 0.8$. Even though $\alpha \sim 1$ we can see how gradient effects are negligible in the non-collective case when compared to homogeneous simulations, as seen in Figure 3.5. This explains why the effects of gradients have not been observed in previous experiments in this campaign. For XRTS experiments outside of this campaign, it could be that the real and imaginary components of the dielectric susceptibility do not reach extrema for the experimental parameters and therefore the effect of gradients would be quite small and easily mistaken as an error in electron temperature.

Further work must be done to incorporate inhomogeneities for Thomson scattering by screening clouds and ion acoustic modes, which are ubiquitous in warm dense matter and tend to be strongly correlated. The extension for screening clouds should be relatively simple as this can be formulated in terms of the free electron structure factor, as shown in chapter 2. In subsequent chapters we will examine the application of the inhomogeneous theory to electron scatter spectra obtained at OMEGA in the collective regime.

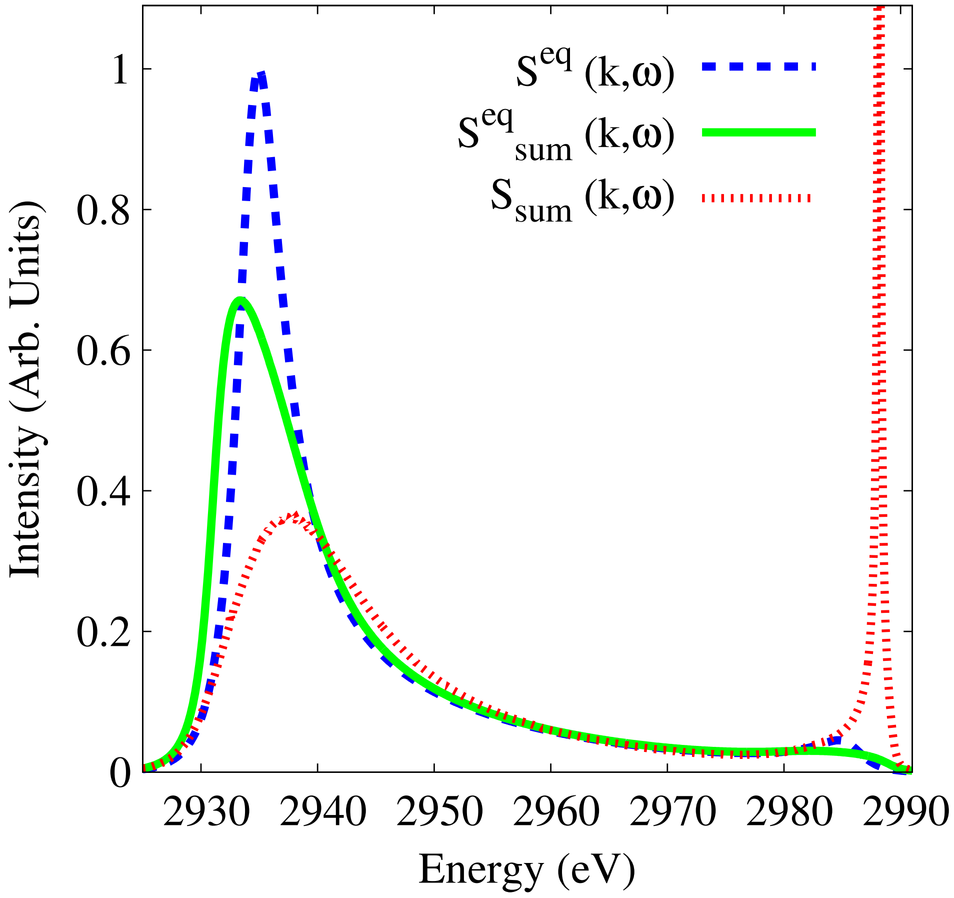

Figure 3.4: Predicted spectra. We have compared the homogeneous case (green line) against our full inhomogeneous scattering model (red line) using the weighted sum method in both cases and for the plasma conditions given in the text with $\Lambda = 1.45$ nm and where $k = 1.03 \times 10^{10}$ m^{-1}. The scatter parameter is $\alpha \sim 1.6$. The weighted sum method was implemented by assuming a linear density profile, with n_e varying from 1.1×10^{23} cm^{-3} to 3.3×10^{23} cm^{-3} over a distance equal to Λ. This profile is then divided into 220 equal cells and the scattering from each cell summed together. The equilibrium structure factor (assuming an homogeneous plasma) is also shown in the figure (blue line). It is clear that the upshifted plasmon peak intensity for the inhomogeneous weighted sum case is much higher than even the downshifted plasmon intensities. This plasmon peaks at an intensity of 3 relative to the rest of the curves (not shown).

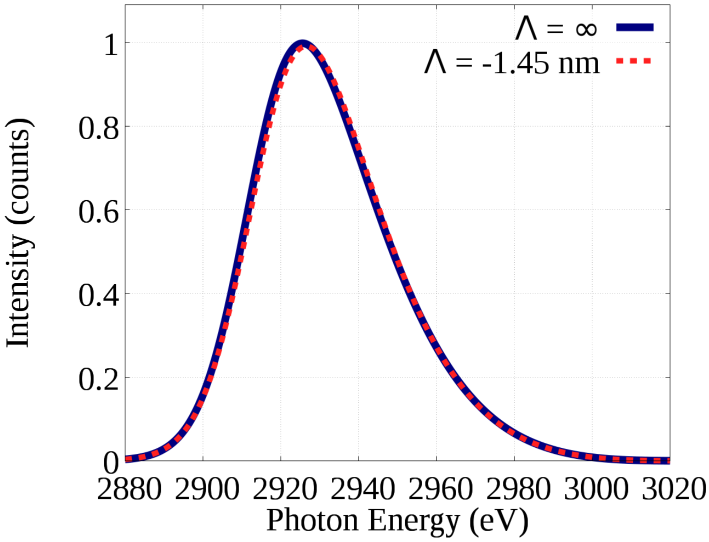

Figure 3.5: *Blue*: Homogeneous inelastic peak for $T_e = 8$eV, $n_e = 2.2\times10^{23}$cm^{-3}, and $Z = 1.0$, for $\theta = 90°$ with $\alpha = 0.8$ and $k = 1.03\times10^{10}\,\mathrm{m}^{-1}$. *Red*: Same plasma parameters as blue, but including the inhomogeneous correction with $\Lambda = 1.45\,\mathrm{nm}$. We see that there is effectively no change in the homogeneous scatter spectra due to gradient effects.

4

OMEGA experimental setup

> *A scientist in his laboratory is not only a technician: he is also a child placed before natural phenomena which impress him like a fairy tale.*
>
> —Marie Skłodowska Curie, *Madame Curie : A Biography (1937)*

4.1 Introduction

Experiments probing warm dense matter using X-ray Thomson scattering were conducted at the OMEGA laser facility in Rochester, New York. This chapter will discuss the details of the experimental setup, centering around the laser configuration, diagnostics, and target configuration. The aim of the experiment is to provide an experimental basis against which equation of state models of warm dense matter may be tested.

The experiment consists of a copper cell filled with deuterium. The copper is cryogenically cooled until the deuterium transitions to liquid phase. One face of the cell is covered by a thin plastic ablator which is driven by a number of laser beams, generating a shock that expands into the deuterium. On the opposite side of this copper cell is a separate foil and channel. The foil is a chlorinated plastic called Parylene-D. Beams ablate the foil generating x-rays which are then collimated through the channel and scatter off of the progressing shock front. The scattered x-rays are collimated down yet another channel which leads to the x-ray spectrometer where the Thomson scattered spectra are recorded. See Figure

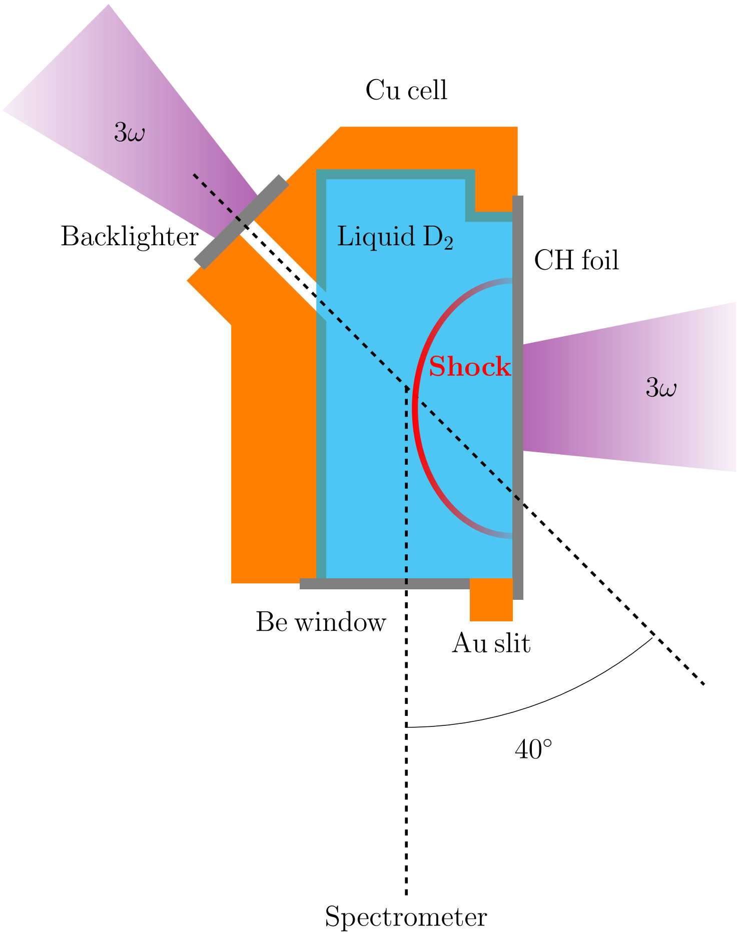

Figure 4.1: Detailed schematic of cryo-XRTS target. A shock is driven into the deuterium filled cryo cell by ablating the polyimide window on the H14 side. Subsequently, a Parylene-D backlighter foil is ablated from the H7 side generating Cl Ly-α emission at 2.96 keV. The x-rays are collimated through a 1.5 mm long pinhole and then scattered off of the oncoming shock. X-rays scatted at an angle of $\theta = 40°$ are collected by the gated Thomson scattering detector.

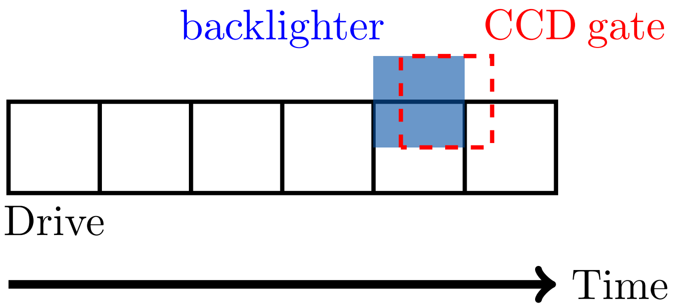

Figure 4.2: Relative timings of drive beams, backlighter beams and detector gate. Each black bin is 1 ns. The drive beam is composed of 12 pairs of beams each on for 1 ns, starting at $t = 0$ ns, to create a longer 6 ns pulse. The Cl Ly-α backlighter (blue) is ablated at $t = 4$ ns and the spectrometer (red) begins acquiring data at $t = 4.3$ ns. The backlighter is on for 1 ns, while each of the 4 strips on the detector is on for 250 ps for a total detection time of 1 ns.

4.1 for a visual representation. The primary diagnostic on this experiment was the gated Thomson spectrometer (GTS). Secondary diagnostics included x-ray pinhole cameras (XRPHC) and an x-ray streak camera for diagnosing the quality of the laser spot size on the Parylene-D backlighter and the temporal evolution of x-rays emitted.

In general, the target and laser configurations were static and decided upon well ahead of the shot day. Laser parameters such as pulse shape, energy, frequency conversion, profile smoothing, timing, pointing, and focusing were submitted via the LLE shot request form (SRF) system. The work of setting up the target alignment, laser parameters, and cryogenic cooling to the requested specifications were carried out by LLE engineers.

4.2 Laser configuration

The OMEGA laser facility consists of 60 beams oriented in a truncated icosahedron (i.e. a soccer ball) which can deposit up to 40 kJ on a target. The ports are labeled based on whether they lie on a pentagon (P), or hexagon (H) of the soccer ball. Of the available beams, 12 beams from the H14 side were used to drive a $8\,\mu$m thick polyimide ablator at $\sim 10^{14}\,\mathrm{W/cm^2}$. The sudden deposition of energy into the ablator causes the material at the laser-target interface to quickly heat up and expand generating a single shock (113). The foil was driven over a spot size of $600-800\,\mu$m for 6 ns by firing pairs of beams for 1 ns each, with a square temporal pulse. The drive beams were in the third harmonic ($3\omega \sim 351\,$nm) with frequency conversion crystal (FCC) detuned from the maximum 500 J to 300 J for first 3 ns of drive and to 420 J for the final 3 ns of the drive. Higher angle beams are detuned because of larger spot size so that a level intensity profile is maintained. Another 13 beams (also 3ω) were employed from the H7 side of the chamber to ablate the Parylene-D backlighter. The backlighter material is essentially chlorinated plastic which, when sufficiently heated, emits Cl Ly-α x-rays corresponding to a photon energy of 2960 eV. The lasers driving the backlighter were tightly focused to a spot size of $\sim 200\,\mu$m to maximize the desired Cl Ly-α emission while suppressing satellites and avoiding ablation of copper which would lead to noise in the form of hard x-rays and background continuum.

4.3 Experimental Diagnostics

4.3.1 Gated Thomson Spectrometer

The gated Thomson spectrometer (GTS) is an X-ray spectrometer consisting of an X-ray framing camera (XRFC) and a Bragg crystal which diffracts the incoming x-rays onto the framing camera. The framing camera is simply a CCD detector combined with a micro-channel plate (MCP). The MCP has four strips each of which were independently and sequentially powered across the entire strip for 0.25 ns such that together they covered the 1 ns duration of the backlighter. A flat highly oriented pyrolytic graphite (HOPG) mosaic crystal was used to spectrally disperse the x-rays as per Bragg's law $n\lambda = 2d\sin\theta_B$ (114, 115). The crystal was set at the Bragg angle of $\theta_B = 38.6°$ with respect to the scattering source and the camera to optimize the intensity for 2960eV x-rays by constructive interference in the cystal lattice, where the interlattice spacing of the HOPG crystal is $2d = 0.6708$ nm. The MCP camera was positioned 23.8 cm from the

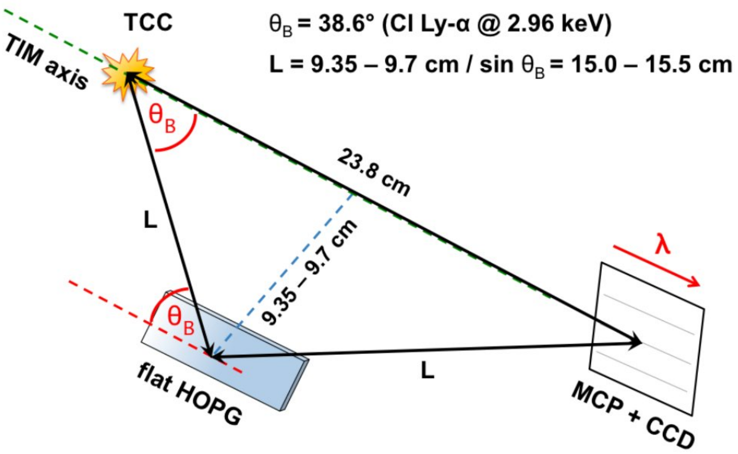

Figure 4.3: Diagram of the gated Thomson spectrometer (GTS) depicting the orientation of the diffracting crystal relative to target chamber center (TCC) and the CCD/MCP detector.

scattering target center, which translates to a spectral resolution of $\sim 12\,\mathrm{eV/mm}$. A Beryllium blast shield was used to filter out visible radiation and prevent debris from damaging the spectrometer.

4.3.1.1 X-ray Framing Camera (XRFC)

LLE has four x-ray framing cameras on offer with time-resolved, two-dimensional, x-ray imaging (116, 117). Two of the cameras have a fixed resolution of ~ 40 ps while the other two have a range of resolutions set by pulse-forming modules with values of 80, 200, 300, 400, 500, or 1000 ps. The cameras are mounted on ten-inch manipulators (TIMs) which allow for positioning within the target chamber. Two cameras were used in this campaign. XRFC4 was coupled with the GTS and mounted on TIM6 (port P7) as the primary Thomson scattering diagnostic. The pulse across each of the 4 strips of XRFC4 was selected to be 250 ps to give some temporal resolution during the 1 ns duration of the backlighter, while not sacrificing signal due to low exposure time. XRFC1 was mounted on TIM1 (port P3) and was focused on the backlighter to examine the temporal evolution of the emission from the ablated backlighter plasma.

An MCP is used to amplify and gate the detected x-ray signal. The MCP is a gold photocathode with a large number of micro-channels which are connected to a high voltage power supply and a phosphor plate (118, 119). When x-rays are incident on the gold cathode they release eletrons. Each of these electrons is accelerated by the electric potential in the MCP. When an accelerated electron collides with the wall of the MCP channel it further releases more electrons creating a cascade that propagates down the length of the channel. The MCP has four strips which can be independently biased by the power supply, allowing for gating and some temporal resolution. When the electrons reach the end of the microchannels they are absorbed by the phosphor plate which forms a 2-D image in the optical range.

Images of the phosphor plates were recorded by a charge-coupled device (CCD) camera. The CCD is a 4096 × 4096 matrix of pixels each of which is 9 μm in size (120). Dark-current noise in the chip is reduced by cooling the cameras to $-20°$ C.

The shots on OMEGA pack so much energy into the shot that by the end the target is completely obliterated and the debris has been launched in all directions throughout the target chamber. An 8 mil (~ 200 μm) Be blast shield was used to shield the GTS from incoming debris, which proved to be critical. In addition to debris, the target generates a lot of unwanted radiation which we shield with a 5 mil (~ 125 μm) Be filter for XRFC4 inside of TIM 6. For CRYO shots the bias voltage on the MCP was set anywhere from 100 V to 300 V. This positive bias further attenuates the measured signal by $\sim 3\times$ for every 50 V. Each strip was gated to measure for 250 ps and they were set sequentially to yield 1 ns of measurements covering the time which the backlighter is driven to produce x-rays.

4.3.1.2 Mosaic Crystal

When one thinks of Bragg diffraction, perfect or single crystals come to mind. These are crystals where all the atomic planes are uniformly arranged to be parallel to each other, where their normal vector defines the surface of the crystal. Single crystals provide the highest spectral resolution, but at the cost of low reflectivity since x-rays are constrained to reflect from specific points on the lattice. In x-ray Thomson scattering, the scattered signal is generally very low and using

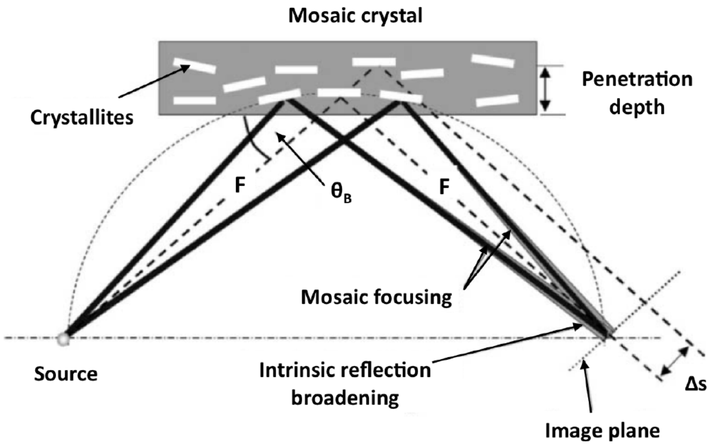

Figure 4.4: Generalized schematic of a mosaic crystal showing how crystallites are misaligned with respect to the face of the crystal. Mosaic focusing occurs if the distances, F, between the image plane and the crystal and the source and the crystal, are equal. X-ray penetration into deeper layers of the crystal can cause a smearing of Δs in the image plane, as can a finite source size.

a single crystal would only worsen the situation. Therefore, we use *mosaic* crystals which sacrifice spectral resolution for higher reflectivity. Mosaic crystals are composed of small sections of perfect crystal lattices all of which are partially and randomly misaligned with respect to the crystal surface, as illustrated in Figure 4.4 (114).

The misalignment of these crystal units causes the x-rays to reflect in a wider randomized spread about the Bragg angle. This *mosaic spread* means that while more x-rays may be accepted from different angles, increasing reflectivity, the reflected beam is defocused perpendicular to the diffraction plane. X-rays of the same energy may arrive along slightly different sections along the spectral axis and x-rays of slightly different energy may arrive at the same point, which translates to a reduction of spectral resolution. If the spread of random crystal orientations can be described by a Guassian distribution function then the *mosaicity* is simply the FWHM of the distribution. Such a simple model may not always be applicable and studies have shown richer complexity in crystal structures (121, 122).

Although mosaic crystals cause loss of spectral resolution through mosaic spread they may also counteract this through *para focusing*. Given a Roland's circle of some fixed radius and a curved crystal on the circle, the crystal will focus rays originating from a point source located anywhere on the circle. For a mosaic crystal, a fraction, of the diffracted x-rays will always fall on Rowland's circle and thus be focused onto the detector (114). This can reduce source broadening and increase spectral resolution.

HOPG crystals are separated into the categories ZYA, ZYB, ZYD, and ZYH which correspond to mosaicity ranging between 0.4° and 3.5°. To select a reasonable crystal for XRTS we must be able to resolve the Compton shifted plasmon peak at $\sim 17.4\,\mathrm{eV}$ away from the quasi-Rayleigh peak, which corresponds to a required resolution of $(\Delta E/E) \sim 5.9 \times 10^{-3}$. This immediately discounts the ZYH crystal which has $(\Delta E/E)_{gamma} \sim 38.1 \times 10^{-3}$, causing excessive mosaic broadening to smear the elastic and inelastic features together. Another mechanism which must be taken into account is depth broadening, where the x-rays penetrate and reflect off of lattice sites deep in the crystal. The penetration depth for 3 keV x-rays is $\lambda \sim 30\,\mu\mathrm{m}$ which corresponds to a depth broadening of $(\Delta E/E)_{depth} = \frac{\lambda_{mfp}}{2L} \times \cos^2(\theta_B) \sim 6.0 \times 10^{-5}$ where L is the distance between the crystal and the detector. The penetration depth and corresponding broadening are negligible so the crystal can essentially be of any thickness (123). The integrated reflectivity for the ZYA HOPG crystal for x-rays at 2960 eV is expected to be $\gamma r_p \sim 3\,\mathrm{mrad}$, where r_p is the peak crystal reflectivity (123).

Previous experiments carried out by Dr Katerina Falk and Dr. Sean Regan initially used the ZYA crystal. This gave a high resolution, but low signal so they switched to the ZYB crystal (30). For this experimental campaign, we used a crystal of ZYA type with dimensions 25×50 mm and 2 mm thick with $\gamma = 0.4^\circ \pm 0.1^\circ$ with the expectation that the inelastic peak in the collective regime will be narrower than that of the non-collective regime making it more difficult to extract the signal if the elastic and inelastic peaks overlap due to resolution limited broadening. Another significant source of broadening will be the finite size of the backlighter which is somewhat restricted by the collimator (124). The ray divergences for the three different Ta pinhole sizes, all of depth 1.5 mm, are 7.6°, 15.2°, 22.6°, for $200\,\mu$m, $400\,\mu$m and $600\,\mu$m respectively. Of course, it should be stated that these broadening effects will largely be accounted

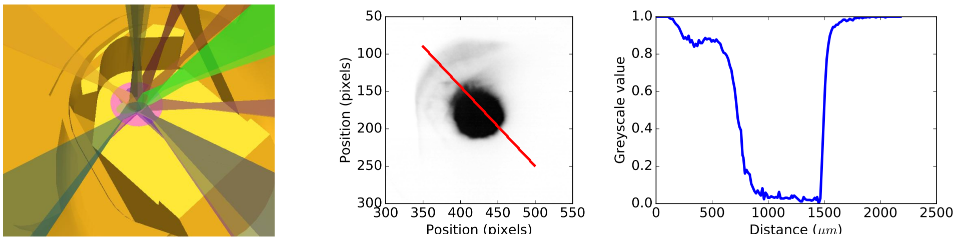

Figure 4.5: *Left*: View from P2C x-ray pinhole camera generated in VisRad. *Middle*: Image from XRPHC showing a uniform spot with no star-like features. The red line represents the lineout taken to assess the spot size. *Right*: Corresponding lineout showing the spot to be $\sim 800\ \mu$m in diameter.

for by the instrument function acquired on spectral calibration shots, provided that the elastic and inelastic peaks are indeed distinct and resolvable.

4.3.2 X-ray pinhole cameras

A number of x-ray pinhole cameras are located in various static positions throughout the OMEGA chamber. These are time-integrated diagnostics which we used to view the high intensity radiation emitted from the backlighter foils. An additional XRPHC was mounted on port P2 to get a good view of the backlighter. This XRPHC was positioned at $\theta = 68.43°$, $\phi = 54.0°$ with respect to the top of the target chamber. The pinholes are made of 50 μm thick Ta with a laser drilled hole of diameter 10 μm. The distance from the pinhole on port P2 to the target is 162.5 mm and the distance from the pinhole to the imaging plane is 648 mm yielding an image magnification of $\sim 4\times$ and an on target resolution of 10 μm/pixel. The images are recorded using charge-injection devices (CID) in direct-detection mode, meaning without phosphor. The CID chips have an effective resolution of 800×600 pixels with a pixel spacing of 38.5 μm (125). The CIDs have a sensitivity range of about $2 - 8$ keV and are typically covered with a 152.4 μm Be window (4 mils of blast shield, 1 mil vacuum window, and 1 mil camera window).

An image from the P2 pinhole camera is shown in Figure 4.5. Broadening of the spot is expected due to expansion of the plasma away from the foil, meaning that the true spot size should be smaller than that seen by the XRPHCs. The images are generally saturated in the center of the spot, but this is unimportant as we are using the XRPHCs to verify the shape and alignment of the spot. If the laser is misaligned the surrounding copper will be ablated and the spot will appear star-shaped.

4.3.3 X-ray Streak Camera

The temporal evolution of x-ray spectra emitted from the Parylene-D backlighter was measured with an x-ray streak camera (SIM Streak Camera A, SSCA) mounted on TIM2 (126). The camera is cross-timed to within ±25 ps of the laser pulse trigger using a fourth-harmonic timing fiducial channel which is recorded along with the streaked x-rays. The SSCA was protected with a 4 mil ($\sim 100\,\mu$m) Be blast shield and filtered with an additional 0.5 mil ($\sim 12\,\mu$m) of Al.

The streak camera functions by converting incident x-rays into electrons using an Au cathode on a 0.5 mil ($\sim 12\mu$m) Be substrate. The electrons are accelerated to 13 keV through an accelerating mesh. They are then deflected by charged parallel plates. The plates are connected to fast power supply which rapidly sweeps the voltage on the plates causing passing electrons to increasingly deflect over time, yielding temporal resolution based on the sweep time. The deflected electrons then impact a phosphor screen the emission of which is recorded on film. For our setup the sweep velocity was 115 ps/mm across a 40 mm phosphor screen, yielding a temporal window of $\sim$ 4 ns. The temporal window was centered at $t = 5$ ns giving a full temporal picture of the backlighter evolution. The film used to record the streaked spectra was Kodak T-max 3200 film. This was developed via rotary processing and digitized with a Perkin-Elmer PDS (photometric data system) Microdensitometer with a resolution of 50 μm/pixel. This can be used to obtain absolute intensity through the use of a calibrated white lamp scanner fitted with adjustable ND filters and a photomultiplier tube (30).

The spectrometer used a flat rubidium acid phthalate (RbAp) crystal ($2d =$ 2.6121 nm) mounted with a Bragg angle of $\theta_B = 8.7°$. The central wavelength was 3.96Å (3.14 keV) with a range of $3.19 - 4.67$Å ($2.66 - 3.89$ keV) so that various Cl K-shell lines could be resolved, including: Cl He-α at 4.444Å, Cl H-α at 4.188Å, Cl He-β at 3.790Å, Cl He-γ at 3.603Å, Cl H-β at 3.535Å, and Cl H-γ at 3.351Å. The crystal was placed between the source and the slit of the streak camera at a distance of 19” (~ 48.26 cm). It should be noted that the SSCA cannot give a direct measure of temporal profile of the backlighter as seen by the shock because of variable filtering effect of the Parylene-D foil/plasma between the ablated side of the foil and the backlighter aperture.

4.4 X-ray Backlighter

4.4.1 Spectral Profiles

The x-ray probe used in this campaign was a Cl Ly-α line at 2.96 keV ($\lambda_0 = 4.188$Å). The x-rays were generated by laser ablating a 10 μm thick Parylene-D foil. The foil was irradiated with 13 beams for the duration of 1 ns at 10^{15} W/cm^2 (200 μm focal spot, 500 J/beam). The lasers were set at 3ω to optimize the x-ray conversion efficiency and reduce backscattering instabilities (15). The small cross-section of the Thomson scattering process yields a small signal, therefore the Cl Ly-α line was chosen due to its high conversion efficiency ($\eta_x \sim 0.2\%$) and narrow bandwidth ($\Delta E/E \sim 2 \times 10^{-3}$) with the aim of producing enough x-rays to observe a signal above the noise of background continuum spectra (3, 127, 128).

Ly-α radiation is a consequence of transitions from $n = 2$ to $n = 1$ atomic energy levels. In the case of Cl Ly-α the Cl is in such a highly ionized state, from heating of the plasma via inverse Bremsstrahlung, that it is hydrogen-like and emits Lyman series x-rays from electrons dropping into the K-shell. The line consists of two fine structure components Cl Ly-$\alpha_{1,2}$ at 2958 eV ($1s - 2p_{1/2}$) and 2962 eV ($1s - 2p_{3/2}$). The total width of the line is $\sim$ 9 eV (127). The line has relatively strong dielectronic satellites on the lower energy wing, which include Cl XVI ($2p^2 - 1s2p$) at 2928 eV and 2933 eV as seen in Figure 4.7. The laser parameters were selected to limit relative strength of these satellites in comparison to the resonance line.

Prior experiments by Dr. Katerina Falk sought to minimize the x-ray contribution from satellites as these would hamper the resolution of the downshifted Compton feature in the Thomson scattered spectra (30). Phase plates were used

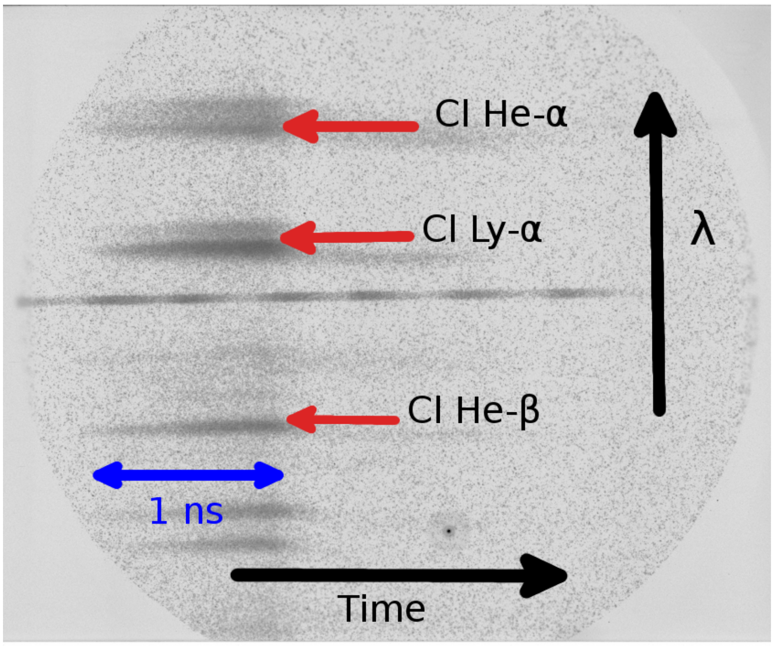

Figure 4.6: X-ray streak camera (SSCA) data taken during a Cryo-XRTS shot in April 2013. The Cl Lyman-α line at 2.96 keV is strong throughout the 1 ns drive of the Parylene-D foil. Weaker, satellite lines such as Cl He-α and Cl He-β are also seen. Towards the center of the image, there is a periodic structure which is the timing fiducial consisting of 8 pulses each 548 ps apart (129).

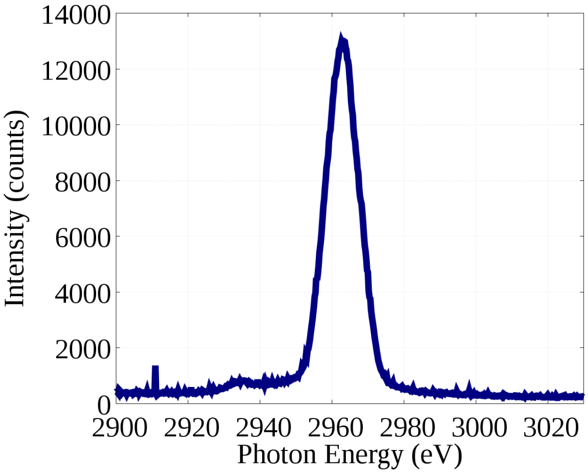

Figure 4.7: Spatially-integrated lineout from GTS during spectral calibration shot. The Cl Lyman-α peak of the backlighter is nearly at 2.96 keV; needing an offset of $\sim$ 2 eV to compensate for differences between the theoretical dispersion curve and alignment of the diagnostic. A relatively weak Cl XVI satellite is seen near 2933 eV

to dampen backscattering instabilities thereby increasing conversion efficiency. They found that increasing the intensity by narrowing the spot size led to a reduction in Li-like satellites and that higher electron temperatures and ionization dampened the He-like emission (15, 127). At later times the plasma cools causing the satellite emission to emerge as seen from the SSCA. This makes gating of the GTS spectrometer all the more critical to achieving a clean x-ray probe and scatter signal. They also found Ar He-α emission in the measured spectra, most likely due to condensation of Ar onto the foil during cooling. A shroud was used to cover the target on cryogenic shots and limit the condensation; the same techniques are used in the present campaign.

A 1.5 mm long backlighter aperture was used to collimate the x-rays from the backlighter directed towards the shock. This aperture was initially 200 μm in diameter for the April 2013 shot day and then expanded to 400 μm and 600 μm variants for the September 2013 shot day.

In comparison to April 2013 experiments, the September 2013 experiments improved on x-ray throughput by widening the backlighter aperture from 200 μm to 400 μm and 600 μm, see Figure 4.9. Spatial filtering of the scattered x-rays

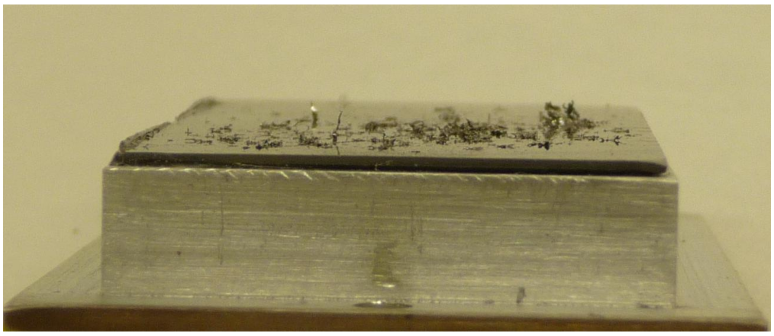

Figure 4.8: Visible damage to HOPG crystal on April 2013 shot day. The Be blast shield was damaged on all four cryo-XRTS shots on that shot day. Target was subsequently modified to mitigate shrapnel.

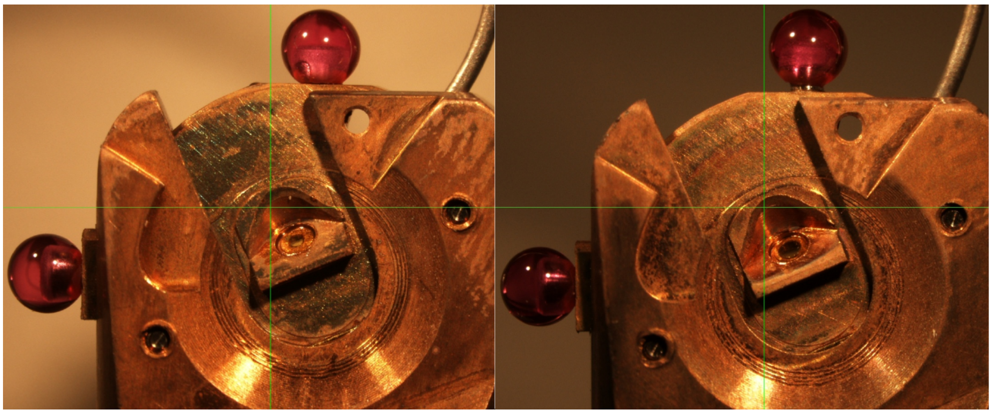

Figure 4.9: Two targets showing the increase in backlighter collimator size from 200 μm to 400 μm or 600 μm to increase x-ray throughput.

was improved by limiting the scattering channel with a 250 μm slit. This also helped to eliminate debris being fired into the GTS blast shield as occurred in the April 2013 experiments. A new HOPG crystal was installed for the September 2013 shot date due to damage, as seen in Figure 4.8, and to improve on spatial non-uniformities witnessed in the HOPG reflectivity.

4.4.2 Expected Signal Estimate

Thomson scattering has a small cross section which severely limits the number of photons that can be measured. It is therefore critical to maximize the number of photons in the probe beam, typically through gains in conversion efficiency, while limiting background noise through appropriate shielding, and making sure that the desired scattered photons are not lost along the way to the detector by increasing the reflectivity of the Bragg crystal and the sensitivity of the detector. Sources of noise include line and continuum emission from the shocked deuterium plasma, as well as lines from undesired stray elements such as Argon. In addition, the scattered x-ray signal must exceed the bremsstrahlung emission which approaches 10^{-7} J/ (eVsr) or 10^4 photons per eV (3). If the scattered signal exceeds the background continuum from bremsstrahlung, it is then simple enough to identify the regions of the signal that are dominated by continuum, do a least-squares fit, and remove the continuum spectra for analysis.

We can get a back of the envelope estimate of the expected signal from knowledge of the efficiencies of each step in the process along with geometric considerations. The total number of detected photons is given by (3):

$$N_{ph,d} = \left(\frac{E_L}{h\nu}\eta_x\right)\left(\frac{\Omega_{plasma}}{4\pi}\eta_{att}\right)\left(\frac{n_e\sigma_{Th}\ell}{(1+\alpha)^2}\right)\times\left(\frac{\Omega_{det}}{4\pi}R_{crystal}\eta_d\right) \tag{4.1}$$

where E_L is the laser energy, η_x is the conversion efficiency from laser energy to x-rays, η_{att} is the attenuation of x-rays by the dense plasma, Ω_{plasma} is the solid angle encompassed by the plasma relative to the x-ray source, Ω_{det} is the solid angle encompassed by the detector relative to the plasma, $R_{crystal}$ is the integrated reflectivity of the Bragg crystal, η_d is the efficiency of the detector (gain through the MCP, CCD, and filtering by foils). The $(1+\alpha)^{-2}$ factor is the attenuation of the inelastic peak.

Given 13 beams, with 500 J each, are incident on the Parylene-D foil at a conversion efficiency of $\eta_X \sim 0.2\%$ we get $(E_L/h\nu) \approx 2.7 \times 10^{16}$ photons of Cl Ly-α emission through 4π. The x-rays are then collimated through the backlighter aperture which has a solid angle of $\Omega_{plasma} = 0.06$ sr. We assume that the plasma attenuates the x-rays by a factor of $\eta_{att} \approx 1/e$ (3). Therefore the number of photons involved in the scattering off of the shocked deuterium is $(E_L/h\nu)\,\eta_x\,(\Omega_p/4\pi)\,\eta_{att} \approx 4.7 \times 10^{13}$ photons. Based on previous experiments and DRACO simulations we expect an electron density of $n_e = 2 \times 10^{23}$ cm^{-3} (31). Given the Thomson cross section $\sigma_{Th} = 6.65 \times 10^{-25}$ cm^2 and assuming the thickness of the deuterium region to be $\ell = 0.05$ cm the scattering fraction is $\ell n_e \sigma_{Th} = 6.7 \times 10^{-3}$ and the total number of scattered photons becomes $\sim 3.1 \times 10^{11}$.

The intensity of the inelastic feature is further attenuated by a factor of $(1+\alpha)^{-2}$ based on the differential cross section from Debye-Hückel theory, where the scattering parameter is $\alpha = 1.8$ for this experimental campaign. The solid angle of the spectrometer is $\Omega_{det} = 0.02$ sr and the reflectivity of the HOPG crystal is about $R_{crystal} \approx 50\%$. The sensitivity, or detection efficiency, of the MCP at ~ 3 keV is $\eta_d \approx 0.01$ (3, 130). These reduce the intensity by a factor of $(\Omega_{det}/4\pi) R_{crystal} \eta_d = 8.0 \times 10^{-6}$ bringing the total count of expected photons at the detector to $\sim 2.5 \times 10^6$ (124). This is comparable to previous experiments by Dr. Katerina Falk as well as other XRTS experiments of Glenzer *et al.* (82, 83, 131), Gregori *et al.* (132, 133) and García Saiz *et al.* (134). Further reductions in the signal may occur based on the position and thickness of the shock during backlighting.

4.5 Targets and shot plan

A few different targets were fielded on the OMEGA campaign. The main targets employed were the copper cells with cryogenically cooled liquid deuterium for measurement of XRTS on WDM. There were also a variety of "warm targets" whose main purpose was characterizing the backlighter and calibrating the GTS response. This section will go into the details of target configurations and alignment.

4.5.1 Warm Targets

Spectral calibration and spot profiling were achieved by firing 10 μm thick standalone Parylene-D foil targets. The foils measured 3 mm in diameter and were centrally mounted on 3 mm × 3 mm CH frames which had a 2 mm diameter hole in the center. Spatial profiling was measured with XRPHCs and the backlighter foil at 1500 μm away from TCC, oriented towards $\theta = 37.73°$, $\phi = 61.18°$; this is roughly in the direction towards port P2 and the same orientation as on the

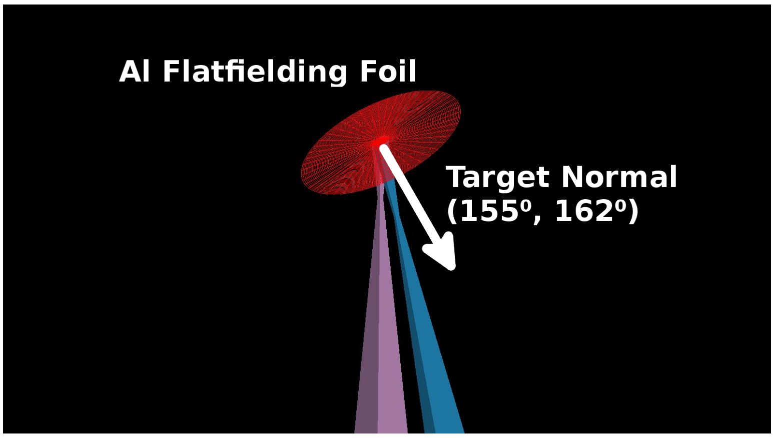

Figure 4.10: Al foil in orientation for flatfielding shot. Figure generated in VisRad (135).

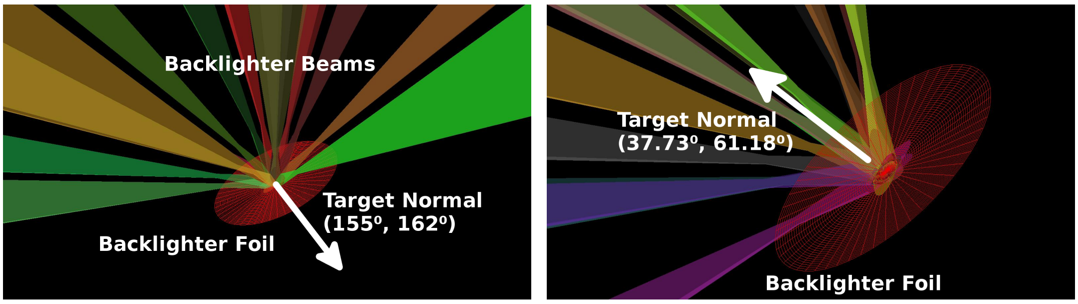

Figure 4.11: *Left*: Parylene-D foil in orientation for spectral calibration shot. *Right*: Backlighter foil in orientation for spatial profile shot. Figures generated in VisRad (135).

cryo XRTS targets. An extra XRPHC was mounted on port P2C to measure the plasma spot quality, as none of the standard XRPHCs had a good view on target. Spectral calibration of the instrument function was done with a Parylene-D foil at TCC oriented towards beam line 17 (port B17, $\theta = 154.97°$, $\phi = 162°$). This is directly opposite to TIM6, giving the GTS spectrometer a clear view of the rear surface of the foil during ablation. Both foil orientations are depicted in Figure 4.11. In addition to the warm Parylene-D targets, a 12.5 μm thick Al target was placed at TCC and oriented towards B17 for the purpose of flatfielding the spectrometer (i.e. correcting for variations in gain and sensitivity across different regions of the CCD/MCP system); see Figure 4.10.

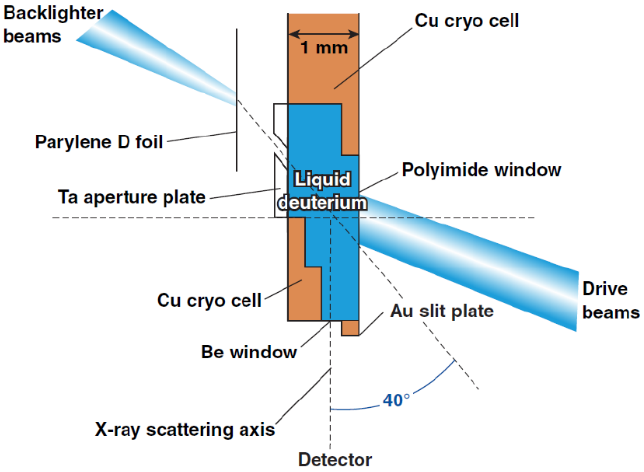

Figure 4.12: A simple, cross-sectional schematic of the cryo-cell. Important features to note are the Au slit plate which narrows the view towards the detector and blocks x-rays generated near the ablation surface, and the Be window which allows for viewing the scattered x-rays while keeping the deuterium in the cell.

4.5.2 Cryogenic Targets

Cryogenic targets consisted of a copper cell mounted on a cryogenic finger. The cell has an 8 μm polyimide ablator window on one side and 10 μm Parylene-D foil backlighter towards the opposite side. Deuterium was filled into the cell through a Cu fill tube to a pressure of $P_0 = 20$ psi $\sim 1.38 \times 10^5$ Pa. The cell was cooled to a temperature of 18 K while visually monitoring the cell through the ASBO telescope on TIM5 for signs of phase change to liquid. A scattering channel on the underside of the target is pointed towards the GTS spectrometer on TIM6. Gold (100 μm) and Iron (50 or 100 μm) shields are placed around the channel to block the spectrometer from viewing direct emissions, particularly x-rays, from the drive and backlighter sides. A simple schematic of the target is shown in Figure 4.12 and the exterior shielding can be seen in Figure 4.13. Targets were designed by Mark Bonino of LLE.

A scattering aperture sits between the backlighter foil and the portion of the cell where the bulk of the D_2 sits. The aperture was made from a Ta plate with a pinhole and is 1.5 mm long. This aperture was initially 200 μm in diameter for

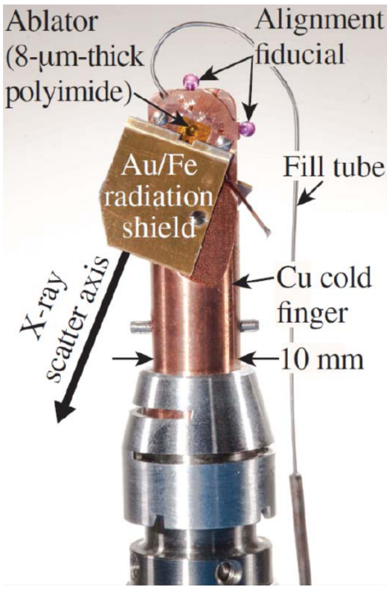

Figure 4.13: Picture of the cryo-XRTS target from the front (H14) side. Here, the radiation shielding and the scattering axis for the x-rays going towards the GTS are clearly visible.

shots in April 2013 and subsequently expanded to 400 μm and 600 μm to increase x-ray throughput for the September 2013 shot day. The scattering channel was machined to 500 μm wide and could be reduced to 250 μm by adding a Au plate to improve spatial resolution. Two precisely measured spherical fiducials (ruby tooling balls) are mounted on the top and side of the target for alignment purposes. During cooling a shroud is placed over the target to reduce the condensation of residual Argon onto the target; the shroud is retracted immediately prior to the shot.

4.5.3 Alignment procedure

Cryogenic targets were mounted on cryo carts 4 and 6 from port P1, the upper pylon of the cryogenic target handling system (CTHS), at the top of the OMEGA target chamber, while warm, foil targets were lowered from port H2 using the target positioning system (TPS) (129). The targets are aligned using the target viewing system (TVS) which has X and Y projected shadowgraphs of the target.

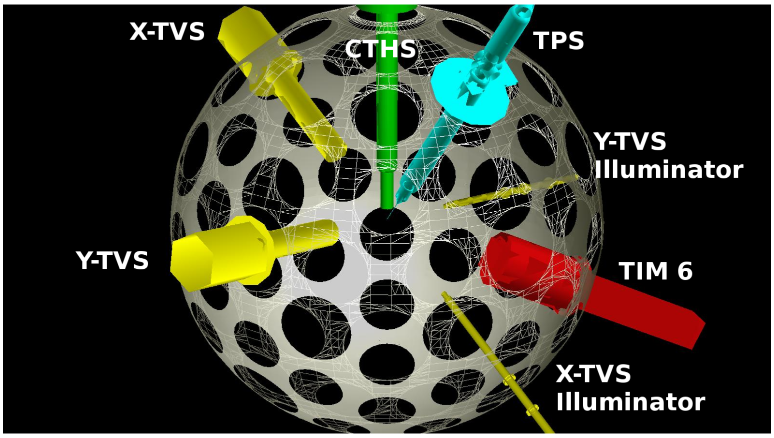

Figure 4.14: The OMEGA chamber as viewed from port P2C. The cryogenic targets are lowered into the chambers using the CTHS and aligned using the X-TVS and Y-TVS cameras. The scattered spectra are viewed on the GTS, mounted on TIM 6. Figure generated in VisRad (135).

The X-TVS is in port P5 ($\theta = 63.44°$, $\phi = 270°$) and the Y-TVS is in port H6A ($\theta = 77.28°$, $\phi = 19.96°$). See Figure 4.14 for a visualization of the chamber.

Foil targets are moved towards TCC until they are visible on the TVS. The targets are then rotated to the target normal corresponding to the type of shot. VisRad software was used to generate alignment reticles which were overlayed on the TVS monitors to accurately position the targets for each shot. Both the X-TVS and Y-TVS reticles must be in agreement for the target to be correctly positioned, Figure 4.15.

The cryo targets required more precise positioning due to the complex nature of their fabrication. The alignment fiducials of each individual target were precisely measured and compared to CAD models. The metrologized values were used to generate a unique set of alignment reticles for each target in VisRad. Prior to aligning the target, the ASBO telescope in TIM5 had to be aligned and focused by inserting simple grid at TCC using TPS 2. Then the cryo target is positioned near TCC and the Cryogenic Target Handling System (CTHS) translation axes are used to match the fiducials with the reticles on the TVS, Figure 4.16.

During the alignment procedure the shroud is lowered as the target is being cooled. Once everything is aligned the ASBO telescope peers through the trans-

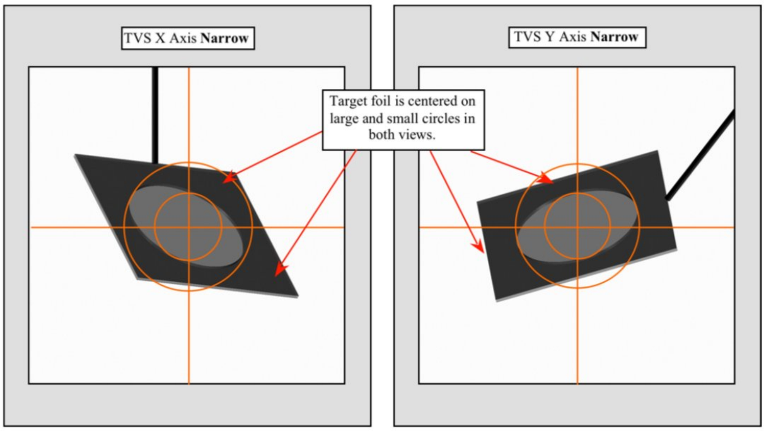

Figure 4.15: *Left*: X-TVS view of standalone Parylene-D foil on a mount of CH foil. *Right*: Same, but Y-TVS view. The circular foils appear elliptical due to the angle with respect to the TVS. The semi-major and semi-minor axes of the projected foil view are aligned to reticles in the X-TVS and Y-TVS views to ensure correct orientation of the target prior to the shot. Figures generated in VisRad (135).

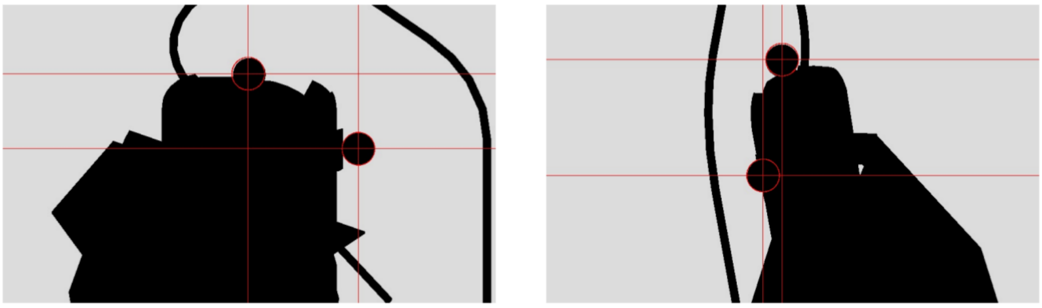

Figure 4.16: *Left*: X-TVS view of the target. The spherical ruby fiducials of the target are aligned to the red crosshairs to ensure correct target orientation. *Right*: Same as left, except from Y-TVS view. Figures generated in VisRad (135).

parent polyimide window to watch the transition from gaseous to liquid phase. The shroud is removed and any drift in alignment is compensated for prior to shooting.

4.6 Target Shots

This section provides a brief summary of each shot configuration on the OMEGA campaign, analogous to the manner in which shots would be defined prior to the shot day and then called up using shot request forms (SRFs).

Cryo XRTS shot

The full XRTS cryo targets, consisting of a copper cell, polyimide ablator window, and Parylene-D backlighter, are used for these shots. Drive beams ablate the polyimide from the H14 side and backlighter beams ablate the Parylene-D from the H7 side of the target chamber. The GTS spectrometer measures the spectra scattered from the shocked liquid deuterium to obtain the plasma parameters (n_e, T_e, and Z). The drive laser has an intensity of $10^{14}\,\mathrm{W/cm^2}$ driving the shock for 6 ns while the backlighter has an intensity of $10^{15}\,\mathrm{W/cm^2}$ ablating the Parylene-D and producing strong Cl Ly-α emission for 1 ns. ASBO telescope is used to view the deuterium during cooling and confirm the phase change from gas to liquid. A shroud is used during cooling to reduce the amount of condensation, in particular Argon, on the target.

Spectral calibration shot

A single Parylene-D foil is mounted on a thin shaft and placed at TCC. The target is ablated and the emitted Cl Ly-α line is measured on the spectrometer and used to calibrate spectral position and instrument function. Beams from port B17 were used to drive the foil as these are directly opposite TIM6 where the GTS spectrometer is mounted. The surface normal of the foil was oriented to point at B17. Beam numbers: 11,17,10,22,26,20,31,37,46,55,56,61,68 were used with 500 J/beam focused at 1500 μm from TCC with a 200 μm spot size. Spectral calibration was done at least once for each shot day to ensure adequate configuration and obtain an instrument function which can then be used for fitting simulated spectra to obtain plasma parameters.

Backlighter spatial profile shot

These shots are similar to the spectral calibration shot in that it is just the Parylene-D foil and no other parts to the target, but the foil is oriented the same way the backlighter is oriented on the full cryo XRTS shots. In addition, the same H7 side backlighter beams are used to ablate the foil. In this orientation the GTS spectrometer is not of much use, so the primary diagnostics are the pinhole cameras which are used to examine the profile of the ablation spot on the foil to ensure adequate alignment in the system.

Flatfield shot

These shots check the first order flatfield spatial response of the GTS spectrometer. An Al foil is placed at TCC and driven by beams from the B17 side. The foil is oriented same as the spectral calibration shot such that the spectrometer may view the emission through the foil. Just two beams were used: 25 and 64, each with 250 J/beam (UV - FCC detune) at a 200 μm spot size focused at TCC.

5

XRTS experiment at OMEGA

> *You should call it entropy, for two reasons. In the first place your uncertainty function has been used in statistical mechanics under that name, so it already has a name. In the second place, and more important, no one really knows what entropy really is, so in a debate you will always have the advantage.*
>
> —John von Neumann on Claude Shannon's uncertainty function,
> *Scientific American Vol. 225 No. 3, (1971), p. 180.*

5.1 Introduction

In the previous chapters we discussed the possible foundations for WDM theory and methods for experimentally testing these hypotheses through use of an XRTS probe. In this chapter we will finally see the results of experiments on the OMEGA laser facility probing shocked warm dense deuterium via XRTS in the collective scattering regime. The results will consist of measured scattering spectra from which we will extract plasma parameters by fitting simulated data. The scatter parameter takes on a value of $\alpha \sim 1.8$ for the experiment's geometry and plasma parameters as estimated from simulations and prior experiments (31). The spectra are right on the transition between collective and non-collective regimes making them sensitive to both electron temperature and density.

I also aim to demonstrate that the extensions to XRTS for inhomogeneous plasmas, discussed in Chapter 3, are indeed applicable for the analysis of these experimental results. If these inhomogeneous corrections were not used it would yield significant errors in the inference of electron temperature from detailed balance considerations. Due to a lack of other independent instruments for diagnosing the plasma parameters, the conditions inferred from the XRTS spectra will be compared to previous experiments in the non-collective regime by Dr. Falk and Dr. Regan (30, 31), as well as hydrocode simulations. The experiments in the non-collective regime were able to confirm the plasma parameters through use of streaked optical pyrometry (SOP) and velocity interferometry (VISAR) which were conducted on shots separate from the XRTS shots, but with a nearly identical platform (30).

There were two separate shot days for this campaign; the first was in April of 2013 and the second was in September of 2013. None of the XRTS shots from April yielded a significant plasmon signal and shots consistently damaged the Be blast shield on the GTS. Targets for the September shot day were modified to reduce debris by narrowing the scatter channel, and removing excess mass from the target. In addition, the scattered signal was increased by widening the collimator of the x-ray backlighter. The HOPG crystal in the GTS was replaced due to the damage layer and spatial non-uniformities seen in the spectra. On the September shot day, there was a single strip on one of the shots where we measured plasmons. Therefore the following chapter will focus on the analysis of this data along with calibration data taken on the same day.

5.2 Experimental Conditions

Warm dense matter was formed by shock compression of cryogenically cooled, liquid deuterium stored in a copper cell at 20 psi. The shock was initiated by ablating an 8μm thick polyimide window covering one face of the copper cell. This foil was driven by 12 beams at $\sim 10^{14}$ W/cm^2. Each beam was frequency-tripled to 3ω ($\lambda = 351$ nm) to enhance laser-plasma coupling (15). The total duration of the drive was 6 ns and was created by firing pairs of beams, 1 ns each, in a staggered fashion so as to maintain a level temporal intensity profile. The spatial intensity was kept level by use of phase plates and polarization smoothing (136). All of the beams were square pulses, and the frequency conversion crystals (FCC) were slightly detuned, primarily to reduce the energy of the higher angle beams. The first 3 ns of the drive consisted of higher angle beams detuned to 300 J/beam while the last 3 ns were detuned to 420 J/beam.

The XRTS probe beam was generated by ablating a 10 μm thick Parylene-D foil with 13 beams at 10^{15} W/cm^2 over 1 ns with a spot size of 200 μm. The plasma generated from this foil emits Cl Ly-α x-rays at 2960 eV which are collimated through a pinhole towards the oncoming deuterium shock. The x-rays scatter off the shock and are collected through a 250 μm to 500 μm wide scattering channel directed towards a gated Thomson spectrometer (GTS). The geometry of the target was set to obtain a scattering angle of $\theta = 40° \pm 7.6°$, where the uncertainty in scatter angle is due to the width of the backlighter collimator (width of 400 μm for the shot where we see significant XRTS signal).

The GTS consists of a HOPG crystal for dispersing the x-rays and a XRFC for recording the spectra. The XRFC had four strips each of which was set to measure for 250 ps and staggered so that the total duration of temporally resolved measurements was 1 ns, consistent with the backlighter drive duration. On the target, Au and Fe radiation shields, and the scattering channel, obscured the GTS from radiation sources other than the deuterium shock. A Be shield on the GTS further filtered any visible radiation while protecting the camera from debris. Full details of the experimental setup may be found in chapter 4.

5.3 Hydrodynamic simulations

Simulations corresponding to the previously described experimental conditions were conducted with the 2D radiation-hydrodynamic DRACO code and the 1D rad-hydro code, HELIOS (73, 76). For a drive intensity of 10^{14} W/cm^2 the simulations yield electron densities of $n_e \sim 1.0 \times 10^{23}$ cm^{-3}, electron temperatures of $T_e \sim 10$ eV, and ionization of $Z \sim 1$ in the shocked region.

5.3.1 DRACO 2D hydrocode

DRACO radiation hydrocode simulations were run by Suxing Hu of LLE for the aforementioned experimental parameters. The simulations were 2D and cylindrically symmetric about the normal of the ablator foil. The mesh size was adaptive to better resolve regions of interest, in particular, those regions closest to the laser axis and at the shock. The results of these simulations at a time step of 5 ns after the start of the drive, can be seen in Figure 5.1. Here the shock has traveled $\sim 250\,\mu$m into the cryo cell. The shocked deuterium occupies a region of $\sim 70\,\mu$m. The plasma parameters in the shock are $T_e = 11 \pm 1\,$eV, $n_e = 1.6 \pm 0.1 \times 10^{23}\,$cm^{-3} and $Z = 0.7\,(-0.1, +0.3)$.

5.3.2 HELIOS 1D hydrocode

HELIOS simulations were run by myself using Prism software of the same name. Here, the PROPACEOS equation of state library was used for opacity and EOS models. The simulations were run for planar geometry with deuterium filling 20 zones from 0.0cm to 0.1cm. The ablator was composed of CH, also filling 20 zones from 0.1 cm to 0.1008 cm. The mass density of liquid deuterium is 0.164 g/cm^3 at 1 bar at boiling point ($\sim$ 23 K) (137). The deuterium in the cryo cell was $\sim$ 20 psi, but this will not significantly change the mass density since at this temperature and density the deuterium is effectively an incompressible fluid with respect to standard, mechanical compression (of course, laser-driven shocks can yield Mbar pressures and are able to compress the deuterium, but what is of interest here is the initial condition prior to ablation).

The Spitzer model was used to describe thermal conductive effects, with a flux limiter of 0.06 being applied. An LTE atomic model was chosen and a diffusion model with 50 frequency groups was used for radiation transport effects. The results of these simulations are presented in Figure 5.2. At $t = 5$ ns the shock has traveled $\sim 400\ \mu$m and has $T_e = 20 \pm 5$ eV, $n_e = 1.3 \pm 0.1 \times 10^{23}$ cm^{-3} and $Z = 0.75 \pm 0.05$. These values are similar to those obtained from DRACO simulations, though some variability is expected due to the use of different EOS tables and 2D versus 1D modeling.

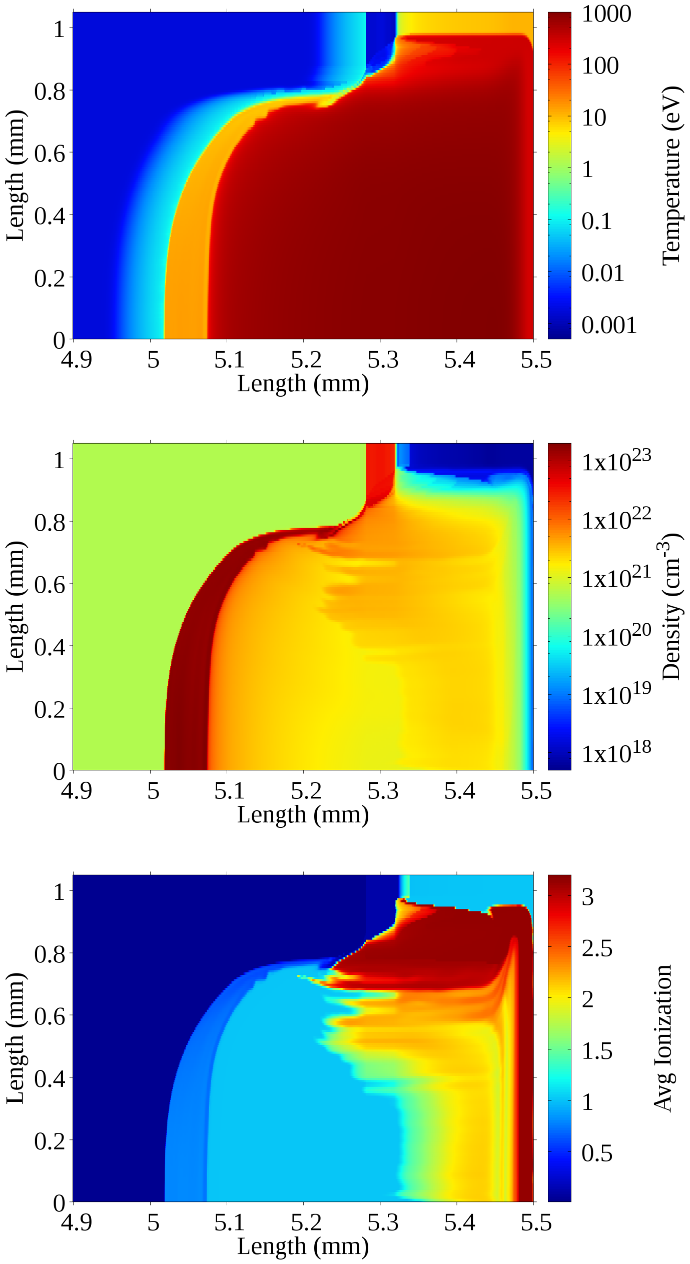

Figure 5.1: Results of DRACO 2D hydrocode simulations at $t = 5$ ns after the initiation of the laser driving the shock. The laser is incident at the 5.32 mm position on the horizontal axis and the shock propagates to the left. *Top*: Electron temperature (eV). *Middle*: Electron density in cm^{-3}. *Bottom*: Average ionization.

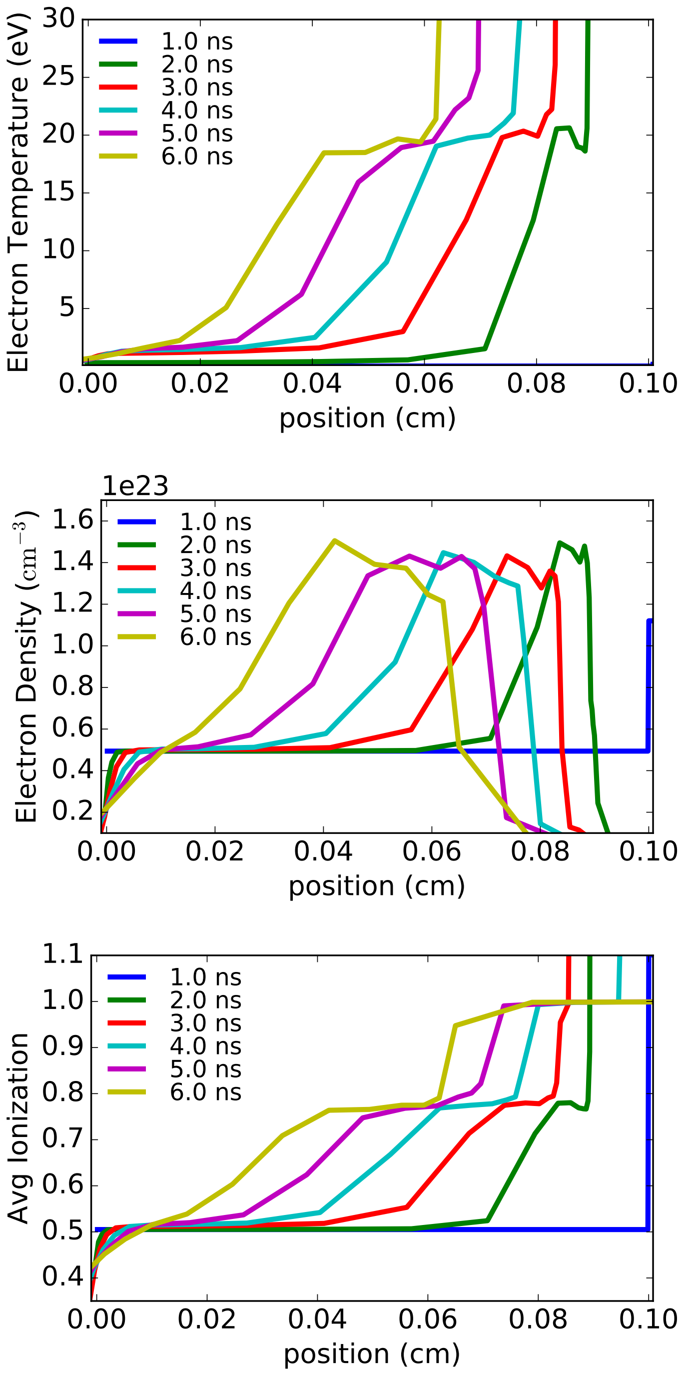

Figure 5.2: Results of HELIOS 1D hydrocode simulations at 1 ns time steps where $t = 0$ ns is the start of the drive laser. The laser is incident at the 0.108 cm position with respect to the plotted axis, and the shock propagates to the left. *Top*: Electron temperature (eV). *Middle*: Electron density in cm^{-3}. *Bottom*: Average ionization.

5.4 XRTS analysis

The GTS yields 4 strips of time resolved data which may be calibrated and processed to yield measured XRTS spectra. Each strip has spectral resolution on the horizontal axis and spatial resolution on the vertical axis. Each pixel has a number of counts corresponding to the intensity of the signal incident on that pixel. These intensities are integrated in the spatial direction across the strip to yield a graph of counts against pixel position on the spectral axis. The horizontal axis is then converted into spectral units of photon energy (eV) by application of a dispersion curve corresponding to the geometry of the camera and Bragg crystal. The intensity is then flatfielded to account for variations in Bragg crystal reflectivity and sensitivity in the MCP and CCD. For sufficiently low intensities flatfielding is unnecessary and a simple subtraction of the background, linear continuum is required. The resultant data is fairly noisy, therefore a smoothing filter is applied to reduce the high frequency variations in the signal and more clearly show the underlying scattered spectra for easier fitting. Finally simulations are run for a number of plasma parameters, varying around the temperature, density, ionization, and gradient scale lengths expected from simulations and prior experiments done in the non-collective regime. An optimal fit is found and the interpretation is discussed. Each of these steps in the analysis process is demonstrated and described in detail in the subsequent sections.

5.4.1 Instrument function

Warm target shots were taken with simply mounted Parylene-D foils oriented with surface normal facing the GTS to obtain an instrument function for the scattered spectra (details of the shot can be found in chapter 4). This instrument function can then be convolved with simulated spectra so that simulations may then be adequately fitted to the measured data which is simpler than the ill-posed problem of deconvolving the instrument function from the measured spectra. Though it should be noted that deconvolution, if done under adequate constraints, can increase the spectral resolution to beyond that which is expected for a particular detector configuration (aptly named *super-resolution*) (138). The main purpose of obtaining the instrument function is to capture the effects of

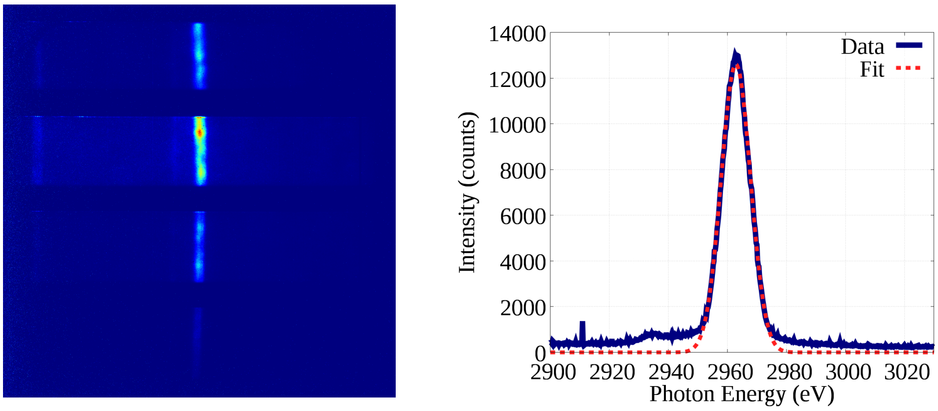

Figure 5.3: *Left*: XRS image from spectral calibration shot. The four strips set to different time delays are visible. *Right, Blue*: Spatially-integrated intensity of the Parylene-D backligher as obtained from the 4th strip of the XRS image seen on the left. The timing was $t = 0.75 - 1.00\,\mathrm{ns}$ after backlighter drive was initiated. *Right, Red*: Gaussian fit with peak at $E_0 = 2962.9$ eV and $\sigma = 5.0$ eV. The fit will be used as an instrument function, to be convolved with simulated XRTS spectra to obtain fits appropriate to the experimental setup. The peak is not quite at 2960 eV suggesting that the dispersion curve is slightly shifted. Satellites are relatively small in intensity and should not interfere significantly with measurement of the scattered plasmon signals.

instrument broadening which may lead to errors in estimated plasma parameters sensitive to other broadening mechanisms such as the Doppler effect. The other purpose of these warm target shots is to assess the importance of satellites around the main Cl Ly-α line and their possible effect on the scattered signal. If the satellites are strong then they may obfuscate the plasmons in the scattered signal as they will lie in a similar spectral range.

Figure 5.3 shows the measured spectrum from one of these Parylene-D shots. The spectrum is fitted with a Gaussian distribution function which yields $\sigma = 5.0\,\mathrm{eV}$. It is also seen that the satellites are relatively low in intensity in comparison to that of the Cl Ly-α. Furthermore, the Cl Ly-α line is at about 2963 eV confirming that the dispersion curve used in converting the image from pixels to photon energy has been adequately modeled and applied, though it may need to be shifted by $\sim 3\,\mathrm{eV}$ to correctly center the backlighter about 2960 eV. This shift was applied in the subsequent analysis such that the elastic peak measured on cryo XRTS shots lies squarely on 2960 eV.

It was found that the single Gaussian was insufficient for modeling the instrument function as it did not reproduce other features seen in the elastic peak in strip 4. The single Gaussian was retained while adding three other fitted Gaussians to form a multi-Gaussian instrument function which more accurately reproduced the data when convolved with simulations. This improved instrument function is displayed in the subsequent figures, where it is used. These other features which the multi-Gaussian describes may be due to the geometry of the cryogenic cell causing reflections or appearing as an extended source as viewed from the spectrometer. Such features would not be seen when imaging a standalone foil pointed at the spectrometer, as was done in the instrument function shots.

5.4.2 Dispersion calculation

A dispersion curve is a set of data mapping pixel position on the CCD to spectral units. Application of the dispersion curve is therefore a straight-forward process. The trickier part is obtaining the dispersion curve. In a standard spectroscopic setup in the visible range one would use a reference such as a mercury or argon pen lamp, identify the lines seen on the spectrometer and fit a curve. An approximate dispersion curve can be generated by inputing the precisely measured geometry of the spectrometer into a ray tracing program. The dispersion curve is applied to the data and we can check for consistency by examining the positions of lines such as Cl Ly-α, its satellites, and Ar He-like and Li-like lines and matching them against their known values (139, 140). We can see in Figure 5.3 that the applied dispersion curve shows the Cl Ly-α line at 2963.0 eV which is close to the known value. The same dispersion curve was applied to another strip acquiring data at $t = 4.55 - 4.80$ ns where Argon lines are visible; see Figure 5.4. The He-like $1S^2 - 1S2P$ singlet and triplet lines are at 3138 eV $\left(3.951\ \text{Å}\right)$ and 3122 eV $\left(3.971\ \text{Å}\right)$ respectively. While the Li-like $1S^2 2P - 1S2P^2$ line is at 3110 eV $\left(3.987\ \text{Å}\right)$ consistent with known values (141).

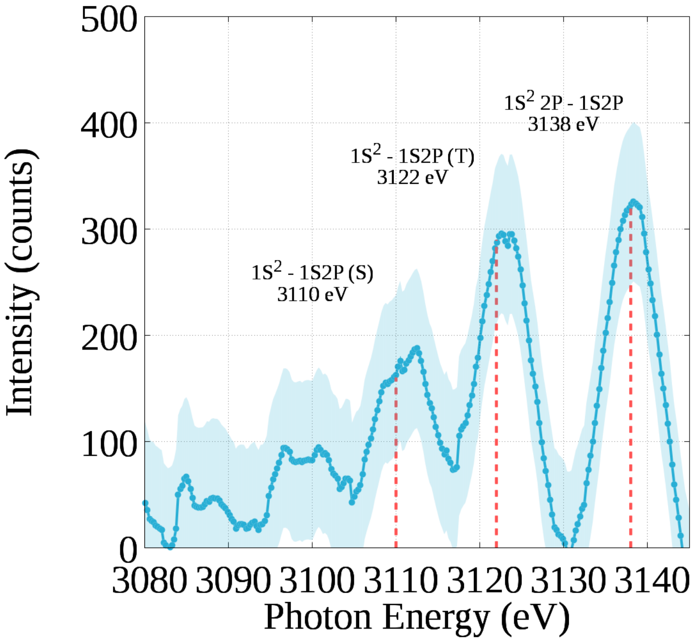

Figure 5.4: Spectra obtained from second strip on the MCP/CCD, $t = 0.25 - 0.50$ ns after start of CCD acquisition, showing He-like and Li-like Argon spectra. The dashed red lines denote the true photon energy of these lines. The observed lines are consistent with known values, further justifying the accuracy of the applied dispersion curve.

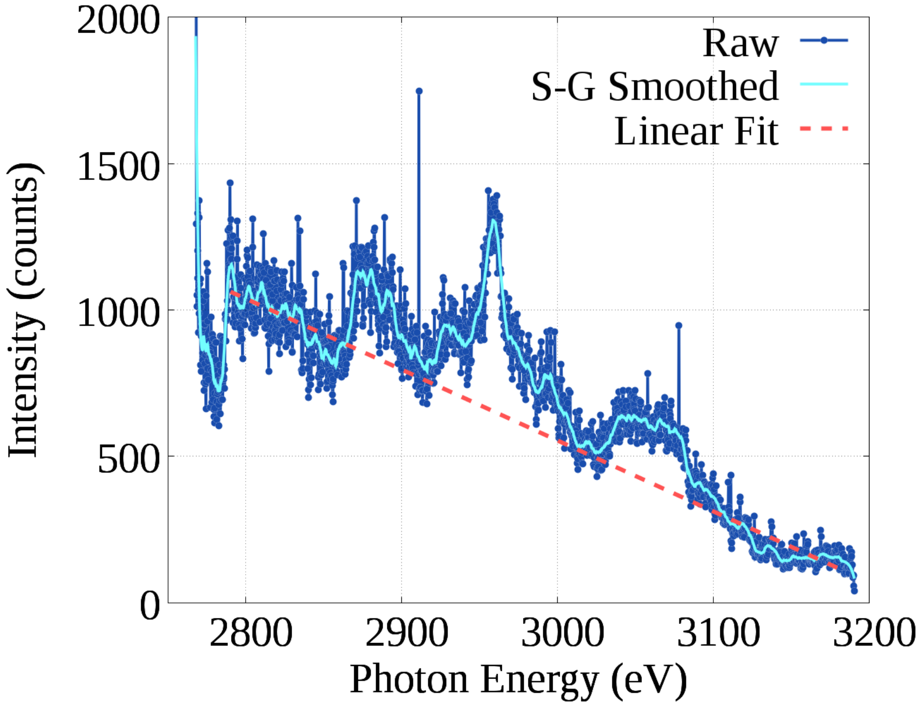

Figure 5.5: *Dark Blue*: Spatially integrated data from strip 4 of XRS. *Light Blue*: Savitzky-Golay smoothed data. *Red*: Linear fit for subtracting the continuum signal for flat-fielding. Strip 4 was activated for $t = 5.05 - 5.30$ ns.

5.4.3 Flatfield and linear continuum

For spectral data obtained at high intensities the HOPG crystal reflectivity and sensitivity of the MCP and CCD will vary nonlinearly. There is no good way to compensate for this from a purely theoretical perspective, so we must characterize the response of the instrument to intense x-rays. This process is known as *flatfielding*.

We were able to obtain flatfielding data on the April shot day, but not on the September shot day, and due to the replacement of the HOPG crystal the previously obtained flatfield is not as reliable for analysis of data from September. Fortunately, a flat field was not necessary as the measured intensity was sufficiently low as to not introduce a nonlinear response. Though another adjustment was required. It is seen in the data that the intensity rises as one goes from one end of the spectrum to the other and that this effect is consistent across strips at different times. This is from background continuum emission to which, at low intensities, the detector responds approximately linearly. Continuum emission due to bremsstrahlung can be modeled by (3)

$$P_{ff}\left(\hbar\omega\right)d\left(\hbar\omega\right)=\frac{32}{3}\left(\frac{\pi}{3}\right)^{1/2}r_0c\left(\frac{E_H}{k_BT_e}\right)^{1/2}\times Z^2n_in_eg\exp\left[\frac{-\hbar\omega}{k_BT_e}\right]d\left(\hbar\omega\right) \quad (5.1)$$

where P_{ff} is the emission power density from free-free bremsstrahlung, $\hbar\omega$ is the photon energy, r_0 is the classical electron radius, c is the speed of light, E_H is the ionization energy of hydrogen, and g is the gaunt factor.

With temperatures at the laser-plasma interface reaching as much as $T_e\sim 1\,\text{keV}$, as modeled by DRACO simulations, the bremsstrahlung spectrum around $\hbar\omega\sim 2.96\,\text{keV}$ is close to linear. Therefore, we use curve fitting to recover the measured background continuum spectrum due to bremsstrahlung, as suggested by Kunze (142). A linear fit is applied to those regions of the data where there are no obvious spectral lines and towards the edges of the acquired data to reduce error. The fitted line is then subtracted from the data resulting in a flatfielded spectrum as seen in Figure 5.5.

5.4.4 Simulation fits

With the data fully calibrated we finally proceed with obtaining the plasma parameters. As with many spectral analysis techniques XRTS analysis is a *forward process*, meaning that we take some model $\mathscr{F}$, which we think will adequately describe the system/measurement, y, feed it a good guess as to what the system conditions are, x, and then compare the output to measured data. If the comparison is good then we infer that the guessed conditions may describe the system.

$$\mathscr{F}\left[x\right]\to y \quad (5.2)$$

This is in contrast to the *inverse process* of analysis by which we have a model (function) which takes parameters as input and the measured value as output, and then we invert the function such that it takes the measured values as input and gives us what we want, the system parameters.

$$x \leftarrow \mathscr{F}^{-1}\left[y\right] \tag{5.3}$$

This distinction is important since the forward process is often applied when the model is highly non-linear and not easily invertible, therefore a number of different system parameters may yield similar simulated data. The guess-work and the valid parameter space is reduced by other known physical constraints. In the case of the OMEGA data, we may rely on rad-hydro simulations and prior experiments using XRTS, SOP, and VISAR, to inform what values of electron density, temperature and ionization we put into the XRTS simulations. Beyond that, we must check the sensitivity of the model to plasma parameters by varying them near the best fit which also gives an estimate on the errors in the best fit parameters.

Examining the data in Figure 5.5 there is a significant amount of high frequency noise which makes it difficult to clearly see the underlying plasmon peaks. We apply a Savitzky-Golay smoothing filter with polynomial order 3 with a window size of 51 points. This is a convolution filter which smooths the data by least-squares fitting a polynomial across the first n points, replacing the data with the fitted values in that region, stepping the window forward by one point and fitting again. The process is repeated until the entire dataset is replaced with locally fitted polynomials (143). The result of the smoothing can be seen in Figure 5.5.

The measured spectrum was obtained at a scatter angle of $\theta = 40°$ and a probe beam at 2960 eV. This yields a scattered wavenumber of $k \sim 1 \times 10^{10}\,\mathrm{m}^{-1}$. From hydrocode simulations and prior experiments we expect temperatures and densities of $T_e \sim$ 8eV and $n_e \sim 2.2 \times 10^{23}\,\mathrm{cm}^{-3}$ respectively (31). This gives a scatter parameter of $\alpha \sim 1.8$. The scattered spectra will thus be in the collective regime, but the proximity to the non-collective regime ensures that the spectra are sensitive to both electron temperature and density.

Different portions of the spectra are sensitive to different plasma parameters which eases the burden of attempting to fit the simulations by hand. The inelastic shift, that is the distance between the elastic and inelastic (plasmon) peaks is sensitive to density. In the collective scattering regime, the shift should be approximately a plasma frequency in energy $\sim \hbar\omega_{pe}$ which is related to why these peaks are referred to as plasmons. The intensity of the spectrum depends on the number of scatter sites and so it is most sensitive to ionization and somewhat sensitive to density. The relative intensity of the elastic (ion feature) and inelastic (electron feature) peaks is especially sensitive to the proportion of free electrons. The width of the peaks is sensitive to temperature via the Doppler broadening mechanism. The relative intensity of the upshifted and downshifted plasmon peaks is strongly dependent on the temperature because of detailed balance, as shown in Eq. 2.19 and discussed in Chapter 3 (16).

It is evident from the smoothed data that the upshifted and downshifted plasmon peaks are of approximately the same intensity. By detailed balance this would imply a large electron temperature, which should also be seen in the Doppler broadening of the peaks. Focusing on fitting to the downshifted peak, as seen in Figures 5.6, 5.7, we get a density of $n_e = 3.0 \pm 1.0 \times 10^{23}\,\mathrm{cm}^{-3}$, temperature of $T_e = 20 \pm 10$ eV and ionization of $Z = 1\,(-0.2, +0.0)$, but the intensity of the upshifted peak severely undershoots that of the measurement. Trying to increase the temperature only leads to catastrophe as the plasmons are broadened far beyond the measured data. This would suggest a violation of detailed balance.

As discussed in Chapter 3, such violations of detailed balance are possible for collective XRTS probing of inhomogeneous systems where the scale length of the inhomogeneity Λ is comparable to the probing scale length $\lambda_p \approx 1/k$. Inhomogeneous XRTS simulations yield good fits to both the upshifted and downshifted plasmons as seen in Figure 5.8. For the inhomogeneous fit we have plasma parameters of $n_e = 4.3\,(-0.3, +0.7) \times 10^{23}\,\mathrm{cm}^{-3}$, $T_e = 12\,(-2, +8)$ eV, $Z = 1$, and $\Lambda = 1.33\,(-0.13, +0.67)$ nm. It should be noted, that the ionization here is somewhat meaningless, as there is no simulated elastic peak to normalize the inelastic peaks to. Additionally, the temperature may be in significant error since detailed balance is violated and the Doppler broadening of the plasmons is smaller than the instrument broadening. Previous experiments in the non-collective regime, where inhomogeneous effects are not present, gave values of $n_e \sim 2.2 \times 10^{23}\,\mathrm{cm}^{-3}$, $T_e \sim 8$ eV, $Z \sim 1$. These are summarized in Table 5.1 along with the plasma parameters obtained from hydro-code simulations.

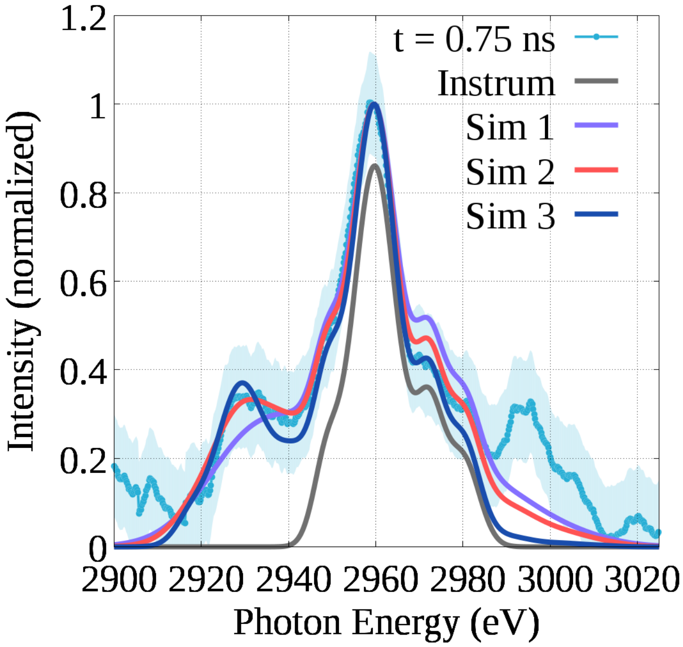

Figure 5.6: Homogenous simulation fits to measured spectra, obtaining sensitivity to temperature and density. *Instrum:* Multi-Gaussian instrument function. *Teal*: Data from GTS strip 4 at $t = 0.75 - 1.00\,\mathrm{ns}$ after the spectrometer starts acquiring data. The data has been smoothed and the linear continuum has been removed. The shaded region represents the standard deviation of the unsmoothed data. *Sim 1, purple*: $n_e = 2.0 \times 10^{23}$ cm^{-3}, $T_e = 30$ eV and $Z = 1.0$. *Sim 2, red*: $n_e = 3.0 \times 10^{23}$ cm^{-3}, $T_e = 20$ eV and $Z = 1.0$. *Sim 3, black*: $n_e = 4.0 \times 10^{23}$ cm^{-3}, $T_e = 10$ eV and $Z = 1.0$. All simulations are done with the RPA model.

There is clearly a disparity between the inhomogeneous collective and the non-collective scattering results. Although, it is interesting to note that both the electron temperature and the electron density are larger by a factor of 2 in the inhomogeneous, collective case. This would mean that the screening length, and thus the scattering parameter, would be equal for the same scattering geometry. To some extent, the disparity between the collective and non-collective results is bridged by the collective, homogeneous fits, whose density of $n_e \sim 3.0 \times 10^{23}\,\mathrm{cm}^{-3}$ lies between the collective, inhomogeneous and the non-collective results.

We may further justify the application of the inhomogeneous theory to the XRTS spectra by observing that in strong shocks the shock thickness, that is the

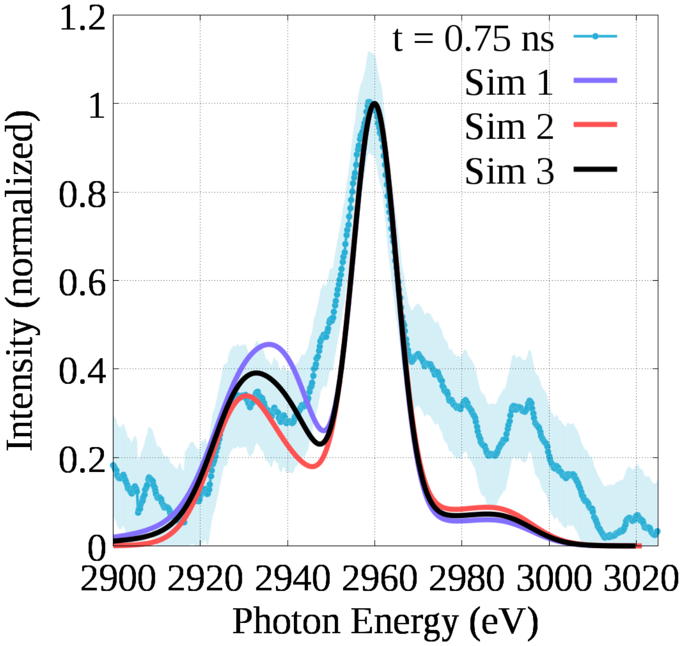

Figure 5.7: Homogenous simulation fits to measured spectra, obtaining sensitivity to ionization. Here, the single-Gaussian instrument is used for simplicity as the ratio of the elastic and inelastic peaks is the critical parameter. *Teal*: Data from GTS strip 4 at $t = 0.75 - 1.00$ ns after the spectrometer starts acquiring data. The data has been smoothed and the linear continuum has been removed. The shaded region represents the standard deviation of the unsmoothed data. All three simulations are $n_e = 3.0 \times 10^{23}\,\mathrm{cm}^{-3}$, $T_e = 20\,\mathrm{eV}$ with only ionization varying. *Sim 1, purple*: $Z = 0.8$. *Sim 2, red*: $Z = 1.0$. *Sim 3, black*: $Z = 0.9$. All simulations are done with the RPA model.

Method	T_e (eV)	n_e ($10^{23}\,\mathrm{cm}^{-3}$)	Z
DRACO	11 ± 1	1.6 ± 0.1	$0.7\,(-0.1, +0.3)$
HELIOS	20 ± 5	1.3 ± 0.1	0.75 ± 0.05
Collective, homog.	20 ± 10	3.0 ± 1.0	$1.0\,(-0.2, +0.0)$
Collective, inhomog.	$12\,(-2, +8)$	$4.3\,(-0.3, +0.7)$	(1.0)
Non-collective (31)	8 ± 5	2.2 ± 0.5	$0.8\,(-0.25, +0.15)$

Table 5.1: Summary of plasma parameters comparing results from hydrocode simulations, collective scattering, and non-collective scattering experiments. For the collective case, fits using the homogeneous theory as well as the inhomogeneous expansion are included.

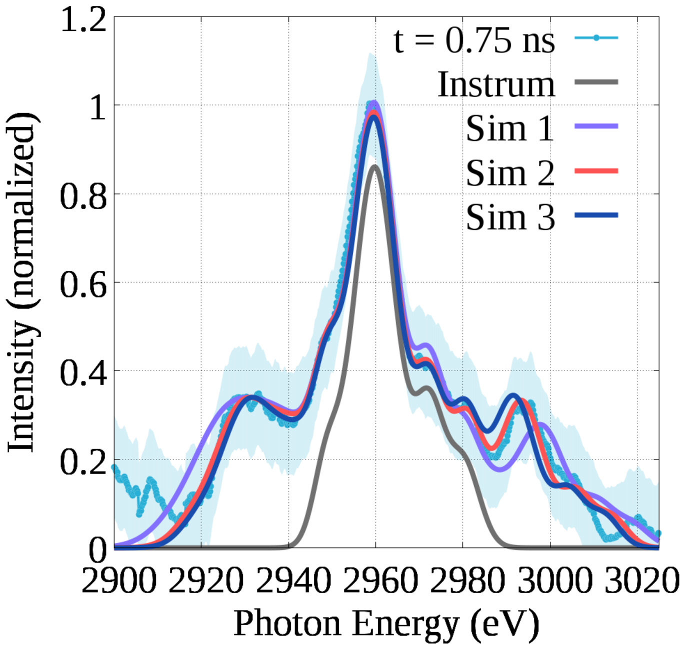

Figure 5.8: Inhomogenous simulation fits to measured spectra, obtaining sensitivity to temperature, density, and gradient scale length. *Teal*: Data from GTS strip 4 at $t = 0.75 - 1.00$ ns after the spectrometer starts acquiring data. The data has been smoothed and the linear continuum has been removed. The shaded region represents the standard deviation of the unsmoothed data. *Instrum*: This is the multi-Gaussian instrument function obtained from fitting the spectral calibration shot and elastic peak on strip 4. The elastic peak is not implemented in these simulations; the downshifted peaks of the simulations are normalized to the downshifted peak of the measured spectra. *Sim 1, purple*: $n_e = 5.0 \times 10^{23}$ cm^{-3}, $T_e = 20\,\mathrm{eV}$, $Z = 1.0$ and $\Lambda = 1.2\,\mathrm{nm}$. *Sim 2, red*: $n_e = 4.3 \times 10^{23}\,\mathrm{cm}^{-3}$, $T_e = 12\,\mathrm{eV}$, $Z = 1.0$ and $\Lambda = 1.33\,\mathrm{nm}$. *Sim 3, black*: $n_e = 4.0 \times 10^{23}\,\mathrm{cm}^{-3}$, $T_e = 10\,\mathrm{eV}$, $Z = 1.0$ and $\Lambda = 2.0\,\mathrm{nm}$. All simulations are done with the RPA model.

shock itself and not the material which has already passed through the shock front, is determined by viscous effects leading to a scale length on the order of mean free path $\Lambda \sim \lambda_{mfp}$. The mean free path is a function of temperature and density as seen in Eq. 1.19 in chapter 1. Plugging in the values for temperature and density obtained from the inhomogeneous simulation fits we get $\lambda_{mfp} \sim 0.4\,\mathrm{nm}$ which is consistent with the fitted gradient scale length.

If we are indeed measuring x-rays which were primarily scattered by the shock front this brings up an important concern: why would such a thin region with so few scatter sites as compared to the shocked material, have such a large influence on the spectra? It was already mentioned previously that the DRACO simulations show a region of shocked plasma $70\,\mu$m wide, which is much larger than the shock thickness. If we were to apply the summation method described in Eq. 3.9 in chapter 3, the volume of the shocked region would overwhelm any signal from the gradient region, as its volume is $\sim 10^5$ times larger.

If we are to believe that the plasmon signal is real then there must be some enhancement causing photons to predominantly scatter off the shock front. It is possible that as the scale length of the gradient approaches the wavelength of the probe beam, the shock front acts like the surface of a crystal where most scattering occurs at the sharp interface defined by the surface of the solid.

Another line of investigation, also relying on the sharpness of the shock gradient, is the quantum hall effect of light (144). It has been shown that for strong gradients of refractive index, photons can be deflected perpendicular to the gradient by a distance many times longer than the thickness of a crystal lattice.

5.5 Conclusions on XRTS

I have presented how the inhomogeneous expansion to XRTS may be applied to analysis of spectra from WDM experiments where there is a clear violation of detailed balance. The inhomogeneous spectral fits gave us additional information on the structure of the shock in the form of the scale length of the gradient Λ. The scale length obtained from the fits was compared to the shock thickness from mean-free path considerations. This check showed that the shock thickness can indeed be obtained from inhomogeneous XRTS theory, and provided further justification for using this expansion by demonstrating consistency with other physical theories. As for the experimental platform itself, there is significant room for improvement before consistent measurements can be provided for testing EOS models. Among the larger concerns, is that the signal to noise ratio for the measured plasmons was lower than desired, to the point that most shots and XRFC strips did not contain readily apparent plasmons. To this end we began investigating alternative backlighter geometries in the hopes of increasing x-ray conversion efficiency. This work is ongoing, and will not be discussed here, but preliminary results suggest a 2× increase in conversion efficiency, which can be of great benefit to future experiments.

Further improvements in shot day efficiency can be made by investigating the cause of failure in the filling and cryogenic cooling of deuterium in the copper cell. It was found in the September 2013 shots that substantial amounts of D_2 had leaked during the filling and cooling process such that two of the targets were unusable. Increasing pressure from 20 psi to 25 psi provided a temporary fix, and future procedures could benefit from vacuuming the target chamber and cooling the target simultaneously to limit the leak rate.

Finally, a major question remains open, with respect to how the shock front can have a significant effect on the scatter spectrum when it is volumetrically negligible as compared to the bulk, shocked material. Future investigations into this question will likely center around other geometric optical effects (that is, in addition to the violation of detailed balance in XRTS spectra) that occur in inhomogeneous media which could lead to enhanced scattering from a sharp interface.

6

Langmuir Probes

> *If Edison had a needle to find in a haystack, he would proceed at once with the diligence of the bee to examine straw after straw until he found the object of his search. I was a sorry witness of such doings, knowing that a little theory and calculation would have saved him ninety per cent of his labor.*
>
> —Nikola Tesla, *New York Times (19 October 1931)*

6.1 Introduction

Langmuir probes have been used in diagnosing the temperature, density and electric potential of plasmas for many decades. Their versatility and simplicity has led to their ubiquity in studying various phenomena including space plasmas, plasma deposition with commercial applications, tokamaks, and, more recently, laboratory astrophysics with supersonic flows (36, 37, 38, 39, 40, 41).

The classical example of a Langmuir probe consists of a single conductive surface exposed to a stationary plasma near thermodynamic equilibrium. A voltage is applied to the probe relative to ground and the current resulting from the interaction with the plasma via collection of charged particles is measured across a resistor. By varying the voltage one obtains an I-V curve from which the plasma parameters may be deduced; see Figure 6.2 for an example of an I-V curve. The temporal resolution of this technique is limited by how quickly the voltage source can be swept. To get around this limitation, multi-tipped probes, where each tip is set at a different bias using a simple DC source, were developed (33). These probes allow for the measurement of temporally-resolved current at a fixed bias and may therefore measure the variation of plasma parameters over time.

In the following sections we demonstrate the design of a probe with high temporal resolution in a floating triple probe configuration in the current-mode which allows us to directly probe the state of shocked, flowing plasma. Constructing such a probe can be beneficial for diagnosing different kinds of fast, localized phenomena which vary shot to shot. One important example, in the context of laboratory astrophysics, is turbulence, which is difficult to probe using optical methods due to a lack of temporal resolution as well as a lack of spatial resolution along the optical axis for any single shot.

We will begin this chapter with an overview of Langmuir probe theory to motivate the requirements in designing a probe suitable for measuring plasmas up to $n_e = 1 \times 10^{18}\,\mathrm{cm}^{-3}$ and $T_e = 10\,\mathrm{eV}$ with nanosecond resolution. Design and characterization of the probe will be discussed in this chapter and experiments which put our new probe to the test by comparing plasma parameters with those obtained by inteferometry and spectroscopy will be discussed in the following two chapters.

6.2 Theory

A Langmuir probe consists of wires (or a single wire), also referred to as probe tips, that are biased against each other (or chamber ground). When a plasma interacts with the tips of the wires it effectively closes the circuit and generates a current whose value is dependent on the temperature, density, and electric potential of the plasma. There are two modes in which an LP can operate: voltage-mode and current-mode. In the voltage-mode two wires are biased against each other with fixed voltages, for which current is measured and the third wire is left floating by a large impedance resistor connecting it to the other two wires. The voltage of the third wire is measured and, along with the current measured between the first two wires, is fed into the LP theory equations to solve for temperature, density, and plasma potential. The high impedance resistor is a source of noise

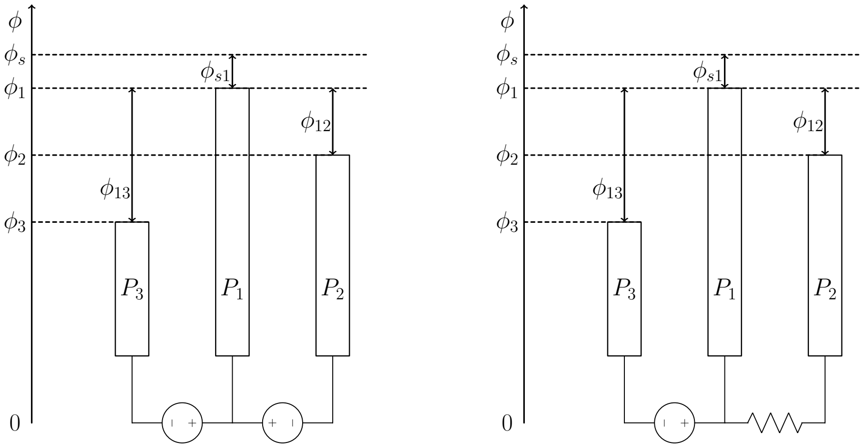

Figure 6.1: *Left:* Current-mode triple Langmuir probe, where a fixed DC bias is placed between P_1 and P_2. Here, the measurement of interest is the current flowing into each tip. *Right:* Voltage-mode triple Langmuir probe, where a high-impedance resistor is used between P_1 and P_2 to measure the voltage.

in pulsed plasmas, and is thus removed in the current-mode design and replaced with another voltage source.

In the current-mode, all three wires are biased against each other and there are no large resistors. The current flowing through each wire is measured and then fed into the LP theory equations. A schematic of these two operating modes can be seen in Figure 6.1. Our design is based on the current-mode probe; the development of the theory will be based on this (35, 36).

Using the convention that electron current to a probe is positive and ion current is negative, assuming probe bias relative to space (plasma) potential $\phi_p \leq \phi_s$, the total current to any probe tip is the sum of electron and ion currents

$$I_{probe} = I_{electron} - I_{ion} \tag{6.1}$$

The general formula for the current due to a particular species is

$$I = A_s e n_s u_s \zeta \tag{6.2}$$

where A_s is the surface area of the sheath, n_s is the density at the sheath edge, u_s is the velocity at the sheath edge and ζ is the proportion of particles crossing the sheath which are collected by the probe.

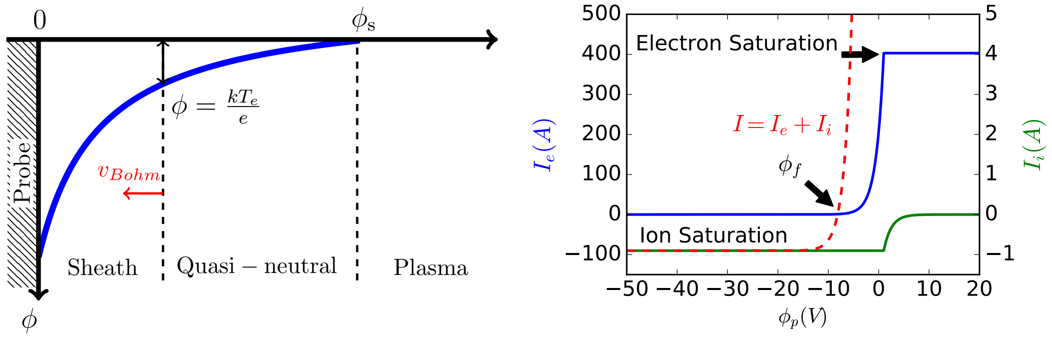

Figure 6.2: *Left:* Diagram showing the exponential decay of the electric potential and the demarcation of sheath, quasi-neutral, and plasma regions. *Right:* I-V curves, assuming collisionless regime, showing electron current (blue), ion current (green), and total current (red). The total current is plotted on the same axis as the ion current. All plots are done for $T_e = 1.5$ eV, $n_e = 1.0 \times 10^{17}$ cm^{-3}, and $\phi_s = 1$ V.

The selection of the sheath area, particle velocity, density, and proportion of particles reaching the probe depends on which physical processes are important to the system. The importance of these processes can be assessed by the appropriate nondimensional parameters. What follows is a brief overview of different probe theories which may be applicable to to the analysis of laser produced plasmas. More detailed reviews may be found in Demidov (2002) and Electric Probes in Stationary and Flowing Plasmas by Paul M. Chung, Lawrence Talbot, and Kenell J. Touryan (20, 145).

The Knudsen number, $\mathrm{Kn} = \frac{\lambda_{\mathrm{mfp}}}{\mathrm{r}}$ as given by Eq. 1.21, is used to check for the influence of collisions on the system. There are two important Knudsen numbers in Langmuir probe theory: one for the bulk plasma (quasi-neutral region) and one for the sheath region; these regions are depicted in Figure 6.2. To check for collisions in the bulk of the plasma the radius of the probe tip is used as the characteristic length scale. For collisions in the sheath, the thickness of the sheath is used as the characteristic length scale. When both Knudsen numbers are much greater than unity, collisionless probe theories may be applied to the analysis of probe currents. If collisions are important in both the sheath and bulk of the plasma, continuum theories are used. If collisions are important in one region and not the other, then hybrid theories are used. Generally speaking, the influence of collisions is to reduce the current to the probe by a factor proportional to the diffusion coefficient. As the particles are attracted by the probe they collide with and are deflected by their neighbors forcing them to take a longer path. On the macroscopic scale this is described by a forced diffusion model (146, 147). The transition regime is somewhat trickier as diffusion models are not valid throughout the entire plasma, typically breaking down in the sheath region near the probe. In this regime, it is important to account for the inertia of the ions, possible orbital motions, and shifts in the distribution function due to collisions with the probe tips, whereas in the collisionless regime one simply addresses the inertia and motion of the ions (146).

The ratio of Larmor radius to probe radius, $\frac{r_g}{r_p}$, is used to assess whether the plasma is magnetized. The Larmor radius, also known as the gyroradius, is given by:

$$r_g = \frac{mv_\perp}{|q|\,B} \tag{6.3}$$

where m is the particle mass, $v_\perp$ is the component of velocity perpendicular to the magnetic field, q is the particle charge, and B is the magnetic field. In a plasma, one typically has different species with different Larmor radii so it is possible for one species to be magnetized and the other to be unmagnetized. The influence of magnetic fields is to force the collected current to follow along field lines (flux tubes). If the current close to the probe, along this line is depleted then the probe must either work against magnetic diffusion across field lines to collect more current or the sheath must be extended further along the field line to envelope more particles (148).

Another important parameter is the size of the sheath compared to the radius of the probe, $\frac{r_p}{\lambda_D}$. In the thin sheath regime one can set the collection area to be the surface area of the probe, $A_s = A_p$. The sheath thickness is also important for determining the form of the ion current.

6.2.1 Collisionless Thick sheath

For $5 \leq \frac{r_p}{\lambda_D} \leq 100$ the probe is in the Laframboise regime (36). Here it is assumed that the bulk of the plasma is collisionless $\mathrm{Kn} = \lambda_{mfp}/r_p \gg 1$ and that the plasma sheath around each probe tip must be collisionless as well, $d_s/\lambda_{mfp} \ll 1$ where d_s is the sheath thickness:

$$d_s = \left(\frac{\sqrt{2}}{3}\right) \lambda_D \left(\frac{2e\phi_{ps}}{kT_e}\right)^{\frac{3}{4}} \tag{6.4}$$

where λ_{De} is the Debye length, $\phi_{ps} = \phi_p - \phi_s$ is the difference between the probe potential and the space (plasma) potential. In addition to the collisionless criterion, the plasma sheaths may not interact, meaning $s > d_s$ where s is the interprobe spacing.

For a plasma composed of electrons and single ion species we assume a drifting Maxwellian distribution

$$f_\alpha(\vec{r}, \vec{v}, t) = n_\alpha(\vec{r}, t) \left(\frac{m_\alpha}{2\pi kT_\alpha}\right)^{\frac{3}{2}} \exp\left[-\frac{m_\alpha \left(\vec{v_\alpha} - \vec{U_\alpha}\right)^2}{2kT_\alpha}\right] \tag{6.5}$$

where the α index indicates the species (either ions or electrons), m_α is the mass, $\vec{v_\alpha}$ is the velocity, $n_\alpha(\vec{r}, t)$ is the number density, $\vec{U_\alpha}(\vec{r}, t) = \langle \vec{v_\alpha} \rangle$ is the average/drift velocity, and T_α is the temperature.

The electron current to a probe, $I_{||e}$, is due to random electron current, taken as thermal velocity,

$$u_s = \left(\frac{kT_e}{2\pi m_e}\right)^{\frac{1}{2}} \tag{6.6}$$

and an exponential decay term which accounts for the electrostatic energy of the probe being less than the thermal energy of the electrons at the tail of the Maxwellian distrubtion, allowing for electrons to escape the potential well created by the probe.

$$\zeta = \exp\left[-\frac{e\left(\phi_s - \phi_p\right)}{kT_e}\right] \tag{6.7}$$

Bringing these terms all together gives the electron current as collected by a probe oriented parallel to any flow.

$$I_{||e} = A_{||} J_{e0} \exp\left[-\frac{e(\phi_s - \phi_p)}{kT_e}\right] = A_{||} J_{e0} \exp\left[-\frac{e(\phi_{sp})}{kT_e}\right] \tag{6.8a}$$

where

$$J_{e0} = en_e \left(\frac{kT_e}{2\pi m_e}\right)^{\frac{1}{2}} \tag{6.8b}$$

is the random electron current density, and $A_{||}$ is the exposed probe surface area.

For the collisionless thick sheath, the ion current is a function of the random thermal ion current density along with correction parameters accounting for the sheath thickness

$$I_{||i} = A_{||} J_{i0} \left(\beta + |\chi_p|\right)^{\alpha} \tag{6.9}$$

where $J_{i0} = en_i \left(\frac{kT_e}{2\pi m_i}\right)^{\frac{1}{2}}$ is the random ion current, and the α, β parameters are given by:

$$\alpha = \frac{2.9}{\left[\ln\left(\frac{r_p}{\lambda_D}\right) + 2.3\right]} + 0.07\left(\frac{T_i}{Z_i T_e}\right)^{0.75} - 0.34 \tag{6.10a}$$

$$\beta = 1.5 + \left(\frac{T_i}{Z_i T_e}\right)\left\{0.85 + 0.135\left[\ln\left(\frac{r_p}{\lambda_D}\right)\right]^3\right\} \tag{6.10b}$$

Here χ_p is the nondimensional potential

$$\chi_p = \frac{e\left(\phi_p - \phi_s\right)}{kT_e} \tag{6.11}$$

6.2.2 Collisionless Thin sheath

For $\frac{r_p}{\lambda_D} \geq 100$, thin-sheath collisionless theory is applicable. The electron current is the same as that for the collisionless thin sheath regime where the thermal velocity of electrons is dominant.

The ion current is given by the simple Bohm expression:

$$I_{||i} = A_{||} en_e \sqrt{\frac{kT_e}{m_i}}\ \exp\left[-\frac{1}{2}\right] \tag{6.12}$$

In the thin-sheath regime the currents are given by (36):

$$I_1 = A_{||} J_{e0} \exp\left[-\frac{e\phi_{s1}}{kT_e}\right] - A_{||} e n_e \sqrt{\frac{kT_e}{m_i}} \exp^{-\frac{1}{2}} \tag{6.13a}$$

$$I_2 = A_{||} J_{e0} \exp\left[-\frac{e(\phi_{s1}+\phi_{12})}{kT_e}\right] - A_{||} e n_e \sqrt{\frac{kT_e}{m_i}} \exp^{-\frac{1}{2}} \tag{6.13b}$$

$$I_3 = A_{||} J_{e0} \exp\left[-\frac{e(\phi_{s1}+\phi_{13})}{kT_e}\right] - A_{||} e n_e \sqrt{\frac{kT_e}{m_i}} \exp^{-\frac{1}{2}} \tag{6.13c}$$

where $A_{||}$ is the collection area of the probe, for a cylindrical probe this is $A_{||} = 2\pi r l$ where r is the radius of the tip and l is the length. ϕ_{s1} is the potential difference between probe tip 1 and the spatial potential of the plasma $\phi_{s1} = \phi_s - \phi_1$. Similarly, $\phi_{12} = \phi_1 - \phi_2$ and $\phi_{13} = \phi_1 - \phi_3$. T_e is the electron temperature, n_e is the electron density, and m_i is the ion mass. J_{e0} is the random thermal electron current density:

$$J_{e0} = e n_e \left(\frac{kT_e}{2\pi m_e}\right)^{\frac{1}{2}} \tag{6.14}$$

where m_e is the mass of an electron.

The first term on the right-hand side of Eq. (6.13) is the electron current and the second term is the ion current. When the plasma is incident on the probe tips a Debye sheath develops around each tip to shield the electric fields from penetrating deep into the plasma. The magnitude of the electron current is dependent on thermal energy of the electrons as compared to the repulsive/attractive energy of the electric potential created by the probes, this is the non-dimensional potential χ_p. Assuming the electrons to be of Maxwellian distribution yields the exponential dependence on χ_p. The ion current, on the other hand, is a bit more complex since thermal current is unlikely to be significant for massive particles. Instead, it is assumed that exponentially small electric fields penetrate the Debye sheath and draw the ions over a distance $L \gg \lambda_{De}$. At the sheath edge, the ions have been accelerated to satisfy the Bohm velocity $v_{Bohm} = \sqrt{\frac{kT_e}{m_i}}$, where the electron temperature reflects the significance of the electrons in establishing the Debye sheath. It should be noted that the Bohm velocity is a minimum criterion and the ions may in fact exceed the Bohm velocity, but most theoretical descriptions of ion collection assume the minimum conditions (149). The various regions between plasma and probe are shown in Figure 6.2 along with an I-V curve depicting the dependence of electron and ion currents on the probe bias.

Given currents I_1, I_2, I_3 measured in an experiment, the functions ϕ_s, T_e, and n_e can be obtained by solving the set of equations 6.13 simultaneously at every point in time. This solving for the plasma parameters from the given currents is towards the end of the present chapter.

6.2.3 Continuum Regime

In the continuum regime, the bulk of the plasma is collisional $\mathrm{Kn} = \lambda_{mfp}/r_p \ll 1$ and the sheath around each probe tip must be collisional as well, $d_s/\lambda_{mfp} \gg 1$. In this case, the current to a cylindrical probe is given by

$$I_{\alpha,sat} = A_s e n_0 \frac{\mu_\alpha k_B \left(T_e + T_\alpha\right)}{r_s \ln\left(\pi L/4 r_s\right)} \tag{6.15}$$

where α is the particle species, r_s is the sheath radius, L is the length of the probe and

$$\mu_\alpha = \frac{eZD_\alpha}{kT_\alpha} = \frac{q}{m\nu} \tag{6.16}$$

is the particle mobility as given by Einstein's relation (a form of fluctuation-dissipation theorem for collisional diffusion). Where D is the diffusion coefficent, q is the electric charge, m is the particle mass, ν is the collision frequency (147).

6.2.4 Transition Regime

Thornton (1971) described a suitable method for interpolating between the collisionless and continuum regimes for estimating the current in the regime where $\mathrm{Kn} \sim 1$, also known as the transition regime (146).

In the collisionless regime, inertial effects act as an impedance to current flowing towards the probe. Similarly, in the continuum regime, collisions/diffusion act as an impedance. These two impedances can be added in series to obtain an interpolation for the transition regime where both collisions and inertial effects are important.

$$I_p = \frac{I_0 I_c}{I_0 + I_c} \tag{6.17}$$

where I_0 is the collisioness current and I_c is the continuum current as described in the prior sections.

6.3 Obtaining plasma parameters from current traces

The set of equations for the thin-sheath theory are composed of at least three current equations representing the current drawn by each tip and at least three unknowns: density, temperature, and plasma potential. In an experiment we measure the currents and must solve for the unknown parameters. Fortunately, the thin-sheath theory equations are simple to solve for using a combination of numerical and analytical techniques.

At every point in time the Langmuir probe should give us three currents, one for each tip. To obtain the time-resolved plasma parameters we simply apply the above equations at a particular point in time, solve for the plasma parameters, and do the same process for all other points in time. As far as the thin-sheath theory equations are concerned, the plasma parameters at any point in time are independent of the plasma parameters at any other point in time.

The process for solving the plasma parameters is as follows: (1) Input the currents to the left hand side of Eq. 6.18 and either graphically or numerically solve for the temperature on the right hand side for the given set biases.

$$\frac{I_1 - I_2}{I_1 - I_3} = \frac{1 - \exp\left(-\frac{e\phi_{12}}{kT_e}\right)}{1 - \exp\left(-\frac{e\phi_{13}}{kT_e}\right)} \tag{6.18}$$

(2) Use the value of T_e obtained in the previous step and solve for n_e using

Eqs. 6.19a and 6.19b.

$$n_e = \frac{J_i}{\exp\left(-\frac{1}{2}\right) e\sqrt{\frac{kT_e}{m_i}}} \tag{6.19a}$$

$$J_i = \frac{1}{A_{||}} \frac{I_3 - I_2 \exp\left[-\frac{e(\phi_{13}-\phi_{12})}{kT_e}\right]}{\exp\left[-\frac{e(\phi_{13}-\phi_{12})}{kT_e}\right] - 1} \tag{6.19b}$$

where J_i is the ion current density.

(3) Finally, use T_e and J_i to solve for ϕ_{s1} in Eq. 6.20.

$$\phi_{s1} = \frac{-kT_e}{e} \ln\left[\frac{I_1 + A_{||}J_i}{A_{||}J_{e0}}\right] \tag{6.20}$$

The above equations should yield exact solutions so there is no need to solve for the plasma parameters iteratively. We also see that the electron temperature is sensitive to the ratio of the currents, whereas the electron density is sensitive to the magnitude of the currents.

There is a further issue of accounting for the current due to the flow velocity of the ions. The thin-sheath theory equations are only valid in a relatively stationary flow where ion collection is dominated by the Bohm velocity.

$$v_{Bohm} = \sqrt{\frac{kT_e}{m_i}} \tag{6.21}$$

When $v_{flow} \geq v_{Bohm}$ we find a way to compensate for the flow term. We choose to compensate for the flow term by subtracting it from the measured currents and using the resultant currents for analysis using the thin-sheath theory equations, as was suggested by Koopman *et al.* with respect to the I-V characteristic (150, 151).

$$I_{2,effective} = I_{2,measured} + I_{flow} \tag{6.22a}$$

$$I_{flow} = A_{\perp} Z e n_e v_{flow} \tag{6.22b}$$

where Z is the ionization level of the plasma, $A_{\perp}$ is the surface area oriented perpendicular to the plasma flow and v_{flow} is the flow velocity of the ions. It is important to note that in 6.22b, the v_{flow} term is added to the measured current

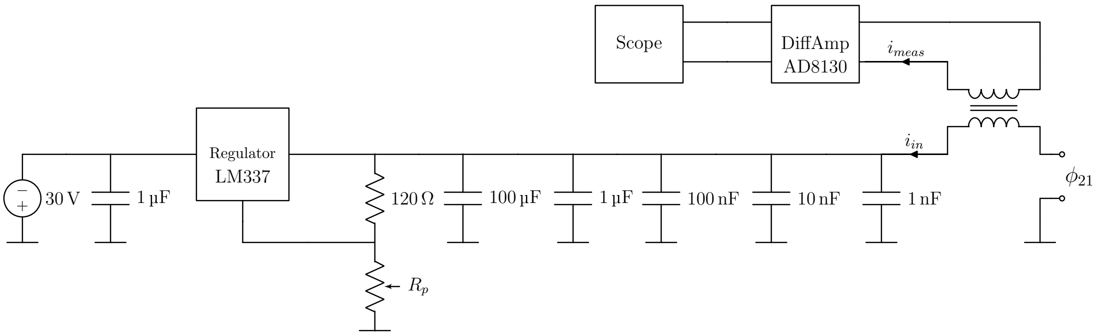

Figure 6.3: Schematic of one tip of the Langmuir probe circuit. Mirroring the circuit, joining the references and adding a transformer for the reference line (tip 1) yields the full circuit. An LM337 voltage regulator is powered by a DC supply, seen on the far left. The bias on the regulator is set by altering the resistance of the potentiometer, R_p. An AD8130 differential amplifier is used to buffer the signal on the oscilloscope side of the transformer, as well as remove external electrical noise common to both wires of the transmission line. All grounds marked in the diagram are in reference to tip 1, which is positively biased, such that the probe is floating with the plasma.

because we defined ion current as negative. This should have the effect of reducing the magnitude of the ion current.

6.4 Probe design and construction

6.4.1 Design considerations

In order to approach GHz resolution the probe design must consider possible high frequency circuit effects. If the wavelength of the measured signal is longer than the circuit length, then there will be significant variations in voltage at different positions along the circuit. If this is the case, then the circuit may no longer be treated using classical circuit or even transmission-line theory, but rather a full analysis using Maxwell's equations is required. Therefore, in order to obtain high temporal resolution, we must make sure that the path traveled by the collected current is short, such that high frequency signals may be collected and easily interpreted (152).

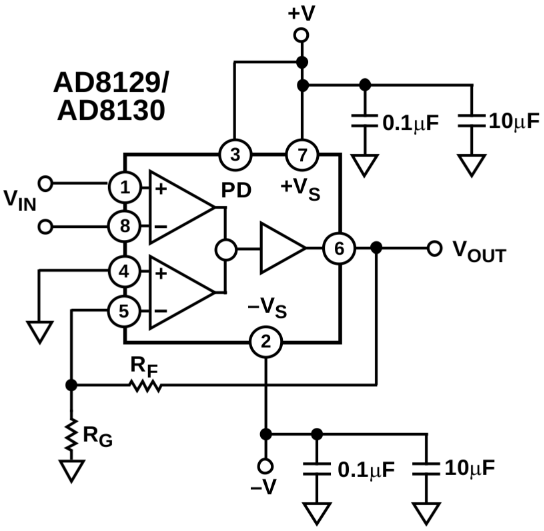

Figure 6.4: Detailed circuit of the AD8130 differential amplifier in a standard gain mode. The resistances for buffering the probe signal are $R_F = 8.25\,\text{k}\Omega$ and $R_G = 2\,\text{k}\Omega$. The gain is determined by $V_{OUT} = V_{IN}\,(1 + R_F/R_G)$. This results in a gain of ~ 2.5 across a standard $50\,\Omega$ impedance and a gain of ~ 5 across a high impedance (typically $1\,\text{M}\Omega$ for most oscilloscopes). The operational amplifier has a bandwidth of 270 MHz and may limit future improvements to temporal resolution.

At GHz frequency, the wavelength of an electromagnetic signal is ~ 30 cm. This poses some problems, since in a typical laboratory setup, at least a meter of cable is required to connect the diagnostic in the vacuum chamber to the oscilloscope, where the signal is being recorded. To work around this issue, we will split the circuit into two physically separated components which are joined by a high bandwidth transformer. We shall distinguish between these two galvanically-isolated parts of the circuit by referring to the portion of the circuit exposed to the plasma as the Langmuir circuit and the other half as the measurement or oscilloscope circuit. The Langmuir circuit will be kept short, such that the measured signal is considered uniform across the circuit length. We may therefore use standard Langmuir probe theories to analyze the collected currents. A schematic of the circuits is shown in Fig. 6.3, where the top loop which feeds through the transformer is the oscilloscope circuit and the entire bottom half of the diagram is the Langmuir circuit.

The upper limit of the measurable density is constrained by the maximum current which the probe may draw before being damaged. The maximum current is set by the circuit elements used in constructing the probe. Since we are attempting to keep a small form factor for the probe to increase the temporal resolution, the circuit elements must be small and may not dissipate as much power. The probe described in Figure 6.3 can withstand up to 18 V and 1 A. The latter constraint translates to approximately $n_e \sim 1 \times 10^{17}\ \mathrm{cm}^{-3}$, obtained from the ion saturation current for low temperature plasmas.

The probe biases are maintained by two variable DC voltage regulators. A series of bypass capacitors are used to shunt currents which are too quick for the voltage regulator as shown in Fig. 6.3. The regulators have a slow response time and if the bypass capacitors were not present then the bias at the probe tips would fluctuate due to large currents passing through the circuit. An approximation of the circuit was designed in LTSpice IV to test for stability of the bias. The simulations showed that the combination of bypass capacitor and voltage regulator keep the bias stable to within 0.05 V, for a driving current of 1 A as shown in Figure 6.10 in a latter section. Though such high currents should not be sustained for extended periods of time for risk of burning out the circuit.

The output of the measurement circuit is fed into a differential amplifier which reduces electronic noise by common-mode rejection of externally sourced electric signals incident on the circuit. The differential amplifier also helps to buffer the signal as it traverses long distances from the experimental chamber to the oscilloscope. A schematic of the differential amplifier is shown in Figure 6.4

The majority of the probe is housed in a tungsten rod with a conical cap. An alumina rod is fed through the cone, to protect the wires extending out from the tungsten body which connect to the probe tip assembly. The probe tip assembly consists of 3 tungsten tips, with dimensions $r_p = 125\mu$m and $l_p = 1.4$mm, soldered to a 4-pin LEMO connector encased in a boron nitride rod. The tungsten wires are partially plated with copper to allow for easy soldering to the LEMO connector. The entire tip assembly connects to a corresponding LEMO connector seated in the alumina rod, allowing for quick exchange of the tip in case it is damaged or requires cleaning from deposited materials, without needing to remove the entire probe during an experiment. The use of tungsten, alumina, and boron nitride help to insulate the probe from damage due to thermal loading (33). A mu metal casing may be added to dampen any magnetic fields. The inside of the constructed probe can be seen in Figure 6.5.

6.4.2 Testing Ferrites

Transformers separating the Langmuir and measurement circuits were hand wound, by the author, around high bandwidth K14 Nickel-Zinc soft ferrite cores provided by Kaschke components. Ferrites are used in a broad range of applications, including high frequency signal filtering. Therefore, it is important to test that the characteristics of the ferrites are suitable to our application. Here we are mainly concerned with bandwidth, though signal droop and hysteresis effects may become important for longer signal acquisition and repetitive cycling as occurs in RF generated plasmas (154).

The bandwidth of the ferrites was tested by creating a small cavity out of copper sheet metal. The cavity was connected to a network analyzer to obtain the real and imaginary components of the magnetic permeability in the cavity. Two measurements were taken, one with the empty cavity (with air), and one

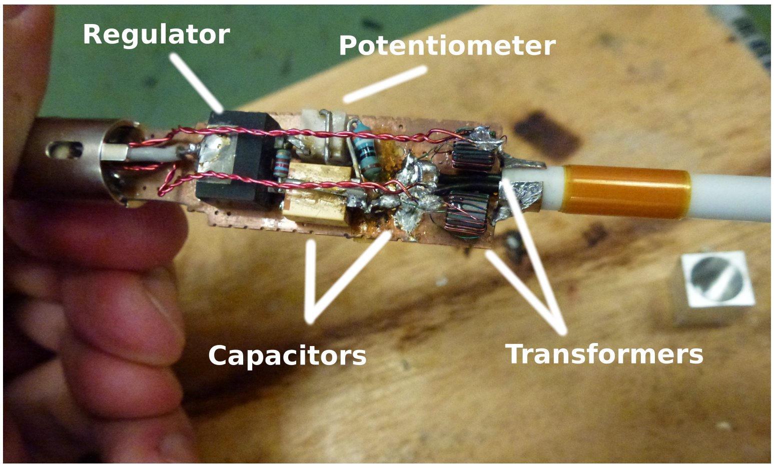

Figure 6.5: Picture of internal circuitry of the constructed probe. Voltage regulator, potentiometer, bypass capacitors, and hand-wound transformers are noted. The 18-pin LEMO sits on the far left and the alumina tube protecting the wires towards the tip of the probe can be seen on the far right. The red twisted-pairs carry the signal from the transformers to the oscilloscope. The copper plate is directly connected to tip 1 and acts as a reference ground plane which is isolated from any external grounds.

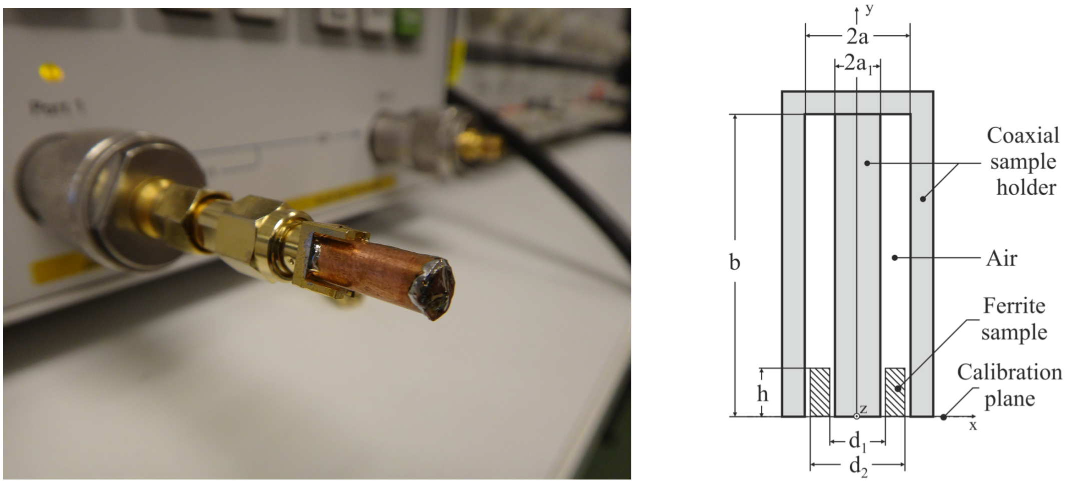

Figure 6.6: *Left:* Picture of ferrite test rig with copper cavity mounted to VNA. *Right:* Cross-sectional schematic of the copper cavity with ferrite (153).

with the ferrite inside. The empty cavity measurement yields the upper limit for which the permeability measurements are valid, due to the impedance of the cavity. This upper limit was $\sim 1\,\mathrm{GHz}$, well above the measured bandwidth of the ferrite, which was $\sim 300\,\mathrm{MHz}$.

Adequate modeling of the ferrite requires knowledge of the frequency dependent, nonlinear, complex permeability:

$$\mu_s = \mu_s^{'} - j\mu_s^{''} \tag{6.23}$$

where the real component, $\mu_s^{'}$, represents inductance of the ferrite and the imaginary component, $\mu_s^{''}$, represents losses (154).

A shorted coper cavity was rigged to a vector network analyzer (VNA) in order to measure the complex permeability, see Figure 6.6. The VNA sends an input signal which is modulated by the inductive effects of the cavity (magnetic permeability). By measuring the magnitude and phase of the S_{11} reflections of the cavity with the ferrite and without the ferrite, in air, we obtain the permeability versus frequency in a range below the cavity's resonant frequency by using (153):

$$\widetilde{Z}_{in} = Z_0 \frac{1+S_{11}}{1-S_{11}} \tag{6.24}$$

$$\widetilde{\mu}_r = 1 + \widetilde{\chi} = 1 + \frac{\left(\widetilde{Z} - \widetilde{Z}_{air}\right)}{jh \cdot \mu_0 \cdot f \cdot \ln\left(\frac{d_2}{d_1}\right)} \tag{6.25}$$

where $Z_0 = 50\,\Omega$ is the impedance of the test port, S_{11} is the complex scatter parameter (for reflections), and $\widetilde{Z}_{in}$ is the impedance of the cavity (with or without ferrite). $\widetilde{Z}_{air}$ is the impedance of the cavity without the ferrite, $\widetilde{Z}$ is the impedance of the cavity with the ferrite, $j = \sqrt{-1}$ is the complex number, h is the height of the ferrite, d_2 is the outer diameter of the ferrite, d_1 is the inner diameter of the ferrite and f is the frequency of the input signal. $\widetilde{\mu}_r$ is then the frequency dependent complex permeability.

The upper limit of the ferrite bandwidth occurs where the imaginary component of the permeability is on par with the real component. This is seen near $\sim 300\,\mathrm{MHz}$ in Figure 6.7. Here, dissipative effects and losses in signal due to the ferrite become important and the ferrite begins to act as a filter in this regime.

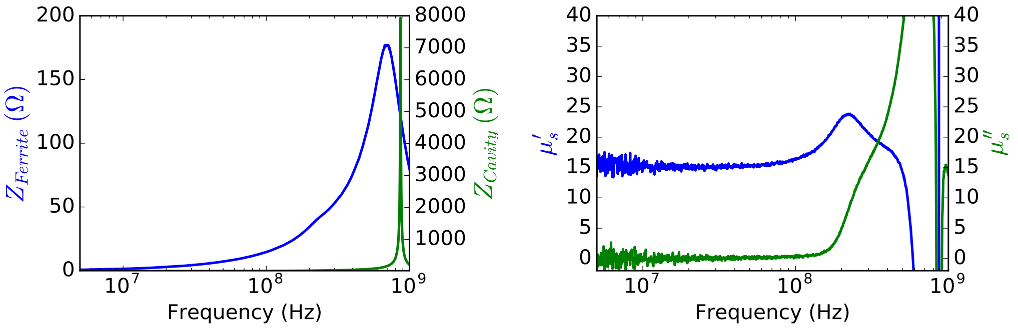

Figure 6.7: *Left:* Impedance of ferrite and cavity obtained from network analyzer. *Right:* Resultant real and imaginary components of magnetic permeability for ferrite showing a bandwidth of ∼ 300 MHz. At low frequency, errors due to low impedance are seen, and at high frequency the cavity impedance dominates; these demarcate the limits of the technique.

The ferrites were then tested as transformers by wrapping a twin copper wire with varying number of windings. The two wires were kept close together on each winding around the transformer to aid in the high frequency coupling between the wires. Since both wires were wound the same number of times the current ratio through the transformer is 1 : 1. The transformer was tested on the network analyzer by driving a signal along one wire and analyzing the response from the other wire. It was found that 20 windings yielded a suitably flat, high signal, bandwidth up to ∼ 200 MHz. This is consistent with the temporal resolution of the full probe setup, shown in the following section, which suggests that the limiting factor in temporal resolution is the transformer.

6.4.3 Temporal resolution of probe

The frequency response, and thus the temporal resolution, of the Langmuir probe was obtained by testing pairs of inputs at the probe tips against the resulting output, where an oscilloscope would be connected, using a network analyzer. This is shown schematically in Fig. 6.8. The network analyzer treats the circuit under testing as a two-port network and measures the response of the network. In this case, we use the scattering or S-parameters given by the network analyzer.

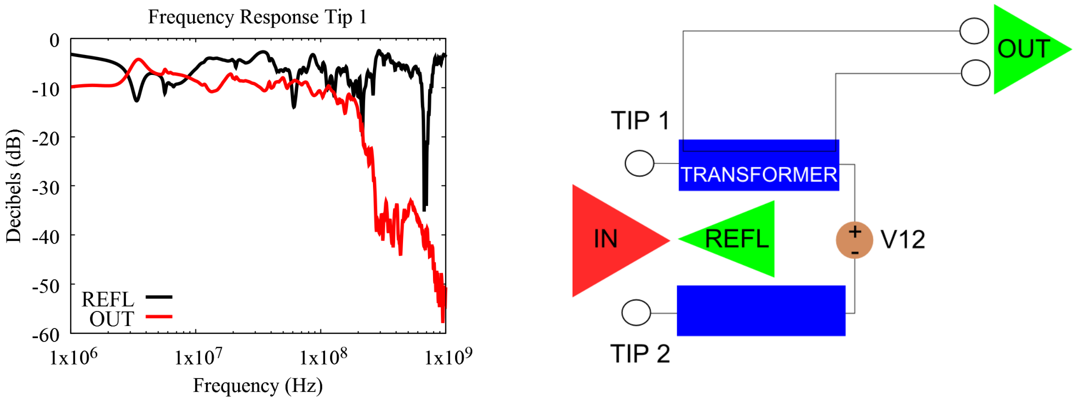

Figure 6.8: *Left:* Frequency response of Langmuir probe measured with network analyzer connected across tips 1 and 2. The measured bandwidth is 200MHz. *Right:* Schematic of Langmuir probe and network analyzer for measuring bandwidth. The network analysis is done without any bias between the probe tips, otherwise one risks damaging the network analyzer and possibly distorting the measurement.

We are particularly interested in the S_{11}, forward reflection coefficient, and the S_{21} forward transmission coefficient as they tell us whether the small, galvanically-isolated front-end of our Langmuir circuit is suffering from any losses and whether the transformers are transmitting sufficient signal from the Langmuir circuit to the measurement circuit. Furthermore, we may test for electronic noise due to cross-talk by connecting the network analyzer to a pair of output channels which are supposed to be isolated from the inputs. In this case, the S_{21} parameter is a measure of the cross-talk between the ports. Fig. 6.8 shows the S_{11} and S_{21} scatter parameters obtained by connecting the input of the network analyzer across tips 1 and 2 and reading the output from their respective channels. We see that S_{21} has strong and relatively flat response up to 200 MHz. Figure 6.9 shows a similar chart for the same inputs, but the output is connected to the output from tips 1 and 3. We see that the cross-talk is significantly lower than the throughput signal, at least 20 dB, up to the bandwidth limit of the probe. This means that electronic noise due to cross-talk is negligible and we don't need to account for it in our calibration.

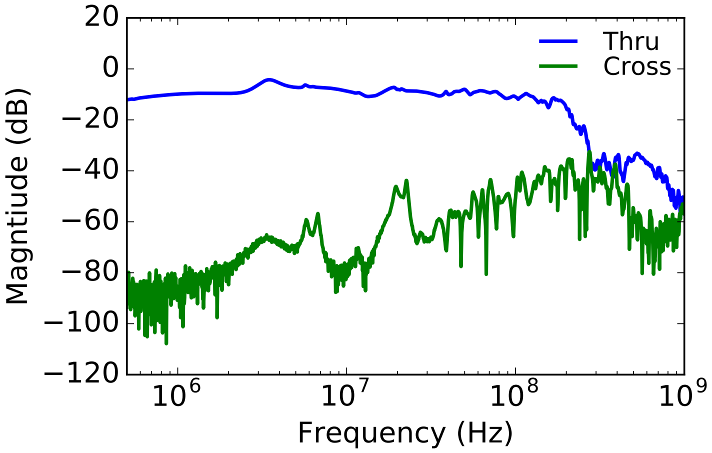

Figure 6.9: *Blue:* Signal throughput from one tip, through the entire circuit up to the oscilloscope as obtained by network analyzer. *Green:* Crosstalk picked up from sending input signal along one tip, but reading from a different channel on the oscilloscope end. Crosstalk remains well below throughput signal until throughput signal decays due to bandwidth limitations at ~ 200 MHz.

6.4.4 LTSpice simulation

All circuit components in the probe have some impedance which can shift the probe bias when met with a large current. We test the stability of the probe bias against such large currents by using a transient circuit simulation implemented in LTSpice IV. The circuit under simulation has already been shown in Figure 6.3. A model of the LM337K voltage regulator was obtained from the Linear Technologies website. The circuit was tested under a 1 A square current pulse with pulse width of 1 μs. The probe tip bias was set at -20 V. The simulation showed that during this time the voltage regulator and bypass (shunt) capacitors were able to maintain the bias to within 0.1 V of the set value, see Figure 6.10. Therefore, the bias which is set and measured prior to each shot, can be assumed to be constant throughout the shot.

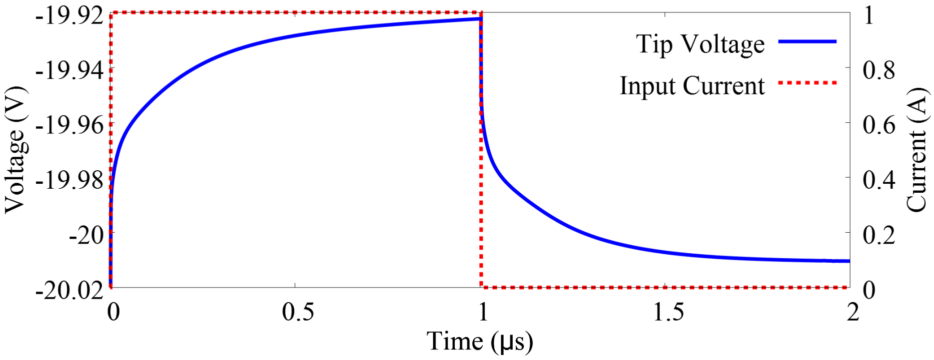

Figure 6.10: Simulation of circuit voltage stability with LM337 voltage regulator and bypass capacitors conducted using LTSpice IV. In red, is shown the input current pulse of 1 A over 1 μs and in blue is the voltage of the probe tip. The probe voltage was initially fixed at 20 V, the maximum operating bias of the probe, and we see that the regulator and capacitors maintain this bias to within 0.1 V.

7

Experimental setup for testing Langmuir Probe

> *I have also a paper afloat, with an electromagnetic theory of light, which, till I am convinced to the contrary, I hold to be great guns.*
>
> —James Clerk Maxwell, *Letter to C. H. Cay, (Jan 5, 1865)*

7.1 Introduction

Experiments using the newly constructed Langmuir probe were conducted in the Gregori group's lab at the University of Oxford. Experiments consisted of carbon rod targets in a vacuum chamber filled with Argon to a pressure of ~ 1 mbar. The target was ablated by a 2ω (532 nm) laser, driving a shock radially outward and into the Argon gas fill. A suite of diagnostics were used to measure the properties of the shock, including: interferometry, emission spectroscopy, three-axis B-dot probes, and Langmuir probes. The aim of the experiments was twofold: first, to adequately characterize the laser-produced plasma shock using standard diagnostic methods; second, to compare the accuracy of the Langmuir probe to the other diagnostics at assessing the plasma parameters to demonstrate that it is a viable tool for characterizing laser produced plasmas.

The triggering of the lasers and diagnostics is initiated by manually flipping a switch which sends a TTL pulse to the Litron laser systems. The Q-switch in the

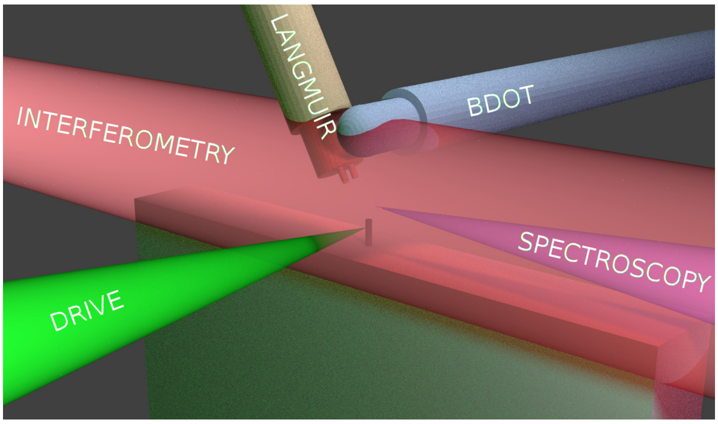

Figure 7.1: A 3D schematic of the experimental setup is shown. The green drive beam is focused onto a carbon rod driving a shock into the Argon gas fill. Interferometry (red) and emission spectroscopy (purple) lines are oriented with field of view orthogonal to the drive laser. Emission spectroscopy is spatially resolved vertically above the target. The B-dot (blue) is positioned vertically above the target while the Langmuir probe (tan) is at an off-angle with the tips pointed directly at the target such that the shock will expand parallel along the length of the tips.

Litron activates, sending out a laser pulse for ablating the target. It also sends a simultaneous electric signal to two different timing boxes. One box sets the delay between the Litron and the Hidra laser system (used for interferometry), giving us the capacity to take interferograms at different times in the plasma evolution. The second box simply splits the signal and sends it to the spectrometer CCD, interferometry CCD, and two oscilloscopes measuring B-dot and Langmuir probe signals, respectively. Software controls the internal delay and gating of the spectrometer and the software programs controlling the interferometer CCD and oscilloscopes were set to acquire data for the duration of the plasma evolution and did not require any further gating.

7.2 Experimental layout

Experiments were conducted in a cylindrical vacuum chamber with 4 major ports along two lines of sight. Carbon rod targets measuring 0.5mm thick were mounted to an aluminum block with a thin layer of Blu-tack and attached to a 3-axis vacuum-safe motor mount within the chamber. The motorized stage allowed for multiple targets to be mounted and aligned, increasing the number of shots per vacuum cycle. Typically, 5 targets were mounted at once with a spacing of $\sim 3\,\mathrm{mm}$.

The Litron laser used to drive the target and shocked plasma, deposits $\sim 2.5\,\mathrm{J}$ of energy at 532 nm with a pulse width of 10 ns in an approximately Gaussian temporal profile. The spot size was estimated by placing a small CCD camera near focus with a significant amount of neutral density filters in the beam line to prevent damage to the camera. The camera position was varied until the smallest spot was obtained. The image of the spot was recorded and converted from pixels to spatial units based on the CCD size and resolution. The spot size was measured to be $\sim 250\,\mu\mathrm{m}$ and this varies little with uncertainties in target position due to the long focal length of the focusing lens.

The optical lines for interferometry and spectroscopy cut across the two ports such that their field of view was perpendicular to the drive laser axis. The three-axis B-dot probe was positioned horizontally (along the same axis as the drive laser) above the target. The Langmuir probe was mounted vertically at an off angle of $\sim 25°$ but pointed such that the expanding shock would travel parallel along the length of the probe tips. A visual representation of the experimental setup is depicted in Figure 7.1.

7.3 Interferometry

7.3.1 Theory of interferometry

A Mach-Zehnder interferometer consists of a laser, two optical paths, and a recording device, in this case a CCD camera, as depicted in Figure 7.2. The laser is passed through a 50/50 beamsplitter where one beam (the object beam) is redirected through the target chamber while the other beam (the reference beam) is directed in air around the chamber. The beams are then recombined at another 50/50 beamsplitter where they interfere and the resulting beam is imaged onto a CCD. Provided that the wavefronts of the object and reference beams

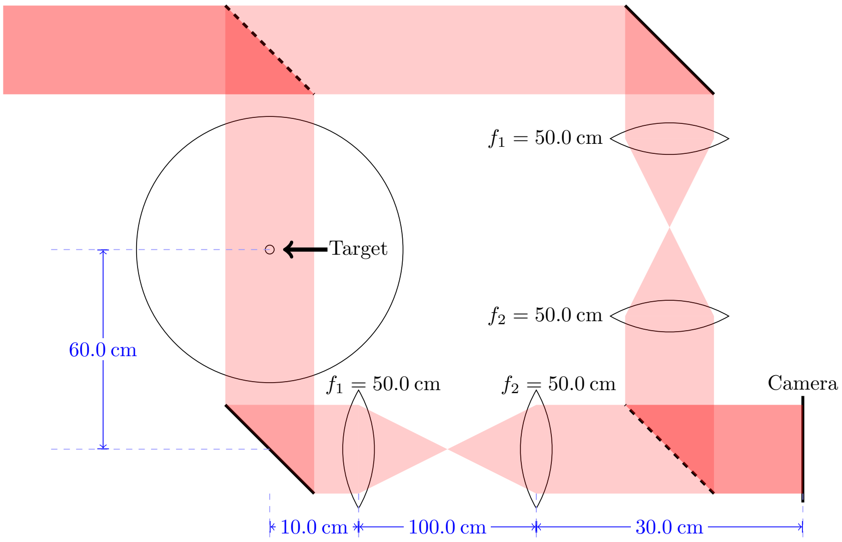

Figure 7.2: A schematic of the Mach-Zehnder interferometer setup for the experiment. Mirrors are solid, bold lines, while beamsplitters are dashed lines. The laser is sourced at the top left corner and ends in the bottom right corner where the interference pattern is imaged by a CCD camera.

are slightly misaligned, and if the refractive indices encountered along each path are identical then a regular array of light and dark interference lines, fringes, is seen. If however, the refractive index along one path is different from the other, such as when a sufficiently dense plasma is present, then the relative phase of the wavefronts is shifted and they interfere in different spots leading to a distortion in the fringe pattern. These measured phase distortions can be translated back into changes in refractive index which are a function of electron density.

The Fourier transform technique uses a carrier frequency to separate zero-order, background, spectrum and first-order spectrum, where spectrum refers to the frequency of the fringes. It is the first-order spectrum which is important, because it carries phase information. This carrier frequency is introduced by slightly misaligning the object and reference wavefronts in a Mach-Zehnder interferometer, introducing a set of (locally) evenly spaced fringes even in background images where no plasma is present to produce a phase shift. The carrier frequency acts to modulate the phase shifts away from zero-order thereby allowing us to distinguish between phase and intensity changes. To retrieve just the phase information, the interferograms are Fourier transformed and everything but the first-order portion of the spectrum is filtered or "masked out".

For any idealized interferometer, the modulated spectrum would be a small dot in frequency space at the carrier frequency distance from the zero-order dot. In any real-world system the optical lines will have some imperfections and phase shifts will appear even in a background interferogram. Therefore, for every shot, a background is taken and processed identically to the shot interferogram. The phase of the background is subtracted from the shot interferogram to minimize error from imperfections in the optical line.

Due to the reliance on modulation and demodulation by the carrier frequency, the Fourier transform method (FTM) is restricted by the Nyquist-Shannon sampling theorem. A sufficiently large carrier frequency must be chosen such that aliasing effects from the width of the first-order spectra do not overlap. Consequently, high resolution cameras are required to resolve the thin fringes in the interferogram. Fortunately, most modern CCD cameras meet this requirement with ease (155).

The setup depicted in Figure 7.2 also shows two sets of lenses on both the object and reference beam paths. These lenses allow us the flexibility to convert the arrangement from interferometry to schlieren or shadowgraphy, though neither technique was used extensively. Schlieren works by blocking the reference arm and placing a small block (typically referred to as a knife edge or schlieren filter) in the focal point of the object beam. Normally, the monochromatic laser light would come to focus all at the same point and be blocked by the schlieren filter, but any light which has encountered large density gradients on its path will be deflected and will no longer focus at the same point as the undeflected light. This results in an image of density gradients which were sufficiently large to deflect light around the schlieren filter (156, 157). Schlieren was not extensively used in this experiment so it will not be elaborated upon it any further. There is a second benefit to having the lenses in the line. The lenses are effectively imaging the target making the edges of objects, where light is deflected, come into sharper focus on the interferograms. This also helps if we wish to convert the optical setup to shadowgraphy, which measures second order density gradients, by simply blocking the reference beam line (156). While shadowgraphy was not used, the increased sharpness and contrast in the interferograms was useful during analysis.

Interferogram Analysis

The process of analyzing the interferograms, using the Fourier transform method, is as follows:

1. Mask all the regions where there are no fringes or where the fringes are broken (discontinuous)
2. 2D fast Fourier transform (FFT) the image
3. Demodulate the carrier frequency
4. Apply a low-pass filter to remove everything but the demodulated signal
5. Inverse Fourier transform (IFFT) the demodulated/filtered signal and retrieve the amplitude and wrapped phase
6. *Unwrap* the 2D phase map from modulo 2π to the real phase map
7. Repeat the process for the background image and take the difference between the two unwrapped phase maps
8. Convert the phase map to electron density

The analysis process is depicted in Figure 7.3 for a background interferogram (i.e. with no plasma present). The technique of using a carrier frequency is precisely amplitude modulation (AM), the same technique used in AM radio transmission, therefore it is expected that the amplitude resulting from the analysis is simply the envelope of the initial signal, as seen in subfigures b.) and e.) of Figure 7.3. It should be noted that the spectrum must be multiplied by a factor of 2 to restore the correct amplitude, since in the demodulation and filtering steps we have only taken half of the carrier frequency signal and filtered out the negative frequency component. More advanced interferometric techniques are

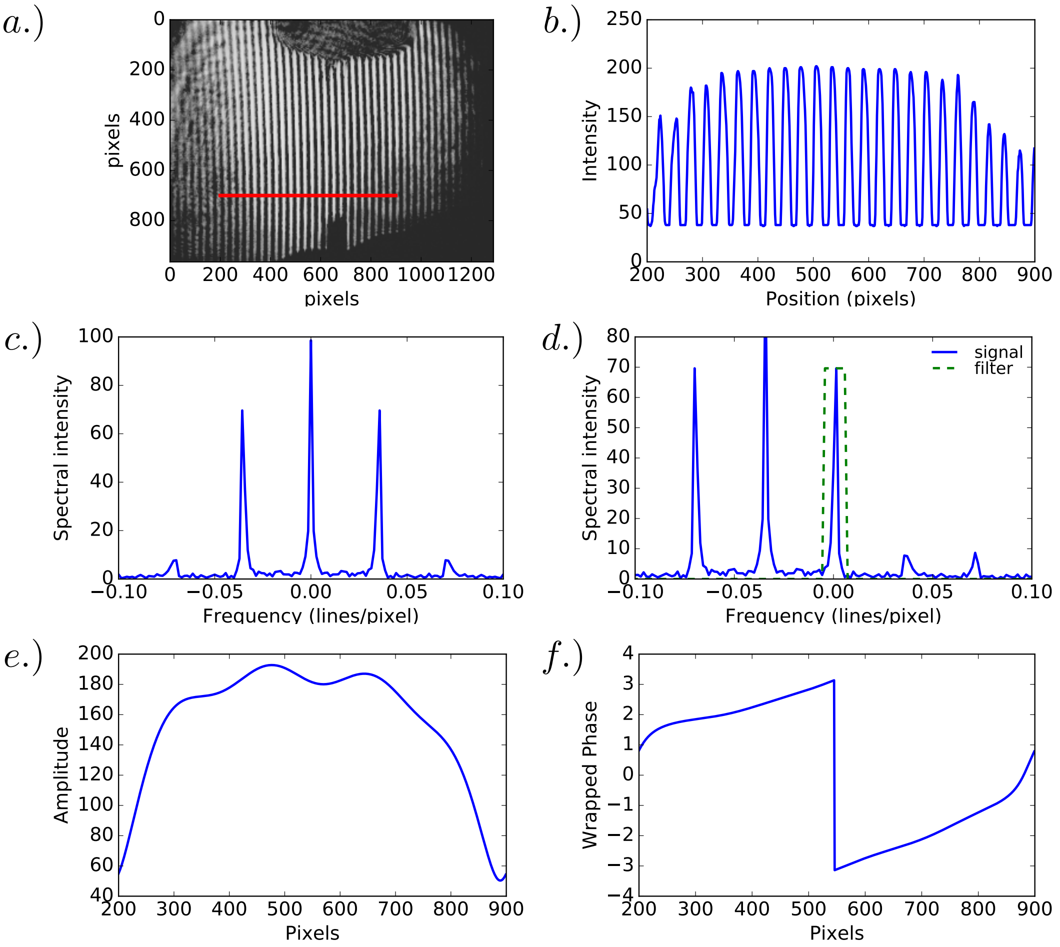

Figure 7.3: *a.)* Background interferogram with red line indicating lineout. *b.)* Intensity profile of the lineout *c.)* Fourier transform of lineout showing a DC component and two symmetric peaks at the carrier frequency. *d.)* Demodulated Fourier spectrum with application of square filter depicted by green dashed lines. *e.)* Amplitude retrieved from inverse Fourier transformed signal after demodulation and filtering. The amplitude is consistent with the envelope of the intensity in panel b. *f.)* Wrapped phase retrieved from aforementioned process. The undulations in the center of the amplitude and at the edges of the phase may be due to Gibbs phenomena from the square filter acting as a sinc function in reciprocal space.

possible by multiplexing and in certain cases additional information, such as magnetic field strength, may be extracted from the amplitude modulations generated by Faraday rotation (158).

In panel f.) of Figure 7.3 we see a saw-tooth pattern where the phase suddenly flips from $+\pi$ to $-\pi$. Due to the sinusoidal nature of light as a wave, any phase differences between the object and reference beams greater than 2π are indistinguishable from phase difference modulo 2π. To recover the true phase difference, we must *unwrap* the interferogram, that is map it from modulus 2π back to total phase difference. If there are no additional discontinuities in the interferogram, then unwrapping is simply a matter of displacing the phase discontinuities until they form a smooth curve. Such a mapping is mathematically one-to-one (bijective), so a phase map modulus 2π uniquely converts to a real phase map.

The most basic method for unwrapping the phase is as follows:

1. Enumerate the sampled phase points from left to right ($a_1 \dots a_N$)
2. Take the difference $a_i - a_{i-1}$ starting with $i = 2$
3. If $a_i - a_{i-1} > +\pi$, subtract 2π from all points $a_i \dots a_N$
4. If $a_i - a_{i-1} < -\pi$, add 2π to all points $a_i \dots a_N$
5. Iterate until all points $i = 2 \dots N$ have been processed

This basic algorithm is highly susceptible to noise, undersampling (less than Nyquist frequency), and dislocations (broken fringes), which can be misidentified as real phase wraps. Most unwrapping algorithms use this algorithm as their basis and construct elaborate defences against sources of error by either creating unwrapping paths which avoid phase residues induced by errors (e.g. branch-cut method), or by identifying and growing regions of high quality phase data prior to lower quality phase data (e.g. weighted least squares) (155).

Next, we convert the unwrapped phase map into electron density by making certain physical assumptions about how the plasma deflects the interferometry

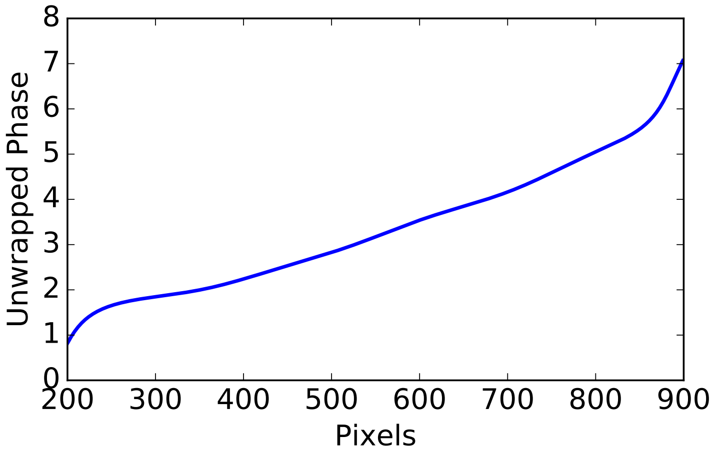

Figure 7.4: Unwrapped phase of Figure 7.3 using the basic unwrapping algorithm. The phase is linearly increasing with position, as is expected from the spatial displacement of the wavefronts used to generate the carrier frequency.

beam. The fringe shift for probe with wavelength λ and path length through the plasma L is given by (159)

$$s = \left[\frac{\Delta(\mu - 1)}{\lambda}\right] L \tag{7.1}$$

where $\Delta(\mu - 1)$ is the phase change in refractivity $(\mu - 1)$.

For free electrons the refractivity comes from the classical dispersion formula for an electron gas which assumes that the probe frequency is greater than the electron-ion collision frequency $\omega \gg \nu_{ei}$ (159).

$$(\mu - 1)_e = -\frac{1}{2}\frac{\omega_{pe}^2}{\omega^2} = -4.46 \times 10^{-14}\lambda^2 N_e \tag{7.2}$$

where ω_{pe} is the electron plasma frequency, N_e is the electron density, ω is the probe frequency and λ is the probe wavelength in cm.

The refractivity of the background gas is given by

$$(\mu - 1)_{gas} = 5.15 \times 10^{-24} N_{gas} \tag{7.3}$$

where N_{gas} is the density of the gas in cm^{-3}. Typically, the refractivity of the gas fill as well as that of protons is negligible and we assume $\Delta(\mu - 1) = (\mu - 1)_e$.

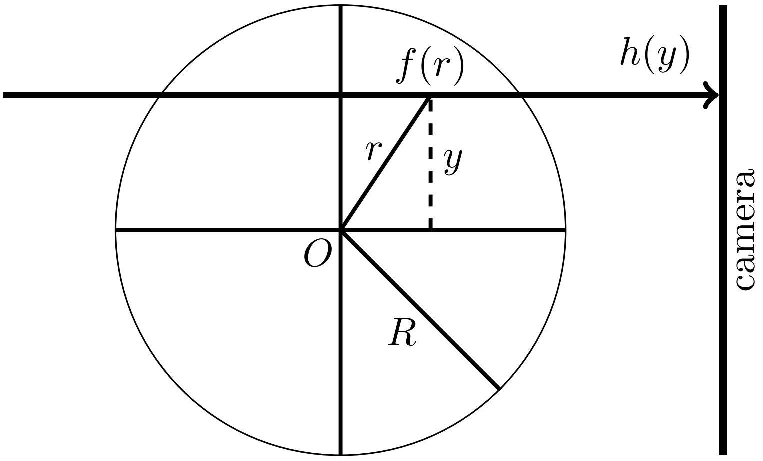

Figure 7.5: Cross-sectional diagram of a system where Abel-inversion is applicable. The drive laser axis is going into the page. We have a plasma of radius R with radially-symmetric property $f(r)$. We probe for $f(r)$ using a camera, which integrates along the line of sight, resulting in measured value $h(y)$.

Substituting Eq. 7.2 into Eq 7.1 and solving for density:

$$N_e = -2.24 \times 10^{13} \frac{s}{L\lambda} \tag{7.4}$$

Our phase difference map is s in the above equation, which simply needs to be multiplied by a constant factor, from Eq. 7.4, depending on the probe beam wavelength and the approximate thickness of the probed plasma to obtain density in units of cm^{-3}.

The aforementioned analysis steps for phase extraction were carried out in the Interferometric Data Evaluation Algorithms (IDEA) software for the data presented in the following chapter (160).

Abel Inversion

In the previous section, when converting the phase to electron density it was assumed that the interferometry beam passes through a plasma of uniform density along the line of sight and with thickness L. This may lead to inaccurate spatial distributions of density for plasmas which are inhomogeneous along the line of sight, as we would expect for an expanding shock front. Fortunately, for radially symmetric plasmas, the problem of obtaining the correct density distribution is easily solved by Abel-inversion. We expect the plasma expansion to be cylindrically symmetric about the drive beam, therefore the interferometry beam is positioned orthogonal to the drive beam to allow for accurate Abel-inversion.

The projection through a plasma is given by the integral of the radially-symmetric property (in this case, refractivity, or density) along the line of sight:

$$h(y) = 2\int_{y}^{R} f(r)\frac{r}{\sqrt{r^2 - y^2}}dr \tag{7.5}$$

where $h(y)$ is projection, or what we measure on the camera, y is the vertical distance on the camera, R is the radius of the plasma, r is the radial distance to some plasma element, and $f(r)$ is the true radial distribution of the observed property, which is what we desire to know. This situation is depicted in Figure 7.5.

The above expression can be analytically inverted to obtain $f(r)$:

$$f(r) = -\frac{1}{\pi}\int_{r}^{R} \frac{dh(y)}{dy}\frac{1}{\sqrt{y^2 - r^2}}dy \tag{7.6}$$

though this expression, if directly implemented for analysis, is susceptible to noise in the differentiation of $h(y)$ and is sensitive to errors in estimating the position of $r = 0$, the axis of symmetry.

An alternative, robust formulation is given by Pretzier (1991) where $f(r)$ is expanded by a Fourier-like series (161):

$$f(r) = \sum_{n=N_l}^{N_u} A_n f_n(r) \tag{7.7}$$

where N_l and N_u are chosen to set the lower and upper bounds of the frequencies, respectively, and A_n are unknown amplitudes. $f_n(r)$ are given by cosine functions:

$$f_0(r) = 1,\ f_n(r) = 1 - (-1)^n \cos\left(n\pi\frac{r}{R}\right) \tag{7.8}$$

This allows us to rewrite the Abel equation as

$$H(y) = 2\sum_{n=N_l}^{N_u} A_n \int_{y}^{R} f_n(r)\frac{r}{\sqrt{r^2 - y^2}}dr \tag{7.9}$$

where the entire integral can be numerically computed and saved to a table, thereby eliminating the noise problems caused by differentiation and speeding up computing times. Noise can be further reduced by choosing the bounding frequencies to act as a filter. The data $h(y)$ are then least squares fitted using $H(y)$, to obtain the coefficients A_n. The coefficients are subsequently plugged into Eq. 7.7 to retrieve the true spatial distribution of densities $f(r)$. This methodology has the added benefit that errors in identifying $r = 0$, the axis of symmetry, propagate less readily than they do in the analytic formulation.

7.3.2 Interferometer setup

A Coherent Inc. Hidra laser was used in constructing a Mach-Zehnder interferometer for probing the electron density of the shock. When optimized, the laser emits 40 mJ over 40 fs at 810 nm. This is achieved through a technique known as *chirped pulse amplification* (CPA), which is done in three stages. First, a seed beam passes between two offset gratings which diffract and temporally stretch the laser by forcing the different spectral components of the underlying seed beam to take paths of slightly different distance (162). In the second stage, the stretched seed beam is passed through a crystal which is pumped by a second laser. The pumped crystal has an inverted population where the electrons are occupying higher energy states than ground, and as the seed beam passes through it stimulates emission, adding photons to the seed beam. Once all the energy has been collected by the seed beam, it is sent to a third stage where the beam is temporally compressed by diffraction gratings in the inverse process of the first stage. What is important here, is that for the purposes of interferometry we do not need this much energy or even that short of a pulse length since the plasma is expected to evolve on nanosecond timescales. In fact, the short pulse length is a hindrance to aligning the interferometer since the arms of the interferometer must have the same path length to within $d_{error} = t_{pulse}c \sim 10\ \mu\text{m}$ for a 40 fs laser so that the wavefronts arrive at the camera at the same time and interfere. These setup constraints were eased by misaligning the compression stage in the CPA arrangement to keep the beam at stretched pulse width of $\sim$ 1 ps, giving a manageable uncertainty of $\sim$ 0.5 mm in the distances of the interferometry lines. The laser energy was attenuated through use of neutral density filters to prevent damage to the CCD and provide a good contrast between the object and reference beams of the interferometer.

The CCD camera used to record the interferograms was a PTGrey Chameleon3 CM3-U3-13S2M which had a resolution of 1288 × 964 pixels with a pixel size of 3.75 μm/pixel. The spatial resolution and field of view (FOV) of the camera were measured by inserting fine mesh grids of known size at the target position. The spatial resolution was found to be $\sim 9\,\mu$m/pixel. This gives a magnification factor of $\sim 0.4\times$ consistent with the magnification factor of the second lens in Figure 7.2. Temporal gating on the camera was not required since the pulse length of the laser was much shorter than the phenomena under observation, and any other light sources in the room were obscured by an infrared bandpass filter mounted on the front of the CCD housing. The camera readout method was global shutter, as opposed to rolling shutter, which meant that the images would not be distorted due to fast movement in the image.

7.4 Emission spectroscopy

For measurement of emission spectra a Czerny-Turner spectrograph (Andor Shamrock 500i with iStar 734 series CCD) was used, as depicted in Figure 7.6. This spectrometer diagram is different from the interferometry diagram (Figure 7.2), in that points where rays converge are in focus, so an image is formed at those points. The purpose of the two external lenses is to form an image of the plasma onto the spectrometer slit. The internal collimating and focusing mirrors in the Czerny-Turner spectrometer form an image of the slit on the camera. Therefore placing a Hg pen lamp directly in front of the slit forms an image on the camera and may be used to obtain the instrument function. The f-number of the spectrograph was $f/6.5$ and the imaging lenses were chosen to match this f-number as closely as possible to minimize the amount of light lost through the system.

Measurements taken by the spectrometer were spatially resolved, and the field of view calibration was acquired by simply imaging a ruler placed within the target chamber. The CCD resolution was 1024 × 1024 pixels with a pixel size of 13 μm. From observing the ruler a spatial resolution of 0.03 mm/pixel was

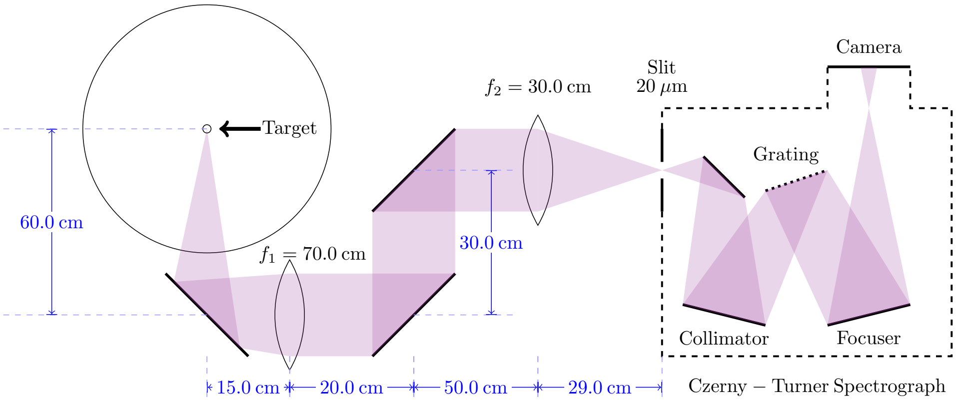

Figure 7.6: Emission spectroscopy setup using a Czerny-Turner Spectrograph. The spectrograph has an f-number of $f/6.5$. Lenses f_1 and f_2 are both 2" (5.08 cm). The grating has a groove density of 600 ℓ/mm. The entrance slit width was set to 20 μm and no exit slit was used.

recorded. This gave a magnification of ~ 0.43 which is consistent with the setup of the optical lines. The time delay of the spectrometer relative to the drive beam was obtained by glinting off of a golden sphere target with the drive laser on low power. The time delay and gating of the spectrometer were narrowed down until the reflection of the laser was only visible within the gated timing and not outside of it.

Absolute intensity (whitelight) calibration, spectral calibration, and measurement of the instrument function are discussed in further detail in subsequent sections. A background image was taken prior to every shot to subtract any noise due to other emission sources and any possible electrical noise due to thermal variations on the CCD. This thermal noise was also mitigated by cooling the CCD chip to 0° C

7.4.1 Theory of Emission Spectroscopy

Emission spectra are generated by spontaneous emission of photons due to electrons dropping from higher energy levels to lower energy levels in an atom. The distribution of electrons among the energy levels, and thus the proportions of emitted spectra, is dependent on the electron temperature. In equilibrium, one would normally use the Saha-Boltzmann distribution to relate the intensities of two different spectral lines to the electron temperature of the plasma (23, 142, 163).

$$\frac{\epsilon_z\left(p\rightarrow q\right)}{\epsilon_z\left(p'\rightarrow q'\right)}=\frac{\lambda_{p'q'}}{\lambda_{pq}}\frac{A_z\left(p\rightarrow q\right)}{A_z\left(p'\rightarrow q'\right)}\frac{g_z(p)}{g_z(p')}\exp\left[-\frac{E_z(p)-E_z(p')}{k_BT_e}\right] \tag{7.10}$$

where ϵ_z is the emission coefficient in units of W m^{-3} sr^{-1} for ionization state z, λ_{pq} and $\lambda_{p'q'}$ denote the wavelengths of the two lines under comparison, A_z is the Einstein coefficient of spontaneous emission, $g(p)$ is the statistical weight of the upper energy level in the transition, $E(p)$ is the energy of the upper level in the transition, and T_e is the electron temperature. In the above, p is the upper level and q is the lower level in a transition, while the apostrophes, or lack thereof, are used to distinguish the two lines under comparison in the ratio.

This method of taking line ratios excludes the need for absolute calibration of the spectrometer with respect to measured intensities since only the relative intensity is important. When multiple lines are measured, a Boltzmann plot may be generated to retrieve the electron temperature by linear regression (142).

The line ratios method requires sufficiently different lines, that is, different energies or electron scattering cross-sections. The former is often achieved by comparing lines from two different elements (requiring prior knowledge of densities) or for lines from the same element which have an energy separation larger than the thermal energy. The latter is used when forbidden transitions (theoretically forbidden under dipole approximation but allowed in higher-order terms, and thus often negligible) are strong enough to be measured (163). If all of our lines are Ar II then this method is insufficient as the energy separations between lines under comparison will be too small. Therefore, we need to absolutely calibrate the spectrometer using a white light source. The absolute values of measured irradiance can be used to obtain not just electron temperature but density, and possibly other parameters as well. These are obtained from the peak intensity, whereas lines may also be sensitive to Doppler and Stark broadening mechanisms yielding information on electron temperature and density for whitelight calibrated and uncalibrated spectrometers alike.

For a plasma in LTE, we may use the following equation to describe the absolute emission:

$$\epsilon\left(p \rightarrow q\right) = \frac{h\nu_{pq} A_z\left(p \rightarrow q\right)}{4\pi n_z} \frac{g_z(p)}{U_z(T_e)} \exp\left[-\frac{h\nu_{pq}}{k_B T_e}\right] \tag{7.11}$$

where n_z is the total local density, h is Planck's constant, ν_{pq} is the frequency of the emitted photon, and $g_z(p)$ is the statistical weight of the upper energy level. $U_z(T_e)$ is the partition function of ionizing stage z, given by:

$$U_z(T) = \sum_{i=g}^{\infty} g_z(i) \exp\left[-\frac{E_z(i) - E_z(g)}{k_B T}\right] \tag{7.12}$$

where (i) denotes the ionization stage and (g) is the ground state.

There are two main effects that plasma parameters have on emission spectra. The first is changes in intensity due to variation in populations at various energy levels. In equilibrium, these populations are dictated by the Saha-Boltzmann distribution which shows a strong dependence on electron temperature(23, 142).

The second effect is broadening. There are a wide array of broadening mechanism including, but not limited to: Doppler broadening, Stark or pressure broadening, instrument broadening, natural broadening, and Zeeman broadening. One can think of the idealized spectra as infinitely thin Dirac-delta pulses positioned at photon energy corresponding to the energy level transition the electron underwent to emit the photon. These idealized spectra are, at the very least, broadened by Heisenberg's uncertainty principle in the process known as *natural broadening*. The resolution of the measuring instrument also acts to broaden the spectra, known as *instrument broadening*. When multiple broadening effects are at play they may be additively convolved to simulate the resulting spectra. Most broadening effects are either Gaussian or Lorentzian, which when convolved with themselves they return the same profile, but when convolved with each other they return a Voigt profile (142).

Natural Broadening

No emission lines, nor the corresponding energy levels in an atom, are infinitely sharp. At a fundamental level, there is an uncertainty in the energy levels which is related to the the lifetime of an energy state via Heisenberg's uncertainty principle $\Delta E \Delta t \geq \hbar/2$. For quasi-stationary, LTE states, the time intervals are exponentially distributed yielding a Lorentzian profile in the spectra. The relative width of this profile is given by (142):

$$\frac{\Delta\lambda_{1/2}}{\lambda_{pq}} = \frac{\lambda_{pq}}{2\pi c}\left[A\left(p \rightarrow\right) + A\left(q \rightarrow\right)\right] \tag{7.13}$$

where $\Delta\lambda_{1/2}$ is the full width at half maximum (FWHM), λ_{pq} is the wavelength of the photon emitted by an electron dropping from energy level p down to energy level q. c is the speed of light and $A\left(p \rightarrow\right)$ is the reciprocal of the radiative life time of the upper level $\tau = 1/\sum_{q<p} A\left(p \rightarrow q\right) = 1/A\left(p \rightarrow\right)$ while $A\left(q \rightarrow\right)$ is the reciprocal of the radiative life time for the lower level, also known as the Einstein coefficient of spontaneous emission.

For the Hg I line at $\lambda = 435.8\,\mathrm{nm}$ with Einstein coefficient $A = 5.57 \times 10^{7}\,\mathrm{s}^{-1}$ we expect $\Delta\lambda_{1/2} \sim 5\,\mathrm{fm}$, making natural broadening negligible in comparison to other sources of broadening.

Doppler Broadening

Spectral lines may also be upshifted or downshifted by the Doppler effect if the emitter has some velocity component relative to the line of sight of the spectrometer. In a plasma described by a Maxwell-Boltzmann distribution, the random thermal velocities of the emitters will each upshift or downshift their respective emitted photons. The sum of these shifts is a broadening in the emitted line, also known as Doppler broadening, which is Gaussian in shape (142, 163).

The relative width of the Doppler broadening distribution is given by (142)

$$\frac{\Delta\lambda_{1/2}}{\lambda_{pq}} = \sqrt{\frac{8k_B T_a}{m_a c^2}\ln 2} \tag{7.14}$$

where T_a and m_a are the temperature and the mass of the emitter a, respectively.

It is the case for most plasmas under spectroscopic study that Doppler broadening is the most significant source of broadening (besides instrumental broadening). This is because most plasmas are generated by heating up matter until it thermally ionizes, and these temperatures coincide with when Doppler broadening becomes important. Although it should be noted that modern lasers are giving us the ability to generate pressure ionized plasmas in the lab.

Stark Broadening

Stark, or pressure broadening is caused by particles in the same system perturbing the energy levels of an atom via long-range electric fields. These electric fields rely both on the density of particles and the screening by surrounding particles, meaning that this technique can be used to obtain a measure of density. The theoretical description of Stark broadening can be complex due to the need to model a large number of charged particles interacting by long-range Coulomb forces. In principle, one would need to solve a time-dependent Schrödinger equation including the dipole moment for the radiating bound electron (neglecting the small monopole and multipole terms), for which there is no general solution. Fortunately, there are two reasonable approximations: the impact approximation and the quasistatic approximation (142).

In the impact approximation, the Baranger formula gives the electron impact broadening of a spectral line for transition $p \to q$ as (142, 164):

$$\begin{aligned}\Delta\omega_{1/2} = n_e \int_0^\infty v f_e(v) \left(\sum_{p' \neq p} \sigma_{pp'}(v) + \sum_{q' \neq q} \sigma_{qq'}(v) \right) dv \\ + n_e \int_0^\infty v f_e(v) \left(\int \left| \phi_p\left(\theta, v\right) - \phi_q\left(\theta, v\right) \right|^2 d\Omega \right) dv \quad (7.15)\end{aligned}$$

where n_e is the electron density, v is the velocity of the scattered electron, $f(v)$ is the Maxwellian electron distribution, $\sigma_{pp'}$ and $\sigma_{qq'}$ are the inelastic cross sections linking the initial and final levels, respectively, with the other perturbing levels. $\phi_p\left(\theta, v\right)$ and $\phi_q\left(\theta, v\right)$ are the elastic scattering amplitudes for the ion in the initial and final energy levels. The integral is taken over the scattering angle, θ, with solid angle element $d\Omega$. The first term on the right-hand side represents inelastic collisions, connecting the upper and lower levels of the transition to perturbing levels p' and q'. The second term accounts for elastic collisions.

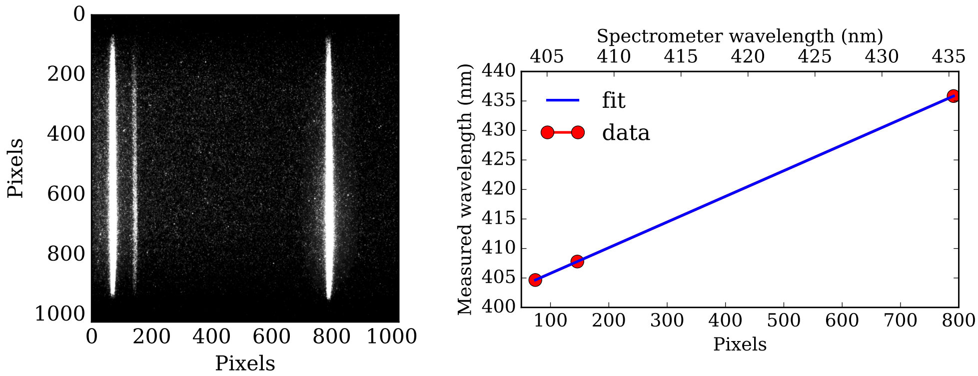

Figure 7.7: *Left:* Spectra emitted from a mercury pen lamp, consisting of Hg I lines at 404.656 nm, 407.783 nm, and 435.833 nm. *Right:* Dispersion curve from plotting the peak positions of the Hg I lines against their known values (red points), and fitting a line to these points (blue). The fit has a value of $R^2 = 1$ to within 7 decimal places, meaning that the dispersion curve is linear. The wavelength listed by the spectrometer software is plotted on the upper axis and corresponds well with the dispersion calibration.

When the perturbation of the lower state, q, can be neglected, Eq. 7.15 simplifies to the one-state equation (142):

$$\Delta\omega_{1/2} \approx n_e X(p) \tag{7.16}$$

where $X(p)$ is the sum of all elastic and inelastic collisional rate coefficients (165).

Reviews of publications investigating Stark widths for Argon II in the UV to optical range for $T_e \sim 1.5$eV and $n_e \sim 1\times10^{17}$cm^{-3} show an expected Stark width of $\sim$ 30pm which is below the maximum spectral resolution of the spectrometer, at 70 pm (166). Therefore it is not expected that Stark broadening will be observed and density information will have to be obtained from the intensity of the lines using absolutely calibrated measurements.

Dispersion calibration

The spectral dispersion of the spectrometer was obtained by measuring the lines emitted by a Mercury pen lamp positioned near the entrance slit of the spectrom-

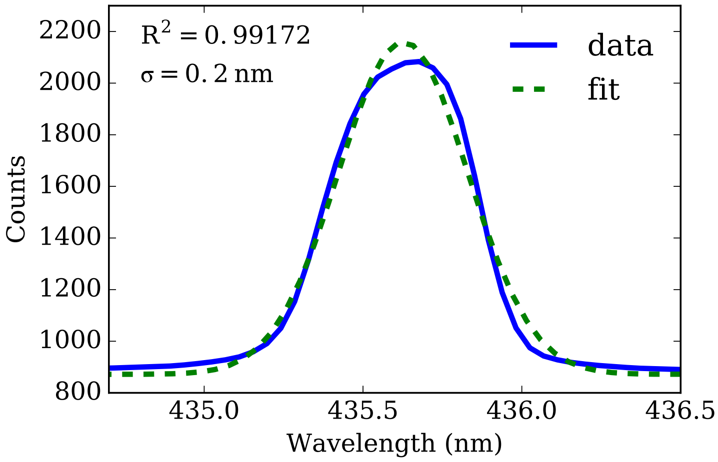

Figure 7.8: Instrument function for spectrograph with slit width of 20 μm. The observed line is Hg I at 435.8335 nm emitted by a mercury pen lamp. The line is well fitted by a Gaussian with $\sigma = 0.2$ nm.

eter. The slit width was set to 20 μm, which was the same width used during the experiments.

From Figure 7.7 we see that the measured dispersion is linear to high precision and that the wavelength listed by the spectrometer software is consistent with the measured values. The spectra measured during the experiment were at or near the wavelength range in the dispersion curve, allowing for linear interpolation/extrapolation in converting pixel position to wavelength for measured spectra.

Instrument function

The instrument function of the spectrometer was obtained by measuring an Hg I line at 435.8 nm using the same pen lamp as was used for the dispersion calibration. The slit width was set to 20 μm just as in experiments. The spectrogram was spatially integrated to give a plot of counts against wavelength, and the measured line was fitted with a Gaussian profile as shown in Figure 7.8.

Since the lines emitted by a Hg pen lamp are relatively thin, minimal natural broadening can be assumed, meaning that all of the broadening can be attributed

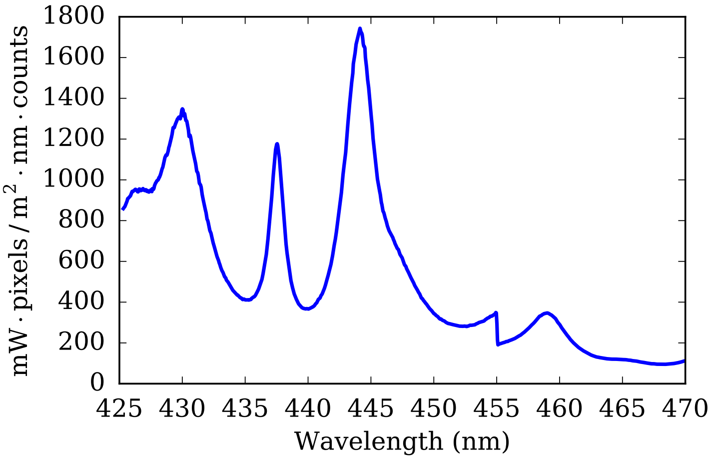

Figure 7.9: Plot of whitelight calibration curve obtained for optical line and spectrograph using Bentham CL6 Irradiance Lamp with a gain of 20, gate time of 1 ms, and signal integrated across 287 pixels. It is assumed that the gain and the gate timing for spectra obtained during shots are 255 and 10 ns respectively. To convert measured spectra to irradiance, the measured counts and the number of pixels over which those counts were integrated are required.

to the spectrometer. The FWHM of the instrument function is used as a measure of the spectral resolution for convolving simulations from PrismSpect to accurately reproduce the measured spectra for fitting.

Whitelight calibration

A Bentham CL6 Irradiance Lamp was used as a whitelight source for absolute calibration of the spectrometer. This source was calibrated with respect to a Quartz Halogen lamp standard calibrated by the National Physical Laboratory, UK. The emitted spectrum is essentially a Planckian, characteristic of a blackbody. The source was placed inside the target chamber and carefully pointed along the spectrometer's optical path to obtain a calibration of the entire system. The spectrum was measured in counts and then divided into the calibration curve provided by Bentham in their specification sheet. The resulting calibration curve converts spectra measured in counts to a measure of irradiance, and can be seen in Figure 7.9. It is important to note that the sharp peaks at lower wavelengths

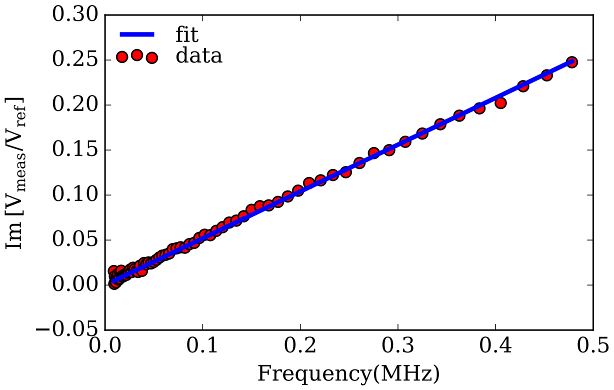

Figure 7.10: Example of bdot probe calibration in low frequency portion of network analyzer signal. The slope of this fit yields the coil area along one axis, which in this case is $a_z = 10.12\,\mathrm{mm}^2$. Note that this is not the calibration for the probe used in the present experiment, though they are similar in construction and composition.

can cause significant deviation in fitting the calibrated spectrum with simulations if there is uncertainty in the spectral axis. If large differences are seen among simulated and measured spectra for the expected plasma parameters, it is better to trust the spectra at higher wavelengths as here the whitelight calibration is flatter.

7.5 Three-axis Bdot

Bdot probes, as their name suggests, measure changes in magnetic field over time. A simple bdot probe consists of a loop of wire with a resistor closing the circuit on the other end. When a changing magnetic field is passed in the vicinity of the wire an electric current is induced as described by Faraday's law of induction:

$$\oint \mathbf{E} \cdot d\ell = -\int \frac{\partial \mathbf{B}}{\partial t} \cdot d\mathbf{A} \tag{7.17}$$

where $\mathbf{E}$ is the induced electric field, ℓ is the wire length, $\mathbf{B}$ magnetic field which is varying in time t through a loop of area $\mathbf{A}$.

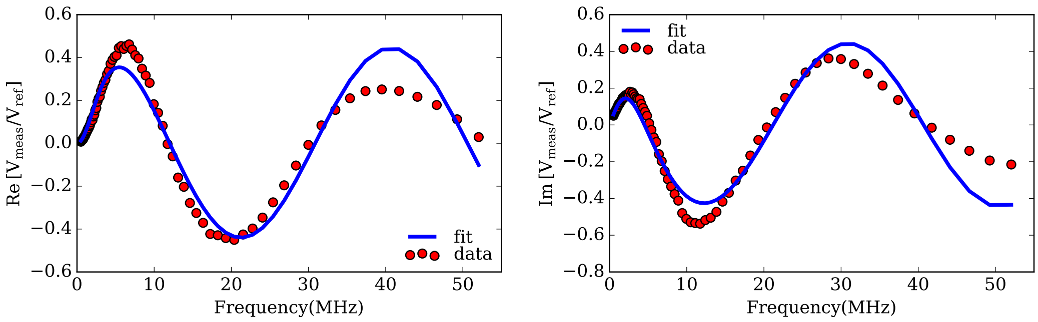

Figure 7.11: Example of bdot probe calibration in high frequency portion of network analyzer signal. In this case we get the delay of the z-axis coil, $\tau = 24.9\,\text{ns}$ and the characteristic inductance time of the z-axis coil $\tau_s = 41.2$ ns. The delay corresponds to $\sim 7.5\,\text{m}$ which is consistent with the length of the transmission line from the probe to the oscilloscope. Note that this is not the calibration for the probe used in the present experiment, though they are similar in construction and composition.

For a single coil of wire we may only measure the magnetic field in one direction, that is along the cylindrical axis about which the coil is wrapped. For a three-axis bdot probe, three separate coils are wrapped around a core of Vespel, to maintain structural integrity, such that they measure magnetic fields in the three orthogonal directions.

The bdot probes are calibrated by characterizing their response to a magnetic field of known quantity. The known, time-varying magnetic field is generated by rigging a Helmholtz coil to a network analyzer. The network analyzer generates a small current through the coil which creates a magnetic field down the center of the coil. The signal being sent down the coil and the response of the bdot may both be measured on the network analyzer. The bdot probe is placed in the coil and moved until we maximize the signal along one bdot axis, as seen on the network analyzer. The signals are then recorded and analyzed as described in (167).

From analyzing the calibration data one measures the areas of each of the three axes of the bdot probe and the delay in temporal response due to inductive effects. These values are directly used to convert the currents measured by the bdot into values for the measured magnetic field.

The network analyzer calibration measurements give us $\frac{V_{meas}(\omega)}{V_{ref}(\omega)}$ which can be used to obtain the area of a single turn of the B-dot coil, a, and the characteristic time scale of inductance effects, τ_s. These parameters are then used in Equation 7.18 and integrated over time to get a measure of the magnetic field:

$$aNg\frac{d}{dt}B(t) = \left[1 + \tau_s\frac{d}{dt}\right] V_{meas}(t) \tag{7.18}$$

where N is the number of coil turns, g is the gain, $B(t)$ is the measured magnetic field, and $V_{meas}(t)$ is the induced voltage measured by the oscilloscope.

The low frequency $(10 - 500\,\text{kHz})$ component of the bdot response to the network analyzer is described by

$$\frac{V_{meas}(\omega)}{V_{ref}(\omega)} = aNg\left(\frac{16}{5^{3/2}}\right)\frac{\mu_0}{rR_p}\left[(\tau_s - \tau)\,\omega^2 + i\omega\right] \tag{7.19}$$

where a is the area of a single turn, g is the gain of the differential amplifier, r is the internal resistance, R_p is the load resistance on the loop, N is the total number of turns, $\mu_0 = 4\pi \times 10^{-7}\ \text{N/A}^2$ is the vacuum permeability, τ is the electrical time delay of the circuit, and $\tau_s = (L_s + M)/R_p$ is the characteristic time scale of inductance effects where L_s is the self-inductance of the loop, and M is the mutual-inductance between two loops.

The high frequency $(10\,\text{kHz} - 50\,\text{MHz})$ component is described by

$$\begin{aligned}\frac{V_{meas}(\omega)}{V_{ref}(\omega)} = \frac{aNg\alpha\mu_0}{\pi r R_p}\frac{\omega}{1 + (\omega\tau_s)^2}&\{[\omega\tau_s\cos(\omega\tau) - \sin(\omega\tau)] \\ &+ i\,[\omega\tau_s\sin(\omega\tau) + \cos(\omega\tau)]\}\end{aligned} \tag{7.20}$$

where α is the geometry factor related to the length of the wire and the return current path.

The slope of the imaginary component in Eq. 7.19 can be used to obtain a the area per turn as demonstrated in Figure 7.10. To obtain τ_s we need to solve the system of equations given by the real and imaginary components of Eq 7.20 for τ and τ_s. This requires a nonlinear algorithm, for fitting to the network analyzer data, which is further complicated by the fact that Eq. 7.20 is oscillatory. In Figure 7.11, a non-linear least squares fit is done using the Levenberg–Marquardt

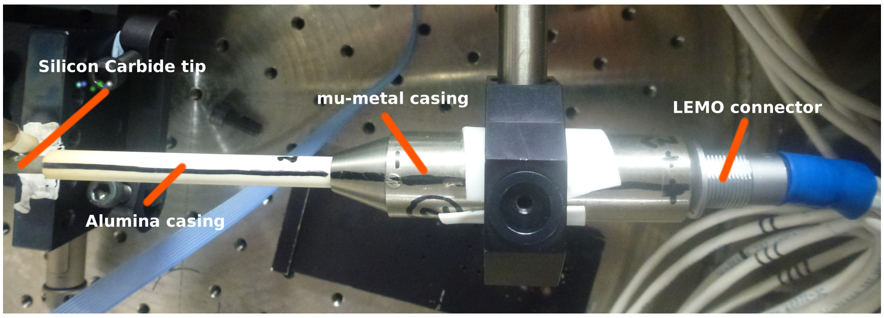

Figure 7.12: Photo of mounted bdot probe with labelled components. The vespel core with loop windings is housed in the silicon carbide tip.

algorithm. Here, one must be careful as the fit is sensitive to the choice of initial values for τ and τ_s. A simpler technique is to measure τ independently, based on the length of the circuit. For a sufficiently short circuit, we take $\tau = 0$ and fit the real component of Eq. 7.19 to retrieve τ_s.

The fits shown in Figures 7.10 and 7.11 are examples of bdot calibration. The bdot probe used in this experiment has calibration constants of $a_x = 11.03\,\text{mm}^2$, $a_y = 11.74\text{mm}^2$, $a_z = 9.37\text{mm}^2$, $\tau_{sx} = 37.6\text{ns}$, $\tau_{sy} = 38.5\text{ns}$, and $\tau_{sz} = 39.1\text{ns}$. The probe is contained in a similar body to the Langmuir probe, with alumina casings towards the tip where the vespel core and windings are seated, and tungsten/steel body with a mu-metal casing to reduce the penetration of magnetic fields into the rest of the circuit, as seen in Figure 7.12. The bdot signal is buffered and protected against external electric fields by a differential amplifier of identical design to the Langmuir probe amplifier, but with a gain of 1. The output of the differential amplifier is measured by a Z-Tec ZT4442 oscilloscope with 14-bit dynamic range, maximum non-interleaved sample rate of 400 MS/s and 300 MHz analog bandwidth. The impedance is matched to the oscilloscope and differential amplifier at 50 Ω to prevent ringing effects and signal loss on the transmission line.

7.6 Langmuir Probe

The theory of Langmuir probes has been described in depth in the previous chapter, therefore this section will briefly mention the orientation and parameters

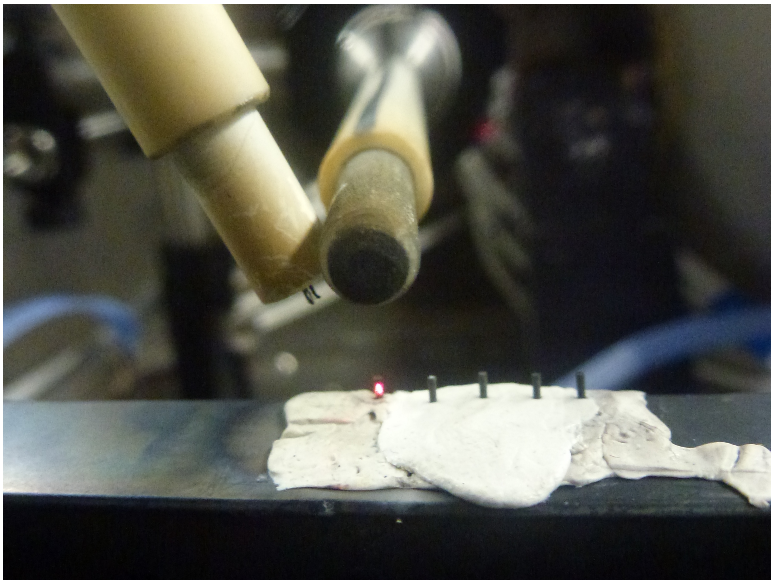

Figure 7.13: Photo of Langmuir probe, bdot probe, carbon targets, and alignment laser setup in target chamber.

of the probe. The main detail here is that the probe tips will be positioned at 6, and 7 mm away from the carbon rod target on various shots to examine time delay and any variation in the temperature and density of the shock with distance. From the perspective of the drive laser, the probe will be at an angle of $\sim 25°$ off from vertical. The tips are still pointed at the target, such that the flow is parallel to the tip length, as seen in Figure 7.13.

Probe biasing was varied between $\phi_{12} = 1.99$ V, $\phi_{13} = 9.96$ V; $\phi_{12} = 12.99$ V, $\phi_{13} = 15.06$ V; and $\phi_{12} = 5.01$ V, $\phi_{13} = 6.99$ V. The three probe currents are measured on a Z-Tec ZT4442 LXI oscilloscope with 14-bit dynamic range, maximum non-interleaved sample rate of 400 MS/s and 300 MHz analog bandwidth.

A photodiode was included on the remaining channel of the oscilloscope for accurate timing of the laser pulses relative to the current traces. This yields further confidence in the delay between the drive beam and the interferometry probe and gives time-of-flight information on the shock based on the difference between the drive peak signal and the appearance of a shock on the Langmuir probe trace or interferogram. The oscilloscope was impedance matched to the Langmuir probe with AC coupling set to 50 Ω.

7.7 Sedov-Taylor blast wave theory

It is expected that the drive beam will generate a spherically expanding shock centered around the carbon target. The propagation of such a shock is modeled by the self-similar description of the Sedov-Taylor blast wave.

The Sedov-Taylor blast wave is described by (19):

$$R = \xi_0 \left(\frac{E}{\rho_0} \right)^{1/5} t^{2/5} \tag{7.21}$$

where R is the radial position of the shock, t is the time elapsed is the shock was initiated, E is the explosion energy, and ρ_0 is the density of the homogeneous atmosphere (background gas), and ξ_o is the dimensionless similarity variable which characterizes the shock and is related to the specific heats of the gas.

Here it is assumed that the explosive energy is suddenly released in a small volume of the atmosphere over a short time, such that a shock is initiated in this volume and expands outwards.

The initial explosion is therefore only dependent on two parameters, the energy E and the density ρ_0. Proceeding with dimensional analysis, these cannot be combined to yield the desired dimensions of length or time, therefore the motion will be a self-similar function of the position R and the time t.

8

Results of Langmuir probe experiments

> *Many creative computer scientists have retreated from inventing languages to inventing tools for describing them. Unfortunately, they have been largely content to apply their elegant new tools to studying the warts and moles of existing languages... It is surprising that so many of us remain passively content with that [conventional language] structure instead of energetically searching for new ones.*
>
> —John Backus, *Can Programming be Liberated from the von Neumann style? (1978)*

8.1 Introduction

In the previous chapters we explored the theory and design of a nanosecond resolution Langmuir probe for the purpose of measuring temperature, density and plasma potential of laser-produced shocks. In this chapter, we examine the results of experiments testing the Langmuir probe against measurements from interferometry and spectroscopy. I show that the standard Langmuir probe theories are not applicable in this regime and that further studies are required to develop a suitable theory. To this end, a heuristic approach is taken where the effective collecting area of the probe and the relative probe currents are modified, assuming inhibition of currents, such that the resultant plasma parameters from applying the collisionless, thin-sheath theory, match those expected from interferometry and spectroscopy. These modifications are justified in that they are the typical places for extending the ideal, collisionless theory when accounting for additional effects such as collisions or magnetic fields.

A schematic of the experimental setup can be seen in Figure 7.1 in Chapter 7. The experiment consisted of a carbon rod target with a thickness of 0.5 mm which was ablated using a green, 532 nm laser with an energy of 2.5 J, a pulse width of 10 ns, and a spot size of 100 μm. The plasma expanded into a 1 mbar Argon gas fill which produced a radially expanding shock. The shock density was diagnosed in the plane perpendicular to the drive beam using a Mach-Zehnder interferometer with a wavelength of 810 nm and pulse width of 100 fs. The emission spectra in the $425 - 470$ nm range, where many Ar II lines are present, were collected by a spectrometer consisting of a grating with 600 ℓ/mm and a gated camera. Magnetic fields were measured using a high temporal-resolution, three-axis B-dot probe which was positioned 12 mm above the target (167). The Langmuir probe was mounted diagonally with the probe tips pointed at the target. The distance from the target to the probe tips was varied to be either 6 mm or 7 mm. Probe biasing was also varied between $\phi_{12} = 1.99$ V, $\phi_{13} = 9.96$ V; $\phi_{12} = 12.99$ V, $\phi_{13} = 15.06$ V; and $\phi_{12} = 5.01$ V, $\phi_{13} = 6.99$ V. For further details, refer back to Chapter 7.

8.2 Interferometry results

Interferograms were taken at different time delays for each shot to give information on how the shock evolves over time. Unwrapping of phase data was conducted using the IDEA software (160). Phase data was then converted to electron density by assuming the classical dispersion formula for an electron gas (159). Figure 8.2 shows a time-lapse of these line-averaged interferograms. The shock is dense and expands rapidly at early times and then slows down and becomes less dense as the expansion progresses. This is consistent with typical blast wave behavior. Abel-inversion can yield more accurate density distributions, provided that the plasma is symmetric about the laser axis, and the interferometry line is oriented perpendicular to the drive laser. Abel inversion was conducted for a set of lineouts

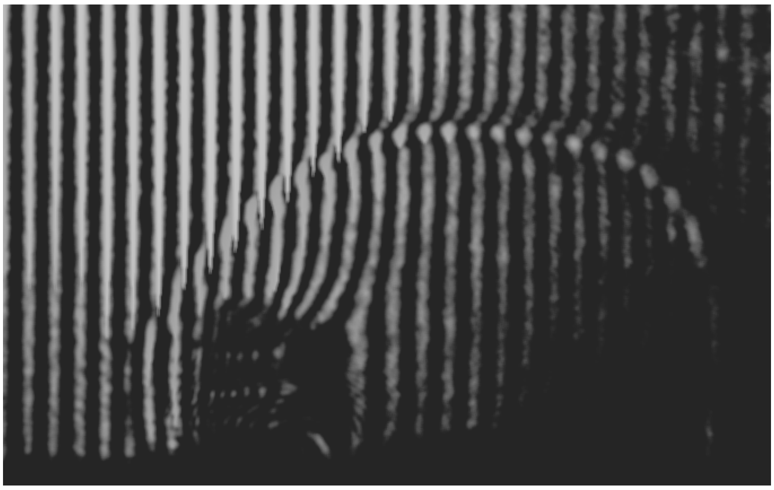

Figure 8.1: Zoomed-in interferogram taken 32.5 ns after drive beam. Significant bending of fringes is seen near the target; this is due to the high density of the shock at early times. Most of the fringes in the high contrast region are not broken and can therefore be processed using the standard Fourier transform method as shown in the top left of Figure 8.2

perpendicular to the laser axis by using a Fourier-based Abel inversion algorithm which is relatively insensitive to errors in estimating the position of the axis of symmetry (161). The algorithm requires that the density approaches zero or a constant value towards the radial limits of the data. Lineouts were taken vertically at the 0 mm position with respect to Figure 8.2 for different times. These were then Abel inverted to generate Figure 8.3. This figure is cropped to just show the progress of the shock peak. The peak density is steadily decreasing as the shock progresses and for Langmuir probes positioned at 6 or 7 cm from the target we would expect an electron density of $n_e \sim 1 \times 10^{17}\ \mathrm{cm}^{-3}$. This shock position over time was then plotted and used to fit a Sedov-Taylor blast wave function, $R = (c_1 t)^{2/5}$ as seen in Figure 8.4, where $c_1 = 5.97 \times 10^{-4}\ \mathrm{cm}^{5/2}/\mathrm{ns}$, where $c_1^{2/5} = \xi_0 \left(\frac{E}{\rho_0}\right)^{1/5}$ from Eq. 7.21. The first two interferometric points were omitted from the fit because at early times the shock position is sensitive to local variations and inaccurately modeled by the Sedov-Taylor theory (19). The teal points in Figure 8.4 are the shock arrival as measured by the Langmuir probe and discussed in subsequent sections. The Langmuir probe points were included in

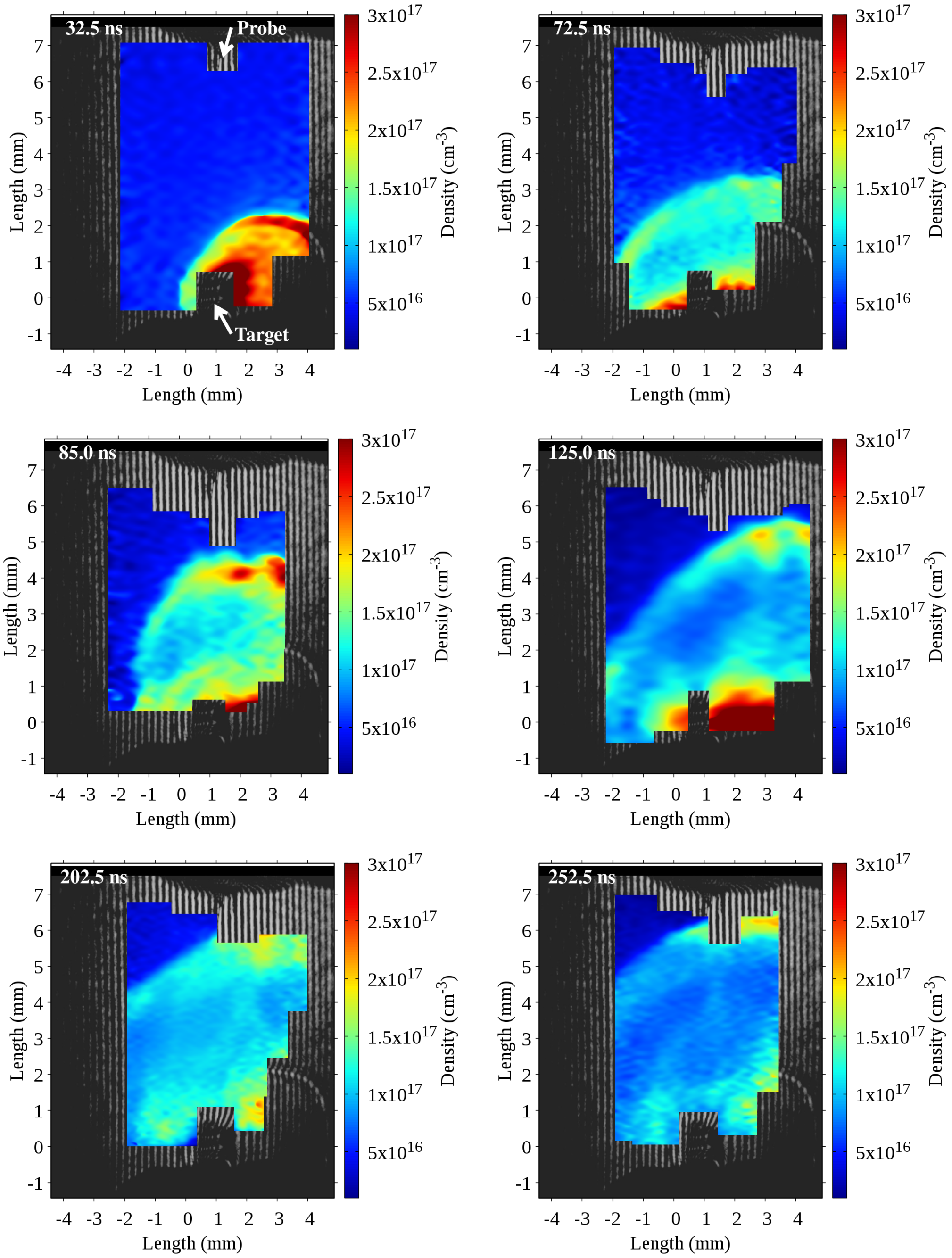

Figure 8.2: Time-lapse of interferograms acquired with different delay times with respect to the drive beam, showing the expansion of the shocked plasma. The black and white background in each subfigure is the original interferogram image while the false color overlay is the result of processing using the FTM. Regions with broken fringes or low contrast were “masked out”; anything outside of the boundaries of the overlays was masked.

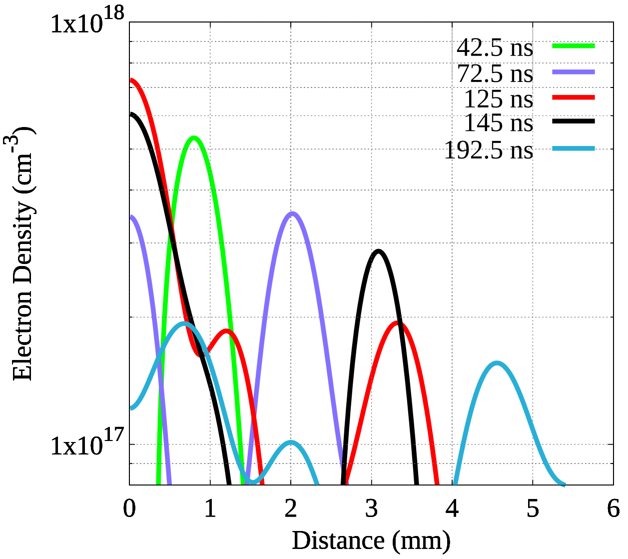

Figure 8.3: Abel inverted interferogram lineouts showing the progress of the shock over time. The lineouts were taken vertically at the zero position marked in Figure 8.2.

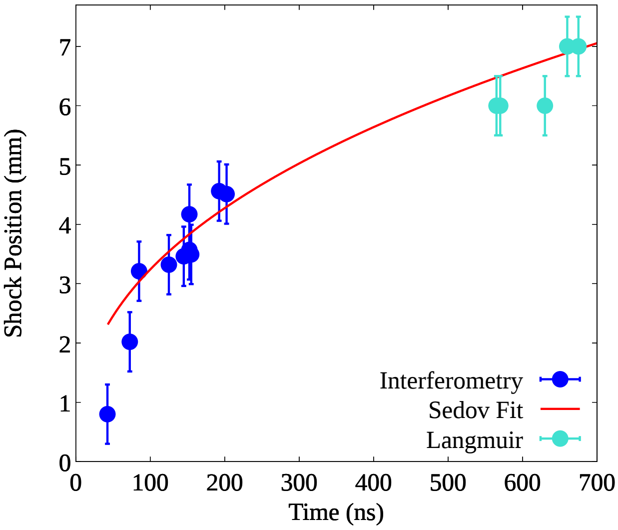

Figure 8.4: *Blue:* Position of shock taken at different times. *Teal:* Arrival of shock according to Langmuir probe signal. *Red:* Sedov-Taylor curve fitted to interferometry and Langmuir probe data. The first two interferometry points are too early and thus omitted in the fit.

the Sedov-Taylor fit to improve the late time characterization of the shock since the interferometric data points are bunched towards early times due to limitations in the vertical field of view. Furthermore, we can estimate the velocity of the shock at the probe tips by taking the first derivative of Eq. 7.21 with respect to time and plugging in the shock arrival time, yielding $v_{\text{flow}} \sim 10\,\text{km/s}$.

8.3 Spectroscopy results

Spatially-resolved emission lines were collected by a spectrometer with a 20μm slit width with varying time delay shot-to-shot to yield information on the evolution of the plasma. The standard method for obtaining the electron temperature for a plasma is to use line ratios, where the lines must have different shapes of cross section. Since our spectra wholly consist of Ar II lines this is not feasible and we must resort to alternative methods using absolutely calibrated spectra (163, 168, 169). Here it is important to note that the spectrometer was whitelight calibrated as described in Chapter 7. The spectrometer's wavelength was calibrated using a mercury pen lamp.

A time-lapse of the spatially-resolved spectra is shown in Figure 8.5. The 0 mm point was set to the target position. The top-left panel is an image of the Langmuir probe (the bright vertical region) and the bdot probe (the horizontal shadow) acquired by the spectrometer with fully opened slit and grating set to zero order. This is a useful reference for seeing where the spectra may be interacting with the probes. The top-right panel is a spectrogram taken $t = 50\,\text{ns}$ after the drive laser was initiated. Significant Ar II spectra extend throughout the space between the target and the probe, suggesting a process of rapid ionization, or preionization, before the shock has had a chance to progress beyond the target. This effect is likely due to photoionization by radiation from the hot, dense plasma at the target, and has been seen in similar experiments (150, 151). In the last four panels of Figure 8.5 the shock position according to the Sedov-Taylor curve is marked by a red, dashed line. This shock position corresponds well with the bright Ar II lines expanding into the preionized background gas.

Abel inversion of the spectra was not possible due to the scattered nature of the acquired data which would have required smoothing techniques, sacrificing

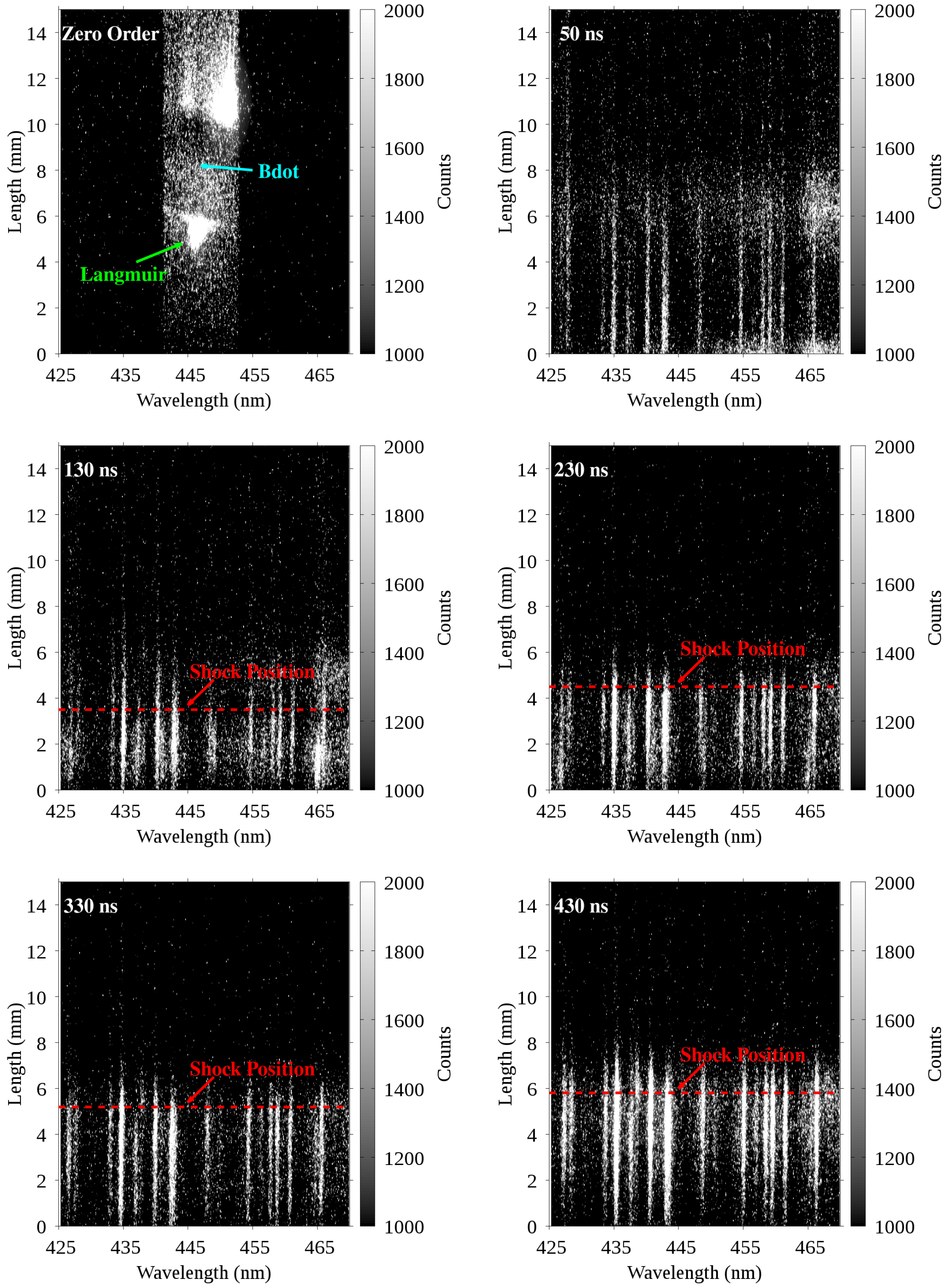

Figure 8.5: Time lapse of spectroscopy figures. Shock position according to the Sedov-Taylor fit from interferometry is marked by the red, dashed line. *Top-left:* Zero order image taken by the spectrometer with the slit fully opened. Here we see the positions of the Langmuir and bdot probes relative to the spatial positions of the spectra. *Top-right:* The shock is not fully developed but we see significant preionization, likely due to photoionization from the hot, dense target.

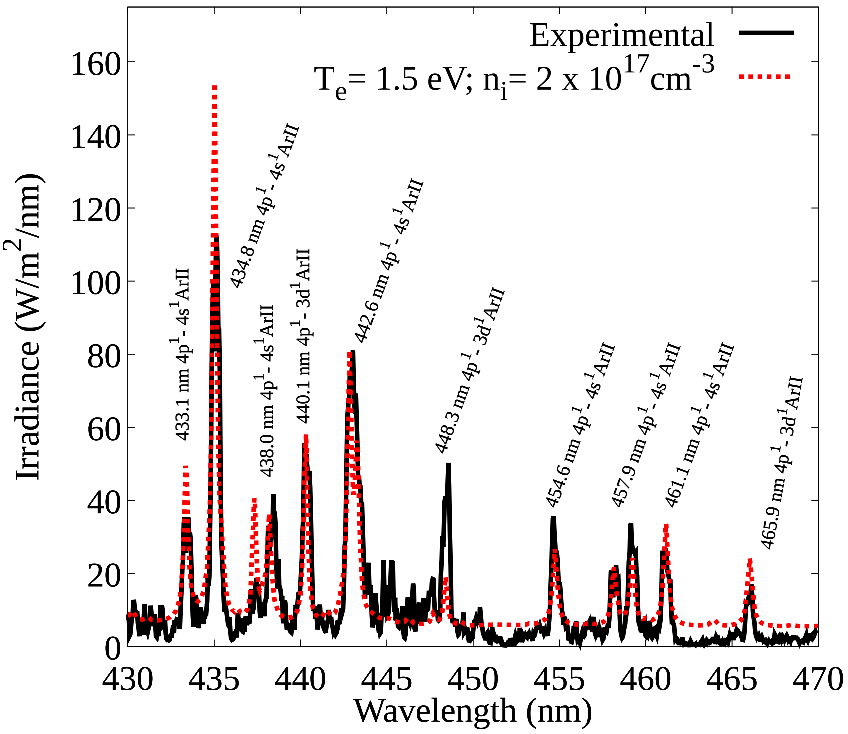

Figure 8.6: Spectroscopy fit at time, t = 380 ns for integrated spectra between position 4.5 mm and 5.4 mm. The fit was simulated using Prismspect with instrument resolution set to $\lambda/\Delta\lambda \sim 2000$, to account for the broadening due to the instrument function.

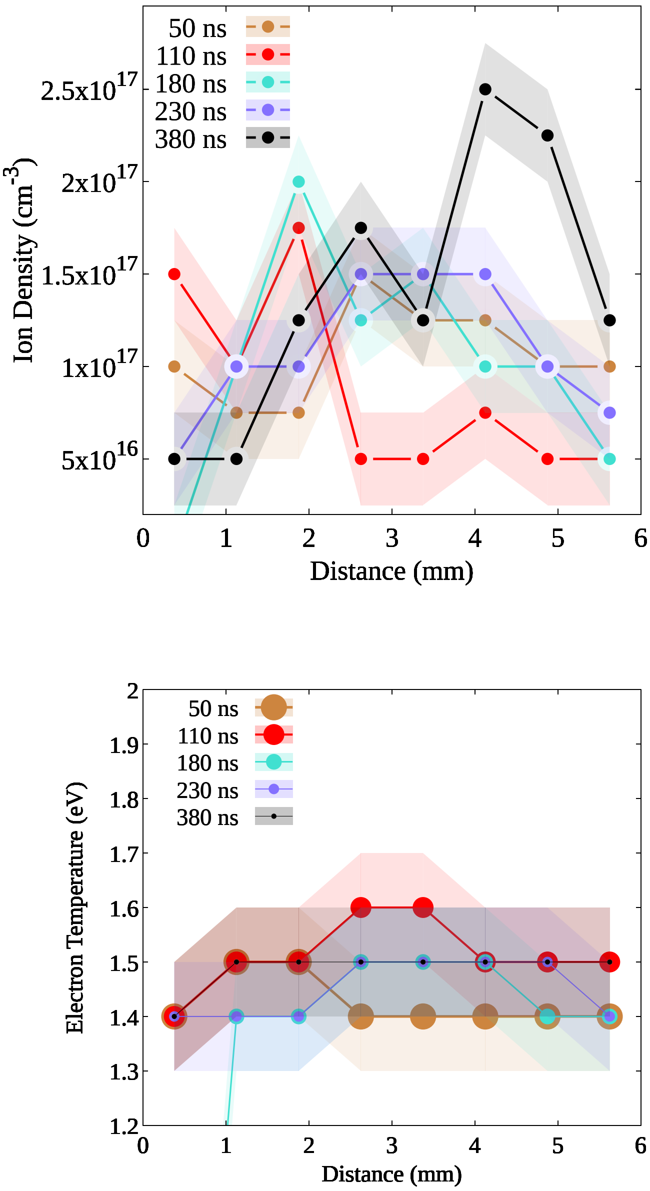

Figure 8.7: Spatially-resolved ion density (top) and electron temperature (bottom) obtained by integrating the spectra at regular spatial intervals. Each curve represents a different time delay from the initial drive laser.

the spectral resolution. Therefore the measured spectra are integrated along the line of sight. Spatially-resolved electron temperature and ion density data were obtained by fitting Prismspect simulations to the calibrated spectra (170). The Prismspect simulations incorporate a resolution parameter which convolves the simulation with a Gaussian function thereby accounting for broadening due to the instrument. In this case, the resolution parameter was estimated from the instrument function in Figure 7.8 to be $\lambda/\Delta\lambda \sim 2000$. An example of the fitted spectra can be seen in Figure 8.6. The Ar II lines were identified using the NIST atomic spectra database (171). The fit generally corresponds well with the measured spectra and the few deviations are likely due to modulations seen in the whitelight calibration in Figure 7.9. The simulations assume a line integrated spectrum along a homogeneous, spherically-distributed plasma with a radial extent of 6 mm.

Spectrograms taken at different delay times were sliced into regular intervals, spatially integrated and then fitted with simulations to yield spatially resolved plasma parameters. The resultant ion densities and electron temperatures are presented in Figure 8.7. We see that $T_e \sim 1.5\,\mathrm{eV}$. Using this temperature we may calculate the Bohm velocity for Argon ions from Eq. 6.21, which comes out to $v_{\mathrm{Bohm}} = 1.9\,\mathrm{km/s}$. Therefore, the shock velocity, as predicted by the Sedov-Taylor curve, is well in excess of the Bohm velocity. Also from Figure 8.7 we see that the ion density is $n_i \sim 1.5 \times 10^{17}\,\mathrm{cm}^{-3}$ which agrees well with interferometry.

8.4 Three-axis bdot results

Prior to carrying out the analysis on the Langmuir probe currents we must check whether our theoretical assumptions are valid. Figure 8.8 shows the magnetic fields measured by the bdot along its three axes. We see that the maximum magnetic field is $B \approx 100$ G. This field is likely generated by misaligned temperature and density gradients in the shock which cause the Biermann battery effect (27). For Argon ions in a flow with $v_{Bohm} \approx 2$ km/s this yields an ion Larmor radius of $r_g \approx 4.2$ cm. Even in this worst case scenario where we have chosen the highest magnetic field and the lowest velocity, the ion Larmor radius is still much larger than the probe tip radius. For electrons, with thermal velocity

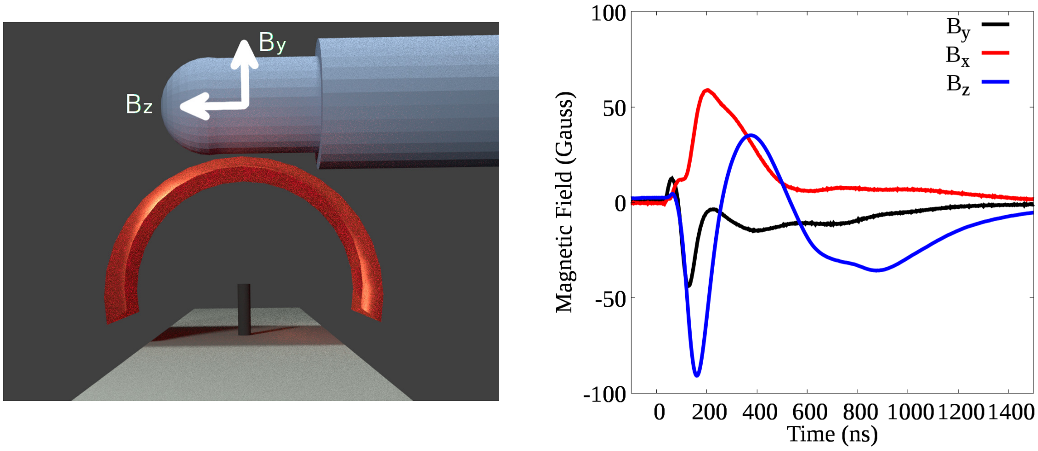

Figure 8.8: *Left:* Schematic showing directions of x, y, and z axes of bdot with respect to the target and expanding shock. The drive laser would be incident on the target from the left side of this figure. *Right:* Example of magnetic fields measured by three-axis bdot on a single shot with bdot core positioned ~ 12 mm above the target.

$v_{th} \sim 500$ km/s the Larmor radius is $r_g = 0.29$ mm which is on par with the probe radius, implying that the electrons are weakly magnetized. In most cases, slight magnetization of the electrons is neglected and only magnetization of ions is deemed to be important (172, 173).

8.5 Langmuir probe results

Now that we have fully characterized the plasma using standard diagnostics, we may proceed to analyze the currents measured by the nanosecond resolution Langmuir probe. To review, we have a fully ionized Argon plasma with an electron density of $n_e \sim 1 \times 10^{17}$ cm^{-3}, and an electron temperature of $T_e \sim 1.5$ eV. The expanding shock approximately follows the Sedov-Taylor model with a flow velocity of $v_{\text{flow}} \sim 10$ km/s which is significantly faster than the Bohm velocity $v_{\text{Bohm}} \sim 2$km/s. Finally, the magnetic fields peak at $B \sim 100$G which corresponds to unmagnetized ions.

Using these plasma parameters, we check for the validity of the thin-sheath

Parameter	***Value***
Debye length (m)	2.9×10^{-8}
electron Larmor radius (m)	2.9×10^{-4}
ion Larmor radius (m)	4.2×10^{-2}
mean free path (m)	5.3×10^{-8}
Knudsen number, bulk	4.3×10^{-4}
Knudsen number, sheath	1.9
Debye number	2.3×10^{-4}
electron Larmor number	2.3
ion Larmor number	3.3×10^{2}

Table 8.1: Plasma parameters describing relevant regimes for $T_e = 1.5$ eV and $n_e = 1 \times 10^{17}$ cm^{-3}

condition and the importance of collisions. The corresponding Debye length, according to Eq. 1.5b, is $\lambda_{De} = 29$ nm. With a probe radius of $r_p = 125\ \mu$m, this results in a Debye number De $= 2.3 \times 10^{-4}$ so the probe is definitely in the thin-sheath regime. The mean free path, as per Eq. 1.19, is $\lambda_{mfp} \sim 53$ nm. The Knudsen number for the bulk of the plasma, that is with respect to the probe radius, is Kn $= 4.3 \times 10^{-4}$ while the Knudsen number for the sheath is Kn $= 1.9$, meaning the quasi-neutral (bulk) region of the plasma is in the continuum regime while the sheath is in the transitional regime, leaning towards the collisonless regime. These parameters are all summarized in Table 8.1. This regime, known as the collisionless thin-sheath dense case, is relatively unexplored in the literature. The most systematic study of this regime was carried out by Tseng and Talbot for the weakly ionized case, wherein one may theoretically separate the fluid and electrical properties of the plasma, and diffusion with respect to a neutral background gas is assumed (145, 174, 175). In our case, the plasma is fully ionized, as witnessed by the strong Ar II lines, and therefore these assumptions, strictly, do not hold. Nonetheless, we will proceed by analyzing the probe currents using the typical Langmuir probe theories to verify whether they may coincidentally hold or whether a heuristic solution can be constructed.

Figure 8.9 shows the three currents measured during a typical shot for this experimental series. For this particular shot, the probe was positioned 6mm away

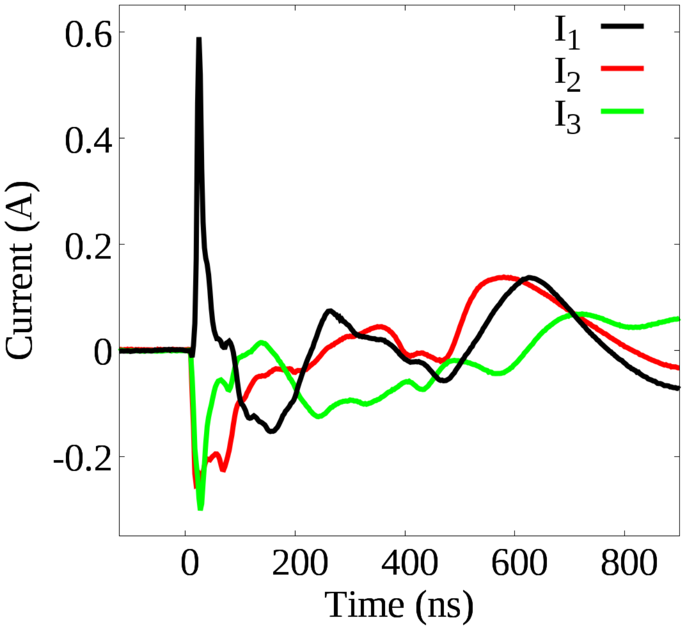

Figure 8.9: Langmuir probe currents measured at a distance of 6 mm from the target with biases set at $\phi_{12} = 1.99$ V and $\phi_{13} = 9.96$ V.

from the target with set biases at $\phi_{12} = 1.99\,\mathrm{V}$ and $\phi_{13} = 9.96\,\mathrm{V}$. These currents were obtained by converting the measured voltage into current through the 50 Ω resistance of the oscilloscope and compensating for the overall gain through the probe and differential amplifier, as measured by the network analyzer. The gain measured by the network analyzer should implicitly contain the gain due to the differential amplifier as well as any attenuation effects through the probe and transmission lines. An additional 10 dB of attenuators were mounted between the oscilloscope and differential amplifier, this was also accounted for explicitly. In Figure 8.9, there is a quick and large signal which can be attributed to either preionization (as seen in the spectrograms at early times) or electrical noise from the laser striking the target. These measured currents, along with another set measured at 7 mm away from the target, will be the focus of our analysis.

8.5.1 Application of collisionless theory

Applying the collisionless theory as given by the set of equations 6.13, results in unrealistically high temperatures or points where the analysis fails altogether. Examining Eq. 6.18, we see that the temperature is sensitive to the ratio of collected currents. In Figure 8.9, the measured currents in tips 1 and 2 are nearly identical, such that $I_{\text{ratio}} = (I_1 - I_2)\,(I_1 - I_3) \approx 0$. The limiting cases of Eq. 6.18 are, as $T_e \rightarrow 0$ the current ratio approaches unity $I_{\text{ratio}} \rightarrow 1$, and when $T_e \rightarrow \infty$ the current ratio approaches $I_{\text{ratio}} \rightarrow \phi_{12}/\phi_{13} \approx 0.2$ A. Therefore, in most regions the temperature cannot be analyzed, and in those regions where it can be analyzed, the temperature will be exponentially large. This eliminates the possibility that the ideal, collisionless, thin-sheath equations, alone, will yield reasonable plasma parameters, consistent with our other diagnostics.

8.5.2 Application of continuum theory

Here we proceed by using the continuum theory of Su and Kiel, described by Eq. 6.15, with the measured plasma parameters to obtain a prediction of the what current should be measured if the continuum theory is applicable to the probe measurements.

Given $n_e \sim 1 \times 10^{17}\,\text{cm}^{-3}$, $T_e \sim 1.5\,\text{eV}$, and assuming $Z \sim 1$ with $T_i = T_e$ the predicted ion saturation current is $I_{i,sat} = 26\,\text{mA}$. This is approximately an order of magnitude lower than what is actually measured by the probe and it is ignoring any cancellation of currents from measuring electrons. Therefore the continuum theory alone is also not applicable.

8.5.3 Application of transition theory

One would expect that since both the collisionless and continuum theories have failed, that perhaps a transition regime approach would work. This assumption is further justified by the fact that as an element of plasma moves towards the probe, it is initially in the collision-dominated quasi-neutral region which must then transition into collisionless free-fall in the sheath region, for a probe in the collisionless dense case (145).

We apply the transitional theory of Thornton, as given by Eq. 6.17 and take the collisionless current I_0 as the ideal collisionless thin-sheath current, given by Eqs. 6.13 and the collisional current I_c as the continuum regime current, given by Eq. 6.15. The resulting ion saturation current is $I_{i,sat} = 26$ mA, same as the continuum theory. This makes sense since the Thornton equation attempts to interpolate between collisional and collisionless theories to obtain values when Kn ~ 1. When the Knudsen number is small (collision-dominated) as it is in the quasi-neutral region, the collision frequency is high, resulting in low particle mobility and low continuum regime current. The large gap between the predicted continuum and collisionless currents means that $I_0 \gg I_c$ and Eq. 6.17 reduces to $I_p \rightarrow I_c$. Therefore, the transition theory cannot account for the currents measured by the probe.

8.5.4 A heuristic approach

Given that neither the collisionless nor collisional theories yield the necessary currents for the plasma parameters as verified by spectroscopy and interferometry we must resort to a heuristic approach. That is, we know what plasma parameters we should be extracting from the Langmuir measurements, so how can we correct the measured currents to obtain consistent values? Looking to other theories, we see that the inclusion of mechanisms, such as collisions or magnetic fields, typically has two effects on the equations. One effect is to change the effective collection area of the probe due to shifts in sheath position. Another effect is to change the ratio of electron to ion current. These are represented as A_s and ζ in Eq. 6.2. The flow speed at the sheath edge, u_s, may also be modulated by supersonic effects.

Initially it was thought that the main deviation from collisionless theory would be due to the large flow velocity dominating over the Bohm velocity. To apply the collisionless theory equations we must account for the increased ion current. This can be done by subtracting the excess current due to the flow, resulting in an effective, stationary current, given by Eq. 6.22a. Such a correction, if applied to all three measured currents, would have no effect on the electron temperature, since it is sensitive to the ratio of the current as seen in Eq. 6.18. It was then assumed that tip 1 would effectively repel the ion current if the energy in the flow is less than the energy of the electrostatic barrier, $e\phi \leq \frac{1}{2}M_i v_{flow}^2$. Unfortunately, the result of this analysis had the opposite of the desired effect. By reducing the magnitude of the ion current in I_2 and I_3 the total currents become larger than that measured by I_1. This would be physically inconsistent with the convention set in chapter 6, that the electron current is positive, the ion current is negative, and therefore the only positively charged probe tip, tip 1, should measure more electrons than the other tips.

Next, a similar approach to the flow compensation idea was tried, but with opposite sign. That is to say, we assume that the magnitude of the ion current is less than what it would be in the collisionless case. Therefore, we artificially increase the magnitude of the ion current measured by tips 2 and 3 and plug these effective currents into the ideal, collisionless thin-sheath equations.

$$I_{2,effective} = I_{2,measured} - I_{inhibited} \tag{8.1}$$

where $I_{inhibited} = AZen_e v_{inhibited}$ and $v_{inhibited}$ is the reduced flow rate of ions compared to Bohm.

It was found that for $v_{\text{inhibited}} = 1.0\,\text{km/s}$ temperatures around $T_e \sim 1\,\text{eV}$ were obtained, consistent with spectroscopy. Unfortunately, with this correction alone, the electron density would be off by a few orders of magnitude. It was decided to modify the effective collection area as this is often impacted by collisional theories. It was found that by changing the effective collection area from $A_{\|}$ to the significantly smaller $A_{\perp}$ densities of $n_e \sim 1 \times 10^{17}$ cm^{-3} were obtained, consistent with interferometry.

The resulting, temporally-resolved plasma parameters are shown in Figure 8.10. The shaded error regions show the sensitivity of the plasma parameters to varying the flow correction around $v_{\text{inhibited}} = 1.0\,(+9.0, -0.5)$ km/s. Here the effects of the flow correction are opposite for the temperature and the density; a larger flow correction maximizes the density while minimizing the temperature, and vice-versa.

Two peaks in electron temperature and plasma potential are seen in Figure 8.10. The second of these two peaks was used in the Sedov-Taylor fit in Figure 8.4

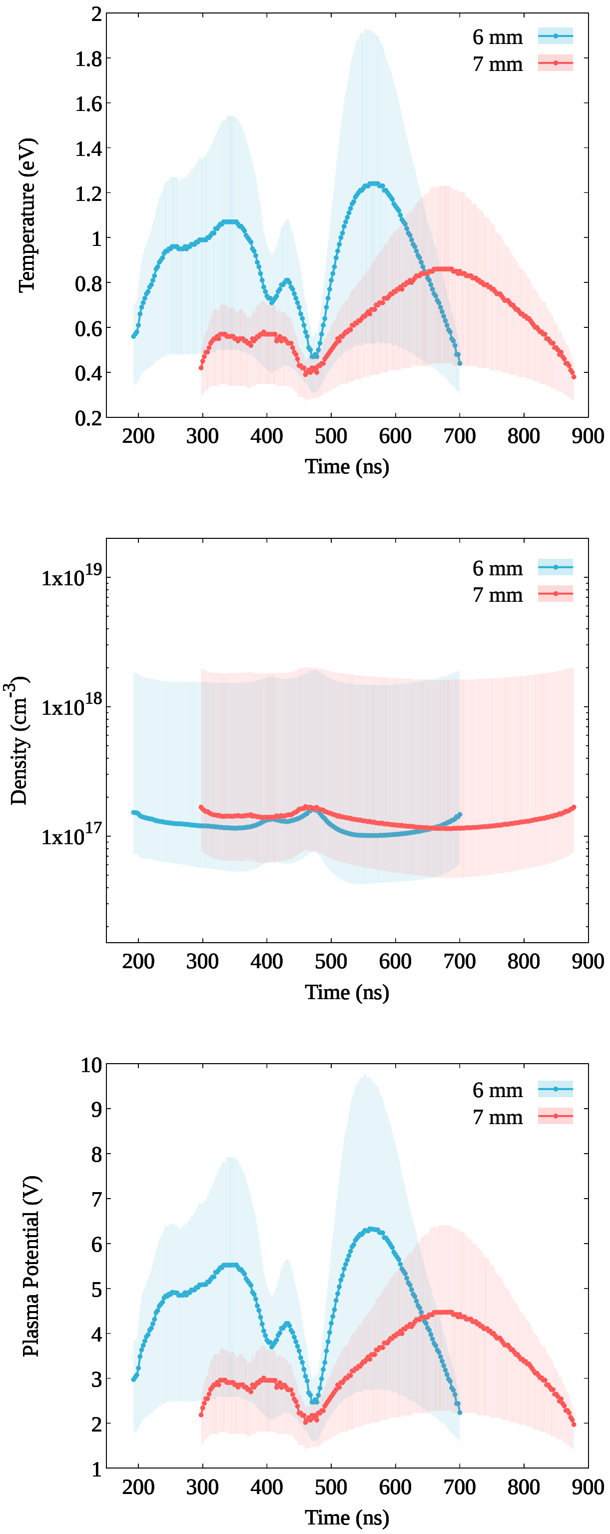

Figure 8.10: Plasma parameters obtained from heuristic method with Langmuir probe at two different distances from the target.

with the idea that the first peak may be a radiative precursor ahead of the real shock. This would be consistent with the strong Ar II lines which are seen ahead of the shock position in Figure 8.5. Another possible explanation for this feature is plume splitting, where an initial shock expands at vacuum velocity which is followed by a second shock expanding at a velocity inhibited by the background plasma (176, 177). It is difficult to confirm this effect since the spatial separation between such peaks would be small compared to the apparent shock thickness at early times and thus not visible in interferometry. But the expanding distance between the shock position and the edge of the Ar II lines ahead of the shock in Figure 8.5 is suggestive of a initial plume expanding faster than the Sedov-Taylor blast wave.

In the process of the analysis it was found that using $A_{||}$ in Eq. 6.13 yielded unrealistic values of electron temperature and density so use of $A_{\perp}$ was attempted which yielded results in accordance with spectroscopy and interferometry. One possible explanation for this is that the flow is so quick that most of the current draw comes from the very tip of the probe and the plasma flowing parallel to the surface of the probe does not have enough time to be accelerated toward the surface. We may check for sheath stability and characteristic collection time of the plasma by using the methods outlined in Doggett *et al* (2005) (151). The time for forming a steady-state Child-Law sheath is $t_c \approx \left(\frac{\sqrt{2}}{9}\right) \omega_{pi}^{-1} \left(\frac{2V_0}{T_e}\right)^{3/4} \sim 20$ ps, where the inverse plasma ion frequency is $\omega_{pi}^{-1} \sim 15$ ps. The collection time scale for ions from the sheath edge is $s_0/u_0 \sim 15$ ps, where s_0 is the sheath thickness and u_0 is the velocity of ions. The time for a plasma element to traverse the length of the probe tip is $L_{probe}/v_{flow} \sim 0.1\ \mu$s. Under these parameters it would seem that there is more than enough time for the ions to be accelerated towards the parallel surface of the probe.

Another possible explanation for the effective collection area is that the supersonic flow when interacting with the probe generates a discontinuity which deflects the bulk of the plasma flow except for at the very tip. It has been shown by Allen (2013) that charged surfaces in a supersonic flow may generate weak discontinuities in the shape of a truncated Mach cone (178). Further work is required to investigate this hypothesis.

The assumption of inhibited flow may be justified by the fact that the quasi-neutral region is collisional. The collisionless assumption of Bohm velocity only works for free-streaming of particles towards the probes, accelerated by small electric fields over distances larger than the sheath thickness. If the particles are colliding, then the flow rate is reduced by forced diffusion, as is seen in the continuum theory. Where the continuum theory fails is when the flowing plasma approaches the transition region between the quasi-neutral and sheath regions, where $\mathrm{Kn} \sim 1$. Here, the collisions are significantly reduced and the particles approach free-fall conditions while in the presence of ever stronger electric fields. The inability to model this complex transition is also why the Thornton theory failed for this case. Future work should focus on solving for the distance of this transition region from the probe and defining it as a boundary layer. Then it should be possible to independently account for the flow rate contributions (or current densities) from the continuum and collisionless regions.

8.6 Conclusion

I have demonstrated the design and analysis of a high temporal resolution current-mode triple Langmuir probe. These probes are suitable for measurement of laser-produced plasmas where supersonic flows are common. Applying the standard theories to the analysis of the probe currents yielded unrealistic plasma parameters. It is possible for plasma parameters measured by the probe to have good agreement with temperatures and densities obtained from emission spectroscopy and interferometry. We have examined a number of different theories and how they may be applied and modified to yield values of temperature and density consistent with interferometry and spectroscopy. In the end, a heuristic approach was used to correct for the effective collection area and proportion of measured currents. These corrections were forced to match the temperature and density measured by spectroscopy and interferometry. This work should be considered a first step towards developing a theory for Langmuir probes in dense, supersonic flows, in that it effectively discounts the usual suspects. That is to say, the purely collisionless, thin-sheath current model as well as the collisional and transition regime models are insufficient for describing dense, supersonic, fully-ionized flows.

Future experimental work should focus on surveying a wider swath of parameter space. Laser energy and gas fill pressure can be adjusted to yield lower or higher density plasmas and move the probe from collisionless to transition to continuum regimes for current collection. Furthermore, extending the probe design to include a fourth, bent tip could enable the measurement of flow velocities as was described by Gatsonis *et al.* with respect to the quadruple, current-mode, probe theory in the collisionless regime (36).

The theory of supersonic plasma flows across Langmuir probes could also benefit from high magnification imaging of the probe tips. Interferometry and spectroscopy with high spatial resolution may confirm structures, such as the weak discontinuity hypothesized by Allen which would explain why the effective collection area turned out to be $A_\perp$ (178). Such observations would also lend themselves to the elaboration of the theory of dusty plasmas.

9

Summary, conclusions, and future work

> *Induction is logically invalid; but refutation or falsification is a logically valid way of arguing from a single counterinstance to — or, rather, against — the corresponding law. This shows that I continue to agree with Hume's negative logical result; but I extend it.*
>
> —Karl Popper, *The Logic of Scientific Discovery (1934)*

9.1 Summary

This thesis has covered two techniques, x-ray Thomson scattering and Langmuir probes, which have proven invaluable in the study of plasmas. These techniques for assessing the temperature and density of a plasma are vitally important in providing an accurate description of relevant mechanisms such as collisionality, sheath effects, as well as equilibrium and non-equilibrium thermodynamic effects. In chapter 3, it was shown that, in theory, macroscopic density gradients can prove to be just as important as microscopic fluctuations in describing the response of a plasma to probing by XRTS. Such gradients can induce an asymmetry in the upshifted and downshifted plasmons in the collective scattering regime, thereby violating detailed balance. The violation of detailed balance is problematic, as it is one of the principle methods for inferring the temperature of a plasma from the scattered spectra. Fortunately, the non-LTE effect of shifting the plasmon intensity ratio towards the blueshifted plasmon can be leveraged to extract information on density gradients in, for example, shocked plasmas.

Chapter 4 described a series of experiments at the OMEGA laser facility for probing warm dense deuterium using XRTS. Prior work had been conducted by Dr. Katerina Falk and Dr. Sean Regan in the non-collective scattering regime, supplemented by measurements using VISAR and SOP. The present work focused on using their refined experimental platform for measuring warm dense deuterium in the collective scattering regime. It was expected that the results of these experiments would be precise measurements of temperature and density which could then be used to test equation of state models for WDM. In this vein, 1D and 2D hydrocode simulations were conducted using two different EOS tables, SESAME and PROPACEOS. These simulations along with prior experimental results were discussed in comparison to the collective scattering measurements acquired on the present experimental campaign, presented in chapter 5. These spectra contained a high intensity upshifted plasmon, on par with the downshifted plasmon intensity, in clear violation of detailed balance. Both homogeneous and inhomogeneous simulations were applied for the dual purpose of checking the consistency in measured plasma parameters and searching for deviations caused by the large gradients when homogeneous XRTS theories are applied in cases where a non-LTE theory is required. The resultant inhomogeneous simulations yielded plasma parameters of $T_e \sim 12\,\mathrm{eV}$, $n_e \sim 4.3 \times 10^{-23} cm^{-23}$ with a gradient scale length of $\Lambda \sim 1.33\,\mathrm{nm}$. It was then shown that this scale length is consistent with the expected shock thickness obtained by mean free path considerations for the measured parameters.

Switching diagnostic methods, chapter 6 discussed the theory and design of a Langmuir probe capable of measuring currents on a nanosecond time-scale. The probe was constructed and measured to have a resolution of 200 MHz which is an order of magnitude greater than typical probe designs. In chapter 7, an experiment was designed for testing this probe against interferometry and spectroscopy to compare the consistency of measured temperature and density values. A three-axis bdot probe was included in the experiment to characterize any possible magnetic effects which can alter the probe current. The experiments consisted of a carbon rod in a 1 mbar background Argon gas, driven by a 2.5 J laser over 10 ns. The sudden deposition of energy resulted in a radially expanding Argon shock following a Sedov-Taylor model, as discussed in chapter 8. Interferometry measured shock densities of $n_e \sim 1 \times 10^{17}\,\mathrm{cm}^{-3}$ near the Langmuir probe, while emission spectroscopy yielded similar ion density values with electron temperatures of $T_e \sim 1.5\,\mathrm{eV}$. Initial analysis of the Langmuir probe currents using the typical collisionless, collisional and transition theories failed, most likely due to the complexity of a dense, collisionless plasma where a plasma element moves from fully collisional to collisionless regime on its path to the probe. It was hypothesized that supersonic flow velocities, significantly larger than the Bohm velocity, could have caused substantial deviations in the measured currents so as to invalidate the application of these theories. A correction for the excess current due to the flow was attempted, with the idea that the resulting effective current could be processed by the ideal collisionless theory. This was not the case, as the flow correction yielded unrealistic current values where the tips which were supposed to be collecting predominately ion saturation current would have had to collect more electron current than the most positively biased probe tip. Finally, a heuristic method where it was assumed that ion currents to tips 2 and 3 were being inhibited, most likely due to collisional effects, was applied. This method yielded temperatures of $T_e \sim 1\,\mathrm{eV}$ and densities of $n_e \sim 1 \times 10^{17}\,\mathrm{cm}^{-3}$, consistent with interferometry and spectroscopy.

9.2 Future work

9.2.1 X-ray Thomson scattering and WDM

For XRTS, further experimental work is required to reproduce and confirm the breakdown of detailed balance in the presence of gradients. Experiments testing for spatial gradients can build off of the experimental platform used at OMEGA, but require a few improvements. One important improvement would be to increase the scattered signal by using a higher intensity backlighter. A volumetric backlighter to replace the planar backlighter is currently under investigation. The inhomogeneous XRTS theory also predicts that effects should be seen in the presence of large temporal gradients as well. Such temporal gradients may be found in experiments examining the disassociation and re-association of plasmas and may provide a measure of the rates of these fast processes.

In the present work, the inhomogeneous theory was applied solely to the free electron term of the dynamic structure factor. This can be readily extended to the ion feature for situations where the ion feature may be formulated in terms of the dielectric response function. Furthermore, the screening term $q(k)$ of the ion component is a function of the free electron dynamic structure factor, which can be readily implemented with the theory as is. In addition, extensions to strongly coupled regimes may be advanced through the use of local field corrections, which would simply include derivatives with respect to the wavenumber k of the correction parameter $G(k)$.

9.2.2 Langmuir probes

Future experiments should focus on collecting Langmuir probe currents at various Knudsen numbers to explore theories describing the dense probe case. This can be supplemented with high magnification interferometry and spectroscopy to image the plasma regions closest to the probe tips. Here it may be useful to investigate transition regime theories to construct a model for how the plasma moves from the collisional case in the bulk region to the collisionless case in the sheath region. Care must be taken, as the only known investigations of the dense case, those of Talbot, describe a theory for weakly ionized plasmas, whereas in laser produced plasmas one is more likely to encounter multiply-ionized species.

Further theoretical work needs to be done in the collisionless thin sheath dense case. The basic components already exist, namely the collisionless, continuum and transition theories, one just needs to find a technique to apply all three simultaneously in a coherent fashion. One approach could be to solve for the stand-off distance of the transition region from the probe and define this as a boundary layer. Then the velocity outside of this layer is defined by the forced diffusion model, while the acceleration under this layer is described by free-fall. Such a methodology should yield an effective velocity which is less than the collisionless velocity, but greater than the continuum velocity, which would be consistent with the inhibited current heuristic used in experimental results in chapter 8.

Once the theory for how to analyze the currents from a probe in the collisionless dense case is established, future work should be aimed at applying the probe to novel scenarios. For example, using the probe to measure fluctuations in temperature and density in turbulent plasmas can be used to obtain a measure of the turbulent energy. This would be especially useful for studies of amplification of magnetic fields through turbulent dynamo effects since the turbulent energy can then be compared to the increase in magnetic energy. It may be possible to examine and compare the spectrum of thermodynamic fluctuations to magnetic fluctuations as well.

Another interesting application would be in Stark broadening experiments. Stark broadening measurements continue to be investigated in regimes accessible to this Langmuir probe, namely $n_e \sim 1 \times 10^{17}\,\mathrm{cm}^{-3}$ with $T_e \sim 1\,\mathrm{eV}$. The probe may prove to be a useful diagnostic for confirming the temperature and density of a plasma produced for investigating Stark broadening.

Appendix A

Publications

Peer Reviewed Publications

1. P. M. Kozlowski, B. J. B. Crowley, D. O. Gericke, S. P. Regan, G. Gregori. Theory of Thomson scattering in inhomogeneous media. *Scientific reports*, 6 (2016).

2. P. M. Kozlowski, M. Oliver, G. Gregori. Design, construction, and characterization of a near-nanosecond resolution Langmuir probe as a diagnostic for laser-produced shocks in plasmas. (to be submitted 2016)

3. P. X. Belancourt, W. Theobald, P. A. Keiter, T. J. B. Collins, M. K. Bonino, P. M. Kozlowski, S. P. Regan, R. P. Drake. Demonstration of Imaging X-ray Thomson Scattering on OMEGA EP. *Rev. Sci. Instrum.*, 87, 11 (2016)

Talks and Posters

1. Poster on *Nanosecond Langmuir Probes for the Resolution of Plasma Properties of Shocks in Laboratory Astrophysics* at 3rd High Power Laser Workshop, SLAC, Stanford, California (2015)

2. Oral presentation on *Nanosecond Langmuir Probes for the Resolution of Plasma Properties of Shocks in Laboratory Astrophysics* at 5th International

Conference on High Energy Density Physics (ICHED), San Diego, USA (2015)

3. Oral presentation on *Diagnosing Density Spatial Gradients using Higher Order Corrections for X-ray Thomson Scattering* at ICF Ignition Sessions Workshop, Wolfson College, Oxford, UK (2015)
4. Oral presentation on *Diagnosing Density Spatial Gradients using Higher Order Corrections for X-ray Thomson Scattering* at 13th International Workshop on the Fast Ignition of Fusion Targets, The Queen's College, Oxford, UK (2014)
5. Poster on *X-ray Thomson Scattering Measurements of Density Gradients* at 2nd High Power Laser Workshop, SLAC, Stanford, California (2014)
6. Poster on *X-ray Thomson Scattering Measurements of Density Gradients* at Omega Laser Facility Users Group Workshope (OLUG), Rochester, New York (2014)
7. Poster on *X-ray Thomson Scattering Measurements of Density Gradients* at Institute of Physics - Plasma physics group Spring conferece, London, UK (2014)
8. Oral presentation on *Inhomogeneous Thomson Scattering* at Oxford Centre for High Energy Density Science Annual Meeting (OxCHEDS), Oxford, UK (2014)
9. Poster on *X-ray Thomson Scattering Measurements of Density Gradients* at Nation Ignition Facility (NIF) user group meeting, Livermore, California (2014)
10. Poster on *High Density and Temperature Diagnostics for Laboratory Astrophysics* at Nation Ignition Facility (NIF) user group meeting, Livermore, California (2013)

Appendix B

Acronyms, symbols, and constants

Table of acronyms

Acronym	Definition
AC	Alternating Current
AM	Amplitude Modulation
ASBO	Active Shock BreakOut
CAD	Computer Aided Design
CCD	Charge-Coupled Device
CID	Charge Injection Device
CPA	Chirped Pulse Amplification
CRYO	CRYOgenic
CTHS	Cryogenic Target Handling System
DC	Direct Current
DFT-MD	Density Functional Theory Molecular Dynamics
DSF	Dynamic Structure Factor
FCC	Frequency Conversion Crystal
FDT	Fluctuation-Dissipation Theorem
FFA	Form Factor Approximation
FFT	Fast Fourier Transform
FOV	Field Of View
FTM	Fourier Transform Method
FWHM	Full Width at Half Maximum
GTS	Gated Thomson Spectrometer
HEDP	High Energy Density Physics
HF	Hartree-Fock
HNC	Hyper-Netted Chain
HOPG	Highly Oriented Pyrolytic Graphite
HWHM	Half Width at Half Maximum
IA	Impulse Approximation
ICF	Inertial Confinement Fusion
IDEA	Interferometric Data Evaluation Algorithms
IFFT	Inverse Fast Fourier Transform
I-V	Current-Voltage

Table of acronyms (cont.)

Acronym	Definition
LCLS	Linac Coherent Light Source
LFC	Local Field Correction
LLE	Laboratory for Laser Energetics
LP	Langmuir Probe
LTE	Local Thermodynamic Equilibrium
LTSpice	Linear Technology Spice
Ly-α	Lyman alpha
MCP	Micro-Channel Plate
mfp	mean free path
ND	Neutral Density
OCP	One Component Plasma
PDS	Photometric Data System
PIMC	Path Integral Monte Carlo
PROPACEOS	PRism OPACity and Equation of State
RbAp	Rubidium Acid Phthalate
RF	Radio Frequency
RPA	Random Phase Approximation
SACLA	Spring-8 Angstrom Compact free electron LAser
SCF	Self-Consistent Field
SOCP	Screened One Component Plasma
SOCPN	Screened One Component Plasma Negative
SOP	Streaked Optical Pyrometry
SP	Stewart-Pyatt
SRF	Shot Request Form
SSC	SIM Streak Camera
TCC	Target Chamber Center
TF	Thomas-Fermi
TIM	Ten Inch Manipulator
TPS	Target Positioning System
TTL	Transistor-Transistor Logic
TVS	Target Viewing System
UV	UltraViolet

Table of acronyms (cont.)

Acronym	Definition
VISAR	Velocity Interferometer System for Any Reflector
VNA	Vector Network Analyzer
WDM	Warm Dense Matter
XFEL	X-ray Free Electron Laser
XRFC	X-Ray Framing Camera
XRPHC	X-Ray Pin Hole Camera
XRS	X-Ray Scatter
XRTS	X-ray Thomson Scattering

Table of symbols

Symbol	Definition
A	Area
$A_z(p \to q)$	Einstein's coefficient for transition from level p to q in state z
$A_{\|\|}$	Parallel surface area
$A_{\perp}$	Perpendicular surface area
a	Area of coil
$a_{\alpha,\beta}$	Inter-particle separation between α and β
B	Magnetic Field
b	Impact parameter
$c(r)$	Correlation function
D	Diffusion coefficient
$D_i(r,t)$	Electric displacement field
d	inter-particle spacing or inter-lattice spacing
d_s	Sheath thickness
$\mathbf{E}$	Electric field
E_C	Compton recoil energy
E_F	Fermi Energy
E_{int}	Internal energy
E_{jk}	Energy to move electron from level j to k
E_L	Laser energy
$E_z(p)$	Energy of level p in state z
E_0	Incident photon energy
$\mathscr{F}$	Transformation operator of process
f	Focal length
$f(r)$	True radial distribution of plasma property
$f(v)$	Velocity distribution function
$f_I(k)$	Distribution of tightly bound electrons
$G(r,t)$	Density-density correlation function
g	Gaunt factor or Gain
g_j	Statistical weight of energy level j
$g_z(p)$	Degeneracy parameter of level p in state z

Table of symbols

Symbol	Definition
$g(r)$	Pair distribution function
$h(r)$	Pair correlation function
$h(y)$	Projection of radially symmetric plasma property
I	Current
I_c	Collisional current
I_{sat}	Saturation current
I_0	Collisionless current
I_1	Current collected by tip 1
$I_{\|\|}$	Current to probe oriented parallel to flow
J	Current density
J_{e0}	Electron thermal current density
J_{i0}	Ion thermal current density
Kn	Knudsen number
$\mathbf{k}$	Wavevector
$\mathbf{k_0}$	Incident wavevector
$\mathbf{k_1}$	Scattered wavevector
k	Wavenumber
k_{De}	Debye wavenumber
L	Distance
L_s	Self-inductance
ℓ	Plasma thickness
M	Mutual inductance
m_α	Mass of species α
N	Number of particles or Number or turns in coil
n	Refractive index or Energy level
n_c	Critical density
n_e	Electron density
P	Pressure
P_{ff}	Free-free Bremmstrahlung emission power
$\mathbf{p}$	Momentum vector
$p(r)$	Density-density correlation function
q	Electric charge
$q(k)$	Screening function

Table of symbols

Symbol	Definition
R	Resistance
R_{crystal}	Integrated reflectivity
$\mathbf{r}$	Inter-particle distance
r	Radius or Internal resistance
r_g	Larmor (gyro-) radius
r_s	Wigner-Seitz parameter
$S\left(k\right)$	Static form factor
$S\left(\mathbf{k},\omega\right)$	Dynamic structure factor
$S_{ce}\left(\mathbf{k},\omega\right)$	Bound-free dynamic structure factor
$S_{DH}\left(\mathbf{k},\omega\right)$	Debye-Hückel dynamic structure factor
$S_{ee}\left(\mathbf{k},\omega\right)$	Electron-electron dynamic structure factor
$S^0_{ee}\left(\mathbf{k},\omega\right)$	Free electron-electron dynamic structure factor
$S_{ei}\left(\mathbf{k},\omega\right)$	Electron-ion dynamic structure factor
$S_{ii}\left(\mathbf{k},\omega\right)$	Ion-ion dynamic structure factor
$S_s\left(\mathbf{k},\omega\right)$	Self-motion dynamic structure factor
$S_{\text{sum}}\left(\mathbf{k},\omega\right)$	Summation method dynamic structure factor
S_{11}	Scatter parameter input port 1 and output port 1
S_{21}	Scatter parameter input port 1 and output port 2
s	Fringe shift
T_α	Temperature of species α
T_e	Electron temperature
T_F	Fermi temperature
T_i	Ion temperature
t_c	Child-Law sheath formation time
$U_z\left(T\right)$	Partition function
u_s	Velocity at sheath
V	Volume or Voltage
V_k	Fourier transform of Coulomb potential
$V_{meas}\left(\omega\right)$	Measured voltage at frequency ω
$V_{ref}\left(\omega\right)$	Reference voltage at frequency ω
v_{Bohm}	Bohm velocity
v_{flow}	Flow velocity
v_{th}	Thermal velocity
$v_\perp$	Perpendicular velocity

Table of symbols

Symbol	Definition
y	Distance
Z	Average ionization or Impedance
Z_c	Number of core electrons per atom
Z_f	Number of free electrons per atom
α	Scatter parameter or Geometry Factor
$\Gamma_{\alpha,\beta}$	Coupling parameter between α and β
δ	Dirac delta function
ϵ_{ij}	Dielectric tensor
$\epsilon\left(\mathbf{k},\omega\right)$	Dielectric response function
$\epsilon_z\left(p \rightarrow q\right)$	Emission coefficient for transition from level p to q in state z
ζ	Proportion of collected particles
η_{att}	Attenuation factor
η_d	Detector efficiency factor
η_x	Conversion efficiency
Θ	Degeneracy parameter
θ	Scatter angle
θ_B	Bragg angle
Λ	Gradient scale length (spatial)
Λ_e	Thermal de Broglie wavelength of an electron
λ_{De}	Debye screening length
λ_{ee}	Electron-electron mean free path
λ_{ie}	Ion-electron mean free path
λ_{ii}	ion-ion mean free path
λ_{mfp}	Mean free path length
λ_{pq}	Wavelength of transition from p to q
λ_s	Screening length
λ_{TF}	Thomas-Fermi screening length
μ	Chemical potential or Permeability
μ_α	Mobility of particle α
μ'	Real component of magnetic permeability
μ''	Imaginary component of magnetic permeability
$(\mu - 1)$	Refractivity
ν_{ii}	Ion-ion collision frequency
ξ_0	Similarity variable

Table of symbols

Symbol	Definition
$\rho\left(\mathbf{r}\right)$	Electron density operator
$\rho^0\left(\mathbf{r}\right)$	Non-interacting electron density operator
$\rho\left(\mathbf{r}\right)_{\mathbf{k}}$	Electron density operator in Fourier space
Σ_j	Summation over all cells indexed by j
σ	Cross-section or standard deviation
σ_T	Thomson cross-section
τ	Gradient scale length (temporal) or Time delay
τ_p	Plasma frequency time scale
τ_s	Inductance time
ϕ	Electric potential
ϕ_f	Floating potential
ϕ_p	Probe potential
ϕs	Plasma (space) potential
ϕ_{ps}	Electric potential between space (plasma) and probe
ϕ_{s1}	Electric potential between space (plasma) and tip 1
χ	Electric susceptibility
χ_p	Non-dimensionalized potential
Ω	Solid angle
ω	Angular frequency (of a wave)
ω_p	Plasma frequency

Table B.1: Note that bold symbols are vector quantities.

Table of constants

Constant	Symbol	Value	Units
Speed of light in vacuum	c	2.99792×10^{8}	m/s
Vacuum permittivity	ϵ_0	8.85419×10^{-12}	F/m
Vacuum permeability	μ_0	$4\pi \times 10^{-7}$	$\mathrm{N/A^2}$
Electron charge	e	1.60218×10^{-19}	C
Electron mass	m_e	9.10938×10^{-31}	kg
Planck's constant	h	6.62607×10^{-34}	$\mathrm{J \cdot s}$
Reduced Planck's constant	$\hbar$	1.05457×10^{-34}	$\mathrm{J \cdot s}$
Boltzmann's constant	k_B	1.38065×10^{-23}	J/K
Pi	π	3.14159	
Imaginary number	i or j	$\sqrt{-1}$	
Hydrogen Ionization Energy	E_H	13.6	eV
Thomson cross section	σ_t	6.65246×10^{-29}	$\mathrm{m^2}$
Bohr radius	a_0	5.29177×10^{-11}	m

Appendix C

XRTS input deck

Here is an example of the input deck used in Gianluca Gregori's XRS code. You can see the parameters used for simulating x-ray Thomson scattered spectra in a plasma with spatial gradients. Output from this code was then post-processed by convolving the simulated spectra with the instrument function using a Python script.

```
--XRTS---input_file-----------------------------------
--
--fit_parameters------------------------------flag----
DO_FIT  0
PHOTON_ENERGY  2960
SCATTERING_ANGLE  40
ELECTRON_TEMP  12 0
ELECTRON_DENSITY 4.3e23 0
AMPLITUDE  1.0  0
BASELINE  0.0  0
Z_FREE  1.0 0
OUT(1=XSEC,2=PWR) 2
--model_for_total_spec---------use-flag--------------
USE_RPA 0
USE_LINDHARD 0
USE_TSYTOVICH 0
USE_STATIC_LFC 0
USE_DYNAMIC_LFC 0
```

```
USE_MFF 0
USE_BMA 0
USE_BMA+sLFC 0
USE_CORE 1
--gradients------------------------------------------
GRAD 1
L_GRADIENT -1.33e-9
T_GRADIENT  1.0
DSTEP 1.0E-4
--ion_parameters----------------------------use_flag-
ION_TEMP 0 0
S_ION_FEATURE 1.000000 0
DEBYE_TEMP -1 0
BAND_GAP 4.0 0
--integration----------------------------------------
N_DAWSON 32
N_DISTRIBUTION 32
N_PVI 32
N_LANDEN 512
N_RELAXATION 1024
N_FFT 4096
EPS 1.0E-4
--See(k,w)------------------------------use/norm-----
STATIC_MODEL(DH,OCP,SOCP,SOCPN) SOCP
USE_ADV_MIX  1
USE_IRS_MODEL  0
HARD_SPHERE_DIAM  1E-10 0
POLARIZABILITY  0.0 0.0
BOUND-FREE_MODEL(IA,IBA,FFA)  FFA
BOUND-FREE_NORM(FK,NO,USR)  NO  0
BOUND-FREE_MEFF 1.0
USE_BOUND-FREE_DOPPLER          0
CONT-LOWR_MODEL(SP,EK,USR)  SP 1
GK  1.5 0
RPA  1 0
LINDHARD  0 0
```

```
SALPETER  0 0
LANDEN  0 0
RPA_TSYTOVICH  0 0
STATIC_LFC  0 0
DYNAMIC_LFC  0 0
MFF  0 0
BMA(+sLFC)  0 0
CORE  0 0
TOTAL  1 0
E_MIN  -100
E_MAX  100
E_STEP  0.1
--target_spec--------------------------chem----Zfree--
NUMBER_OF_SPECIES 1
TARGET_1 H 1 -1
MASS_DENSITY 0.8
NE_ZF_LOCK 0
DATA_FILE 35082_s2_h.txt
NUMBER_POINTS 320
OPACITY_FILE nofile 0
--instrument_function---------------------------------
USE_FILE 0
FILE_NAME ../instrum2.txt
INST_MODEL GAUSSIAN
INST_FWHM 5.0
BIN_PER_PIXEL 1.0
INST_INDEX 2.0
--additional_parameters-------------------------------
MAX_ITERATIONS 0
LEVENBERG_MARQUARDT 0
SIGMA_LM 1.0
SAVE_FILE 31.txt
```

References

[1] S. J. Blundell, K. M. Blundell. *Concepts in Thermal Physics*, (Oxford University Press2009), 2nd edn. ISBN 978-0199562107. 2, 6, 11, 23

[2] S. Ichimaru. Strongly coupled plasmas: high-density classical plasmas and degenerate electron liquids. *Reviews of Modern Physics*, **54**(4), 1017 (1982). 2, 9, 21, 28, 29

[3] S. H. Glenzer, R. Redmer. X-ray Thomson scattering in high energy density plasmas. *Reviews of Modern Physics*, **81**(4), 1625 (2009). 4, 14, 25, 29, 30, 34, 65, 69, 70, 90

[4] F. Chen Francis. *Introduction to plasma physics*, (Springer, New York1974). 4, 6, 9

[5] S. Eliezer, A. K. Ghatak, H. Hora, A. Ghatak. *Fundamentals of equations of state*. 1, (World Scientific2002). 4

[6] R. P. Drake. *High energy density physics*, (Springer2006), 1st edn. ISBN 978-3540293149. 4, 38

[7] B. A. Remington, R. P. Drake, D. D. Ryutov. Experimental astrophysics with high power lasers and Z pinches. *Reviews of Modern Physics*, **78**(3), 755 (2006). 5

[8] A. P. Jephcoat. High-pressure physics: Testing one's metal. *Nature materials*, **10**(12), 904 (2011). 5

[9] F. Graziani, M. P. Desjarlais, R. Redmer, S. B. Trickey. *Frontiers and Challenges in Warm Dense Matter*, vol. 96, (Springer Science & Business2014). 5, 12

[10] K. Falk, S. Regan, J. Vorberger, M. Barrios, T. Boehly, *et al.* Self-consistent measurement of the equation of state of liquid deuterium. *High Energy Density Physics*, **8**(1), 76 (2012). 5

[11] P. Celliers, G. Collins, D. Hicks, J. Eggert. Systematic uncertainties in shock-wave impedance-match analysis and the high-pressure equation of state of Al. *Journal of applied physics*, **98**(11), 113529 (2005). 5

[12] G. Collins, L. Da Silva, P. Celliers, D. Gold, M. Foord, *et al.* Measurements of the equation of state of deuterium at the fluid insulator-metal transition. *Science*, **281**(5380), 1178 (1998). 5

[13] S. Ichimaru. *Basic Principles of Plasma Physics*, (Addison-Wesley1973), 1st edn. ISBN 978-8189938178. 6, 7, 8, 20, 23, 26, 27, 28, 40, 42, 45

[14] A. Höll, T. Bornath, L. Cao, T. Döppner, S. Düsterer, *et al.* Thomson scattering from near-solid density plasmas using soft x-ray free electron lasers. *High Energy Density Physics*, **3**(1), 120 (2007). 6

[15] W. L. Kruer. *The physics of laser plasma interactions*, (Addison-Wesley Publishing Co.1988). 7, 65, 67, 80

[16] D. Froula, S. H. Glenzer, N. C. Luhmann, J. Sheffield. *Plasma scattering of electromagnetic radiation*, (Academic Press2010), 2nd edn. ISBN 978-0123748775. 8, 30, 38, 39, 92

[17] D. O. Gericke, J. Vorberger, K. Wünsch, G. Gregori. Screening of ionic cores in partially ionized plasmas within linear response. *Physical Review E*, **81**(6), 065401 (2010). 9, 25

[18] A. Kumar, R. Singh, J. Thomas, S. Sunil. Parametric study of expanding plasma plume formed by laser-blow-off of thin film using triple Langmuir probe. *Journal of Applied Physics*, **106**(4), 043306 (2009). 9, 14

[19] Y. B. Zel'dovich, Y. P. Raizer. *Physics of Shock Waves and High-Temperature Hydrodynamic Phenomena*, vol. 1 (Academic Press). 10, 147, 151

[20] V. Demidov, S. V. Ratynskaia, K. Rypdal. Electric probes for plasmas: The link between theory and instrument. *Review of scientific instruments*, **73**(10), 3409 (2002). 10, 12, 14, 102

[21] P. Glansdorff, I. Prigogine. *Thermodynamic theory of structure, stability and fluctuations*, (John Wiley & Sons1971). 11

[22] D. Kondepudi, I. Prigogine. *Modern thermodynamics: from heat engines to dissipative structures*, (John Wiley & Sons2014). 11

[23] T. Fujimoto. *Plasma spectroscopy*, vol. 123, (Oxford University Press2004). 11, 135, 136

[24] R. Tolman. *The principles of statistical mechanics*, (Oxford University Press1938). 11

[25] P. M. Kozlowski, B. J. B. Crowley, D. O. Gericke, S. P. Regan, G. Gregori. Theory of Thomson scattering in inhomogeneous media. *Scientific reports*, **6** (2016). 12

[26] H. Lin, G. Li, R. D. Bengtson, C. P. Ritz, H. Tsui. A comparison of Langmuir probe techniques for measuring temperature fluctuations. *Review of scientific instruments*, **63**(10), 4611 (1992). 12

[27] J. Meinecke, H. Doyle, F. Miniati, A. Bell, R. Bingham, *et al.* Turbulent amplification of magnetic fields in laboratory laser-produced shock waves. *Nature Physics*, **10**(7), 520 (2014). 12, 158

[28] D. Ryutov, B. Remington, H. Robey, R. Drake. Magnetohydrodynamic scaling: from astrophysics to the laboratory. *Physics of Plasmas (1994-present)*, **8**(5), 1804 (2001). 12

[29] J. E. Cross, B. Reville, G. Gregori. Scaling of magneto-quantum-radiative hydrodynamic equations: From laser-produced plasmas to astrophysics. *The Astrophysical Journal*, **795**(1), 59 (2014). 12

[30] K. Falk. *Measurement of Equation of State of Compressed Hydrogen and Deuterium*. Ph.D. thesis, Oxford University (2011). 13, 62, 64, 65, 80

[31] S. Regan, K. Falk, G. Gregori, P. Radha, S. Hu, *et al.* Inelastic x-ray scattering from shocked liquid deuterium. *Physical review letters*, **109**(26), 265003 (2012). 13, 15, 69, 79, 80, 91, 94

[32] K. Falk, S. Regan, J. Vorberger, B. Crowley, S. Glenzer, *et al.* Comparison between x-ray scattering and velocity-interferometry measurements from shocked liquid deuterium. *Physical Review E*, **87**(4), 043112 (2013). 13, 50

[33] F. F. Chen. Langmuir probe diagnostics. In *IEEE-ICOPS Meeting, Jeju, Korea* (2003). 14, 100, 113

[34] R. L. Merlino. Understanding Langmuir probe current-voltage characteristics. *American Journal of Physics*, **75**(12), 1078 (2007). 14

[35] S.-L. Chen, T. Sekiguchi. Instantaneous direct-display system of plasma parameters by means of triple probe. *Journal of Applied Physics*, **36**(8), 2363 (1965). 14, 101

[36] N. A. Gatsonis, L. T. Byrne, J. C. Zwahlen, E. J. Pencil, H. Kamhawi. Current-mode triple and quadruple Langmuir probe methods with applications to flowing pulsed plasmas. *IEEE transactions on plasma science*, **32**(5), 2118 (2004). 14, 16, 99, 101, 104, 106, 168

[37] R. Modolo, J.-E. Wahlund, R. Boström, P. Canu, W. Kurth, *et al.* Far plasma wake of Titan from the RPWS observations: A case study. *Geophysical Research Letters*, **34**(24) (2007). 14, 99

[38] B. Cherrington. The use of electrostatic probes for plasma diagnosticsa review. *Plasma chemistry and plasma processing*, **2**(2), 113 (1982). 14, 99

[39] T. Yamada, J. Kim, M. Ishihara, M. Hasegawa. Low-temperature graphene synthesis using microwave plasma CVD. *Journal of Physics D: Applied Physics*, **46**(6), 063001 (2013). 14, 99

[40] J. Kallman, M. Jaworski, R. Kaita, H. Kugel, T. Gray. High density Langmuir probe array for NSTX scrape-off layer measurements under lithiated divertor conditionsa). *Review of Scientific Instruments*, **81**(10), 10E117 (2010). 14, 99

[41] S. C. Hsu, P. M. Bellan. A laboratory plasma experiment for studying magnetic dynamics of accretion discs and jets. *Monthly Notices of the Royal Astronomical Society*, **334**(2), 257 (2002). 14, 99

[42] G. Gregori. Graduate Class in Plasma Physics: Statistical Theory and Strongly Coupled Plasmas (2009). 20, 22, 26, 28, 35

[43] J.-P. Hansen, I. R. McDonald. *Theory of simple liquids*, (Academic Press2006). 20

[44] J. Vorberger, I. Tamblyn, B. Militzer, S. Bonev. Hydrogen-helium mixtures in the interiors of giant planets. *Physical Review B*, **75**(2), 024206 (2007). 22, 31

[45] J. Vorberger, I. Tamblyn, S. A. Bonev, B. Militzer. Properties of Dense Fluid Hydrogen and Helium in Giant Gas Planets. *Contributions to Plasma Physics*, **47**(4-5), 375 (2007). 22, 31

[46] B. Holst, R. Redmer, M. P. Desjarlais. Thermophysical properties of warm dense hydrogen using quantum molecular dynamics simulations. *Physical Review B*, **77**(18), 184201 (2008). 22, 31

[47] J. Chihara. Difference in x-ray scattering between metallic and non-metallic liquids due to conduction electrons. *Journal of Physics F: Metal Physics*, **17**(2), 295 (1987). 23

[48] R. W. James. *The Optical Properties of the Diffraction of X-rays. The Crystallline State Vol 2.*, (G. Bell1954). 25

[49] D. Pines. *Elementary Excitations in Solids: Lectures on Protons, Electrons, and Plasmons, Advanced Book Program*, (Perseus Books1999). 25

[50] G. Gregori, S. H. Glenzer, W. Rozmus, R. Lee, O. Landen. Theoretical model of x-ray scattering as a dense matter probe. *Physical Review E*, **67**(2), 026412 (2003). 25, 27, 28, 31

[51] K. Wünsch, J. Vorberger, M. Schlanges, D. O. Gericke. Ion structure for x-ray Thomson scattering in dense fusion plasmas. In *Journal of Physics: Conference Series*, vol. 112, 032077, (IOP Publishing2008). 26

[52] K. Wünsch, P. Hilse, M. Schlanges, D. O. Gericke. Structure of strongly coupled multicomponent plasmas. *Physical Review E*, **77**(5), 056404 (2008). 26

[53] V. Schwarz, B. Holst, T. Bornath, C. Fortmann, W.-D. Kraeft, *et al.* Static ion structure factor for dense plasmas: Semi-classical and ab initio calculations. *High Energy Density Physics*, **6**(3), 305 (2010). 26

[54] G. Gregori, A. Ravasio, A. Höll, S. Glenzer, S. Rose. Derivation of the static structure factor in strongly coupled non-equilibrium plasmas for X-ray scattering studies. *High Energy Density Physics*, **3**(1), 99 (2007). 26, 29

[55] S. Y. Buhmann, D. T. Butcher, S. Scheel. Macroscopic quantum electrodynamics in nonlocal and nonreciprocal media. *New Journal of Physics*, **14**(8), 083034 (2012). 27

[56] L.-F. Chen, C. Ong, C. Neo, V. Varadan, V. K. Varadan. *Microwave electronics: measurement and materials characterization*, (John Wiley & Sons2004). 27

[57] L. P. Pitaevskii, E. M. Lifshitz. *Physical Kinetics*, (Butterworth-Heinemann1981), 1st edn. ISBN 978-0750626354. 27, 45

[58] D. Salzmann. *Atomic physics in hot plasmas.* 97, (Oxford University Press1998). 28

[59] J. Kimball. Short-Range Correlations and Electron-Gas Response Functions. *Physical Review A*, **7**(5), 1648 (1973). 29

[60] J. Kimball. High-density expansion of the electron-gas correlation function. *Physical Review B*, **14**(6), 2371 (1976). 29

[61] D. Bradley, J. Kilkenny, S. Rose, J. Hares. Time-resolved continuum-edge-shift measurements in laser-shocked solids. *Physical review letters*, **59**(26), 2995 (1987). 29

[62] D. Riley, O. Willi, S. Rose, T. Afshar-Rad. Blue shift of the K absorption edge in laser-shocked solids. *EPL (Europhysics Letters)*, **10**(2), 135 (1989). 29

[63] O. Ciricosta, S. Vinko, H.-K. Chung, B.-I. Cho, C. Brown, *et al.* Direct measurements of the ionization potential depression in a dense plasma. *Physical review letters*, **109**(6), 065002 (2012). 29

[64] F. Rogers, H. Graboske Jr, D. Harwood. Bound eigenstates of the static screened Coulomb potential. *Physical Review A*, **1**(6), 1577 (1970). 29

[65] P. Eisenberger, P. Platzman. Compton scattering of x rays from bound electrons. *Physical Review A*, **2**(2), 415 (1970). 29

[66] A. Issolah, Y. Garreau, B. Levy, G. Loupias. Experimental check of core Compton profiles, calculated using a quasi-self-consistent-field method. *Physical Review B*, **44**(20), 11029 (1991). 29

[67] B. Crowley, G. Gregori. X-ray scattering by many-particle systems. *New Journal of Physics*, **15**(1), 015014 (2013). 31

[68] G. I. Kerley. Equation of state and phase diagram of dense hydrogen. *Physics of the Earth and Planetary Interiors*, **6**(1), 78 (1972). 31, 35

[69] B. Militzer, D. Ceperley. Path integral Monte Carlo calculation of the deuterium Hugoniot. *Physical review letters*, **85**(9), 1890 (2000). 31

[70] E. E. Salpeter. Electron density fluctuations in a plasma. *Physical Review*, **120**(5), 1528 (1960). 31

[71] T. Döppner, O. Landen, H. Lee, P. Neumayer, S. Regan, *et al.* Temperature measurement through detailed balance in x-ray Thomson scattering. *High Energy Density Physics*, **5**(3), 182 (2009). 34

[72] R. Fäustlin, T. Bornath, T. Döppner, S. Düsterer, E. Förster, *et al.* Observation of ultrafast nonequilibrium collective dynamics in warm dense hydrogen. *Physical review letters*, **104**(12), 125002 (2010). 34

[73] P. Radha, T. Collins, J. Delettrez, Y. Elbaz, R. Epstein, *et al.* Multidimensional analysis of direct-drive, plastic-shell implosions on OMEGAa). *Physics of Plasmas (1994-present)*, **12**(5), 056307 (2005). 35, 81

[74] D. Keller, T. Collins, J. Delettrez, P. McKenty, P. Radha, *et al.* DRACO—A New Multidimensional Hydrocode. In *APS Division of Plasma Physics Meeting Abstracts*, vol. 1 (1999). 35

[75] G. I. Kerley. Equations of state for hydrogen and deuterium. Tech. rep., Sandia National Laboratories (2003). 35

[76] J. MacFarlane, I. Golovkin, P. Woodruff. HELIOS-CR–a 1-D radiation-magnetohydrodynamics code with inline atomic kinetics modeling. *Journal of Quantitative Spectroscopy and Radiative Transfer*, **99**(1), 381 (2006). 35, 81

[77] D. Pile. X-rays: First light from SACLA. *Nature Photonics*, **5**(8), 456 (2011). 38

[78] P. Emma, R. Akre, J. Arthur, R. Bionta, C. Bostedt, *et al.* First lasing and operation of an ångstrom-wavelength free-electron laser. *nature photonics*, **4**(9), 641 (2010). 38

[79] D. Evans, J. Katzenstein. Laser light scattering in laboratory plasmas. *Reports on Progress in Physics*, **32**(1), 207 (1969). 38, 39, 47

[80] S. H. Glenzer, R. Redmer. X-ray Thomson scattering in high energy density plasmas. *Reviews of Modern Physics*, **81**(4), 1625 (2009). 38, 40, 47

[81] G. Gregori, S. H. Glenzer, W. Rozmus, R. Lee, O. Landen. Theoretical model of x-ray scattering as a dense matter probe. *Physical Review E*, **67**(2), 026412 (2003). 38, 45

[82] S. Glenzer, G. Gregori, R. Lee, F. Rogers, S. Pollaine, *et al.* Demonstration of spectrally resolved x-ray scattering in dense plasmas. *Physical review letters*, **90**(17), 175002 (2003). 38, 70

[83] S. Glenzer, O. Landen, P. Neumayer, R. Lee, K. Widmann, *et al.* Observations of plasmons in warm dense matter. *Physical review letters*, **98**(6), 065002 (2007). 38, 70

[84] E. G. Saiz, G. Gregori, D. O. Gericke, J. Vorberger, B. Barbrel, *et al.* Probing warm dense lithium by inelastic X-ray scattering. *Nature Physics*, **4**(12), 940 (2008). 38

[85] A. L. Kritcher, P. Neumayer, J. Castor, T. Döppner, R. W. Falcone, *et al.* Ultrafast x-ray Thomson scattering of shock-compressed matter. *Science*, **322**(5898), 69 (2008). 38

[86] C. Brown, D. O. Gericke, M. Cammarata, B. Cho, T. Döppner, *et al.* Evidence for a glassy state in strongly driven carbon. *Scientific reports*, **4** (2014). 38

[87] D. Chapman, J. Vorberger, L. Fletcher, R. Baggott, L. Divol, *et al.* Observation of finite-wavelength screening in high-energy-density matter. *Nature communications*, **6** (2015). 38

[88] N. Peacock, D. Robinson, M. Forrest, P. Wilcock, V. Sannikov. Measurement of the electron temperature by Thomson scattering in tokamak T3. *Nature*, **224**(5218), 448 (1969). 38

[89] M. Forrest, P. Carolan, N. Peacock. Measurement of magnetic fields in a tokamak using laser light scattering. *Nature*, **271**, 718 (1978). 38

[90] B. Nagler, U. Zastrau, R. R. Fäustlin, S. M. Vinko, T. Whitcher, *et al.* Turning solid aluminium transparent by intense soft X-ray photoionization. *Nature Physics*, **5**(9), 693 (2009). 38

[91] P. Emma, R. Akre, J. Arthur, R. Bionta, C. Bostedt, *et al.* First lasing and operation of an ångstrom-wavelength free-electron laser. *nature photonics*, **4**(9), 641 (2010). 38

[92] O. Hurricane, D. Callahan, D. Casey, P. Celliers, C. Cerjan, *et al.* Fuel gain exceeding unity in an inertially confined fusion implosion. *Nature*, **506**(7488), 343 (2014). 38

[93] S. Regan, K. Falk, G. Gregori, P. Radha, S. Hu, *et al.* Inelastic x-ray scattering from shocked liquid deuterium. *Physical review letters*, **109**(26), 265003 (2012). 38, 45, 51

[94] G. Gregori, J. Schein, P. Schwendinger, U. Kortshagen, J. Heberlein, *et al.* Thomson scattering measurements in atmospheric plasma jets. *Physical Review E*, **59**(2), 2286 (1999). 40

[95] B. Crowley, G. Gregori. X-ray scattering by many-particle systems. *New Journal of Physics*, **15**(1), 015014 (2013). 40

[96] C. Kittel. *Introduction to solid state physics*, (Wiley2004), 8th edn. ISBN 978-0471415268. 40

[97] J. Chihara. Difference in x-ray scattering between metallic and non-metallic liquids due to conduction electrons. *Journal of Physics F: Metal Physics*, **17**(2), 295 (1987). 41

[98] L. Kadanoff, G. Baym. *Quantum Statistical Mechanics*, (W.A. Benjamin Inc.1962), 1st edn. 41

[99] N.-H. Kwong, M. Bonitz. Real-time Kadanoff-Baym approach to plasma oscillations in a correlated electron gas. *Physical review letters*, **84**(8), 1768 (2000). 41

[100] G. Gregori, S. Glenzer, O. Landen. Generalized x-ray scattering cross section from nonequilibrium plasmas. *Physical Review E*, **74**(2), 026402 (2006). 42

[101] G. Gregori, A. Ravasio, A. Höll, S. Glenzer, S. Rose. Derivation of the static structure factor in strongly coupled non-equilibrium plasmas for X-ray scattering studies. *High Energy Density Physics*, **3**(1), 99 (2007). 42

[102] V. Belyi. Fluctuation-dissipation relations for a nonlocal plasma. *Physical review letters*, **88**(25), 255001 (2002). 42, 44

[103] M. Bornatici, Y. A. Kravtsov. Comparative analysis of two formulations of geometrical optics. The effective dielectric tensor. *Plasma physics and controlled fusion*, **42**(3), 255 (2000). 42, 43, 44

[104] D. Pines, P. Nozieres. *The Theory of Quantum Liquids*, (Westview Press1999), 1st edn. 45

[105] T. Döppner, O. Landen, H. Lee, P. Neumayer, S. Regan, *et al.* Temperature measurement through detailed balance in x-ray Thomson scattering. *High Energy Density Physics*, **5**(3), 182 (2009). 47

[106] R. Fäustlin, T. Bornath, T. Döppner, S. Düsterer, E. Förster, *et al.* Observation of ultrafast nonequilibrium collective dynamics in warm dense hydrogen. *Physical review letters*, **104**(12), 125002 (2010). 47

[107] D. Chapman, D. O. Gericke. Analysis of Thomson scattering from nonequilibrium plasmas. *Physical review letters*, **107**(16), 165004 (2011). 47

[108] S. Glenzer, W. Rozmus, B. MacGowan, K. Estabrook, J. De Groot, *et al.* Thomson scattering from high-Z laser-produced plasmas. *Physical review letters*, **82**(1), 97 (1999). 50

[109] W. Rozmus, S. Glenzer, K. Estabrook, H. Baldis, B. MacGowan. Modeling of Thomson scattering spectra in high-Z, laser-produced plasmas. *The Astrophysical Journal Supplement Series*, **127**(2), 459 (2000). 50

[110] D. Chapman, D. Kraus, A. Kritcher, B. Bachmann, G. Collins, *et al.* Simulating x-ray Thomson scattering signals from high-density, millimetre-scale plasmas at the National Ignition Facility. *Physics of Plasmas*, **21**(8), 082709 (2014). 50

[111] P. Sperling, T. Liseykina, D. Bauer, R. Redmer. Time-resolved Thomson scattering on high-intensity laser-produced hot dense helium plasmas. *New Journal of Physics*, **15**(2), 025041 (2013). 50

[112] S. Y. Buhmann, D. T. Butcher, S. Scheel. Macroscopic quantum electrodynamics in nonlocal and nonreciprocal media. *New Journal of Physics*, **14**(8), 083034 (2012). 50

[113] T. Boehly, D. Brown, R. Craxton, R. Keck, J. Knauer, *et al.* Initial performance results of the OMEGA laser system. *Optics communications*, **133**(1), 495 (1997). 58

[114] H. Legall, H. Stiel, M. Schnürer, M. Pagels, B. Kanngießer, *et al.* An efficient X-ray spectrometer based on thin mosaic crystal films and its application in various fields of X-ray spectroscopy. *Journal of Applied Crystallography*, **42**(4), 572 (2009). 58, 61, 62

[115] G. Ice, C. Sparks. Mosaic crystal x-ray spectrometer to resolve inelastic background from anomalous scattering experiments. *Nuclear Instruments and Methods in Physics Research Section A: Accelerators, Spectrometers, Detectors and Associated Equipment*, **291**(1-2), 110 (1990). 58

[116] J. Kilkenny. High speed proximity focused X-ray cameras. *Laser and Particle Beams*, **9**(01), 49 (1991). 59

[117] D. Bradley, P. Bell, O. Landen, J. Kilkenny, J. Oertel. Development and characterization of a pair of 30–40 ps x-ray framing cameras. *Review of scientific instruments*, **66**(1), 716 (1995). 59

[118] J. Kilkenny, P. Bell, R. Hanks, G. Power, R. Turner, *et al.* High-speed gated x-ray imagers. *Review of Scientific Instruments*, **59**(8), 1793 (1988). 60

[119] G. L. Stradling. *Ultrahigh Speed and High Speed Photography, Photonics, and Videography*, (SPIE1990), 7th edn. 60

[120] R. Turner, O. Landen, D. Bradley, S. Alvarez, P. Bell, *et al.* Comparison of charge coupled device vs film readouts for gated micro-channel plate cameras. *Review of Scientific Instruments*, **72**(1), 706 (2001). 60

[121] M. S. del Rio, M. Gambaccini, G. Pareschi, A. Taibi, A. Tuffanelli, *et al.* Focusing properties of mosaic crystals. In *SPIE's International Symposium on Optical Science, Engineering, and Instrumentation*, 246–255, (International Society for Optics and Photonics1998). 61

[122] A. Tuffanelli, M. S. del Rio, G. Pareschi, M. Gambaccini, A. Taibi, *et al.* Comparative characterization of highly oriented pyrolytic graphite by means of diffraction topography. In *SPIE's International Symposium on Optical Science, Engineering, and Instrumentation*, 192–198, (International Society for Optics and Photonics1999). 61

[123] A. Pak, G. Gregori, J. Knight, K. Campbell, D. Price, *et al.* X-ray line measurements with high efficiency Bragg crystals. *Review of Scientific Instruments*, **75**(10), 3747 (2004). 62

[124] B. Henke, H. Yamada, T. Tanaka. Pulsed plasma source spectrometry in the 80–8000-eV x-ray region. *Review of scientific instruments*, **54**(10), 1311 (1983). 62, 70

[125] F. Marshall, T. Ohki, D. McInnis, Z. Ninkov, J. Carbone. Imaging of laser–plasma x-ray emission with charge-injection devices. *Review of Scientific Instruments*, **72**(1), 713 (2001). 63

[126] D. H. Kalantar, P. M. Bell, R. L. Costa, B. A. Hammel, O. L. Landen, *et al.* Characterization of x-ray streak cameras for use on Nova. In *22nd Int'l Congress on High-Speed Photography and Photonics*, 680–685, (International Society for Optics and Photonics1997). 64

[127] M. Urry, G. Gregori, O. Landen, A. Pak, S. Glenzer. X-ray probe development for collective scattering measurements in dense plasmas. *Journal of Quantitative Spectroscopy and Radiative Transfer*, **99**(1), 636 (2006). 65, 67

[128] D. Phillion, C. Hailey. Brightness and duration of x-ray line sources irradiated with intense 0.53-μm laser light at 60 and 120 ps pulse width. *Physical Review A*, **34**(6), 4886 (1986). 65

[129] *Omega Laser Facility Users' Guide*, (Laboratory for Laser Energetics2014). 66, 73

[130] J. Bateman. The detection of hard X-rays (10–140 keV) by channel plate electron multipliers. *Nuclear Instruments and Methods*, **144**(3), 537 (1977). 70

[131] S. Glenzer, G. Gregori, F. Rogers, D. Froula, S. Pollaine, *et al.* X-ray scattering from solid density plasmas. *Physics of Plasmas (1994-present)*, **10**(6), 2433 (2003). 70

[132] G. Gregori, S. Glenzer, F. Rogers, S. Pollaine, O. Landen, *et al.* Electronic structure measurements of dense plasmas. *Physics of Plasmas (1994-present)*, **11**(5), 2754 (2004). 70

[133] G. Gregori, S. Glenzer, H.-K. Chung, D. Froula, R. Lee, *et al.* Measurement of carbon ionization balance in high-temperature plasma mixtures by temporally resolved x-ray scattering. *Journal of Quantitative Spectroscopy and Radiative Transfer*, **99**(1), 225 (2006). 70

[134] E. G. Saiz, G. Gregori, D. O. Gericke, J. Vorberger, B. Barbrel, *et al.* Probing warm dense lithium by inelastic X-ray scattering. *Nature Physics*, **4**(12), 940 (2008). 70

[135] J. MacFarlane. VISRADA 3-D view factor code and design tool for high-energy density physics experiments. *Journal of Quantitative Spectroscopy and Radiative Transfer*, **81**(1), 287 (2003). 71, 74, 75

[136] S. P. Regan, J. A. Marozas, R. S. Craxton, J. H. Kelly, W. R. Donaldson, *et al.* Performance of 1-THz-bandwidth, two-dimensional smoothing by spectral dispersion and polarization smoothing of high-power, solid-state laser beams. *JOSA B*, **22**(5), 998 (2005). 80

[137] Gas Encyclopedia (2013). 82

[138] P. A. Jansson. *Deconvolution. With applications in spectroscopy*, vol. 1, (Academic Press1984). 85

[139] A. Thompson, D. Attwood, E. Gullikson, M. Howells, J. Kortright, *et al.* *X-ray data booklet* (2009). 87

[140] G. H. Zschornack. *Handbook of X-ray Data*, (Springer2007). 87

[141] F. Beg, I. Ross, A. Lorenz, J. Worley, A. Dangor, *et al.* Study of x-ray emission from a table top plasma focus and its application as an x-ray backlighter. *Journal of Applied Physics*, **88**(6), 3225 (2000). 87

[142] H.-J. Kunze. *Introduction to plasma spectroscopy*, vol. 56, (Springer2009). 90, 135, 136, 137, 138, 139

[143] A. Savitzky, M. J. Golay. Smoothing and differentiation of data by simplified least squares procedures. *Analytical chemistry*, **36**(8), 1627 (1964). 91

[144] M. Onoda, S. Murakami, N. Nagaosa. Hall effect of light. *Physical review letters*, **93**(8), 083901 (2004). 96

[145] P. M. Chung, L. Talbot, K. J. Touryan. *Electric Probes in Stationary and Flowing Plasmas*, (Springer1975). 102, 160, 162

[146] J. Thornton. Comparison of theory and experiment for ion collection by spherical and cylindrical probes in a collisional plasma. *AIAA Journal*, **9**(2), 342 (1971). 103, 107

[147] C. Su, R. Kiel. Continuum theory of electrostatic probes. *Journal of Applied Physics*, **37**(13), 4907 (1966). 103, 107

[148] K.-S. Chung, I. H. Hutchinson. Kinetic theory of ion collection by probing objects in flowing strongly magnetized plasmas. *Physical review A*, **38**(9), 4721 (1988). 103

[149] K.-U. Riemann. The Bohm criterion and sheath formation. *Journal of Physics D: Applied Physics*, **24**(4), 493 (1991). 107

[150] D. W. Koopman. Langmuir probe and microwave measurements of the properties of streaming plasmas generated by focused laser pulses. *Physics of Fluids*, **14**, 1707 (1971). 109, 154

[151] B. Doggett, C. Budtz-Joergensen, J. Lunney, P. Sheerin, M. Turner. Behaviour of a planar Langmuir probe in a laser ablation plasma. *Applied surface science*, **247**(1), 134 (2005). 109, 154, 166

[152] F. Nibler. *High-frequency circuit engineering*, (IET1990). 110

[153] N. Blaz, A. Maric, G. Radosavljevic, L. Zivanov, G. Stojanovic, *et al.* Modeling and characterization of frequency and temperature variation of complex permeability of ferrite LTCC material. *Progress in electromagnetics research B*, **23**, 131 (2010). 114, 115

[154] E. C. Snelling. *Soft Ferrites: properties and applications*, (Butterworth1988). 113, 115

[155] P. Rastogi, E. Hack. *Phase estimation in optical interferometry*, (CRC Press2014). 125, 128

[156] I. H. Hutchinson. *Principles of Plasma Diagnostics*, (Cambridge University Press2005). 125

[157] A. Vogel, I. Apitz, S. Freidank, R. Dijkink. Sensitive high-resolution white-light Schlieren technique with a large dynamic range for the investigation of ablation dynamics. *Optics letters*, **31**(12), 1812 (2006). 125

[158] M. Kalal, K. A. Nugent, B. Luther-Davies. Phase-amplitude imaging: its application to fully automated analysis of magnetic field measurements in laser-produced plasmas. *Applied optics*, **26**(9), 1674 (1987). 128

[159] E. McLean, S. Ramsden. Optical interferometric and spectroscopic measurements of electron density in a plasma. *Physical Review*, **140**(4A), A1122 (1965). 129, 150

[160] M. Hipp, J. Woisetschläger, P. Reiterer, T. Neger. Digital evaluation of interferograms. *Measurement*, **36**(1), 53 (2004). 130, 150

[161] G. Pretzier. A new method for numerical Abel-inversion. *Zeitschrift für Naturforschung A*, **46**(7), 639 (1991). 131, 151

[162] P. Maine, D. Strickland, P. Bado, M. Pessot, G. Mourou. Generation of ultrahigh peak power pulses by chirped pulse amplification. *IEEE Journal of Quantum electronics*, **24**(2), 398 (1988). 132

[163] U. Fantz. Basics of plasma spectroscopy. *Plasma Sources Science and Technology*, **15**(4), S137 (2006). 135, 137, 154

[164] H. Elabidi, N. B. Nessib, M. Cornille, J. Dubau, S. Sahal-Bréchot. Electron impact broadening of spectral lines in Be-like ions: quantum calculations. *Journal of Physics B: Atomic, Molecular and Optical Physics*, **41**(2), 025702 (2008). 138

[165] H. R. Griem. *Principles of plasma spectroscopy*, vol. 2, (Cambridge University Press2005). 139

[166] N. Konjević, A. Lesage, J. Fuhr, W. Wiese. Experimental Stark widths and shifts for spectral lines of neutral and ionized atoms (a critical review of selected data for the period 1989 through 2000). *Journal of Physical and Chemical Reference Data*, **31**(3), 819 (2002). 139

[167] E. Everson, P. Pribyl, C. Constantin, A. Zylstra, D. Schaeffer, *et al.* Design, construction, and calibration of a three-axis, high-frequency magnetic probe (B-dot probe) as a diagnostic for exploding plasmas. *Review of Scientific Instruments*, **80**(11), 113505 (2009). 143, 150

[168] V. N. Ochkin. *Spectroscopy of low temperature plasma*, (John Wiley & Sons2009). 154

[169] D. A. Cremers, A. K. Knight. *Laser-Induced Breakdown Spectroscopy*, (Wiley2006). 154

[170] J. MacFarlane, I. Golovkin, P. Woodruff, S. Kulkarni, I. Hall. Simulation of plasma ionization and spectral properties with PrismSPECT. In *Plasma Science (ICOPS), 2013 Abstracts IEEE International Conference on*, 1–1, (IEEE2013). 158

[171] A. Kramida, Y. Ralchenko, J. Reader. NIST atomic spectra database (ver. 5.3). *National Institute of Standards and Technology, Gaithersburg, MD* (2016). 158

[172] I. Hutchinson. Oblique ion collection in the drift approximation: How magnetized Mach probes really work. *Physics of Plasmas (1994-present)*, **15**(12), 123503 (2008). 159

[173] E. P. Szuszczewicz, P. Z. Takacs. Magnetosheath effects on cylindrical Langmuir probes. *Physics of Fluids (1958-1988)*, **22**(12), 2424 (1979). 159

[174] L. Talbot. Theory of the Stagnation-Point Langmuir Probe. *Physics of Fluids (1958-1988)*, **3**(2), 289 (1960). 160

[175] R. C. Tseng, L. Talbot. Flat Plate Boundary-Layer Studies in a Partially Ionized Gas. *AIAA Journal*, **9**(7), 1365 (1971). 160

[176] R. Wood, K. Chen, J. Leboeuf, A. Puretzky, D. Geohegan. Dynamics of plume propagation and splitting during pulsed-laser ablation. *Physical Review Letters*, **79**(8), 1571 (1997). 166

[177] A. Bulgakov, N. Bulgakova. Gas-dynamic effects of the interaction between a pulsed laser-ablation plume and the ambient gas: analogy with an underexpanded jet. *Journal of Physics D: Applied Physics*, **31**(6), 693 (1998). 166

[178] J. Allen. On supersonic plasma flow around an obstacle. *Journal of Plasma Physics*, **79**(03), 315 (2013). 166, 168